POLITECNICO DI MILANO
SCUOLA DI DOTTORATO
DOTTORATO DI RICERCA IN BIOINGEGNERIA

Deformable Image Registration for Radiotherapy Monomodal Applications

Doctoral dissertation of:
Aldo Rodrigo Mejía Rodríguez

Advisors: **M. Sc. Giovanna Rizzo**
Dr. Edgar Roman Arce Santana
Tutor: **Prof. Anna Maria Bianchi**

Supervisor of the PhD Program:

Prof. Maria Gabriella Signorini

XXV Cycle – 2013

Ph.D. Thesis in Biomedical Engineering

Publication Data:
Deformable Image Registration for Radiotherapy Monomodal Applications.
Ph.D. Thesis

Aldo Rodrigo Mejía Rodríguez
Department of Electronics, Information and Bioengineering
Politecnico di Milano
Piazza Leonardo da Vinci, 32
20133 Milano, Italy
e-mail: aldorodrigo.mejia@mail.polimi.it

POLITECNICO DI MILANO
SCUOLA DI DOTTORATO
DOTTORATO DI RICERCA IN BIOINGEGNERIA

Deformable Image Registration for Radiotherapy Monomodal Applications

Doctoral dissertation of:
Aldo Rodrigo Mejía Rodríguez

Advisors: **M. Sc. Giovanna Rizzo**
Dr. Edgar Roman Arce Santana
Tutor: **Prof. Anna Maria Bianchi**

Supervisor of the PhD Program:

Prof. Maria Gabriella Signorini

XXV Cycle – 2013

“Life is not a problem to be solved,

but a reality to be experienced.”

-Soren Kierkegaard-

To all my family,

who even in the distance made me feel their love and support.

To all those people who started as colleagues, classmates or just acquaintances,

who became friends, and now are my international family.

To Lupita,

my unconditional support,

who decided to join me in this adventure.

THANK YOU!!!

Acknowledgements

It has been a long journey, full of stressful moments, but with many more joys and achievements. Before this chapter of my life comes to its end, looking forward to begin a new one, I would like to thank

The *“Consejo Nacional de Ciencia y Tecnologia – CONACyT”* for the support for my PhD studies in Milan, Italy (reference: scholar / scholarship – 213579 / 308665).

My advisor, Dr. Giovanna Rizzo, for blindly accepted me in her research group and for letting me learn from her passion, criticism and dedication to always want to improve.

My tutors, Prof. Anna Maria Bianchi and Dr. Edgar R. Arce-Santana, for your trust and support during the PhD.

The review committee of the thesis, Dr. Ben Heijmen, Dr. Eliana Vasquez Osorio and Dr. Oscar Acosta, for their valuable contribution and dedication in reviewing this work.

My gurus in the image registration and mathematic worlds, Elisa S. and Isnardo, thank you for explain me, confuse me and amaze me about what we can do mixing some crazy ideas.

All my friends, the IBFM-LITA gang (Dani, Elisa M., Sofia, Sara, Fabio, Elena, Antonio, Prof. Lafo), the BioIng gang (Fra, Robi, Ramo, Sara, Andrea, Matteo, Jas, Sere, and the rest of this select group), the international gang (Amanda & Gustavo, Eline & Marcelo + 1, Raul, Ha) for making memorable the whole experience of living in Italy.

My family, for all your understanding and support in my decision to spend 3 long years away from them, making me always feel their presence.

My partner and confidence of adventures, Lupita, for her support and trust, showing me that we can count on each other in the good, the bad, the best and the worst situations no matter where we are.

Abstract

Modern approaches in oncology are based on the use of different imaging modalities in order to better define the morphological and biological characteristics of the tumors. Moreover, imaging can be used in radiotherapy (RT) to better control irradiation, monitoring the therapy and preserving organs at risk (OAR). This approach requires the use of registration techniques able to correctly remap the patient anatomy in the same spatial reference system, possibly taking into account organ deformations often occurring in patients undergoing a RT treatment plan.

The aim of this work is to propose and evaluate an innovative elastic registration method capable to recover complex deformations in specific thoracic RT images, like those presented in 4D CT lung images. The proposed approach consists in two steps: first, a global affine registration using the Particle Filter (PF) is performed; second, the transformation is locally refined using a discrete implementation of the Horn-Schunck Optical Flow (OF) method with four control parameters. This two-step elastic registration method is referred in the thesis as the Particle Filter + Optical Flow (PF+OF) approach.

This novel registration technique was evaluated in particular with two 4D CT medical images datasets: first, a set of 4D CT lung images from a controlled model; second, a dataset of 4D CT lung clinical images from five patients treated with RT. In addition, performance comparison between the PF+OF method and other fluid like non-parametric registration algorithms already proposed in RT for the registration in the thoracic district, Demons and Diffeomorphic Demons, was performed analyzing anatomical structures of clinical interest.

Summary

Introduction

Modern approaches in oncology are based on the use of different imaging modalities in order to better define the morphological and biological characteristics of the tumors. Moreover, imaging can be used in radiotherapy (RT) to better control irradiation, monitoring the therapy and preserving organs at risk (OAR) [Hill et al., 2001]. This approach requires the use of registration techniques able to correctly remap the patient anatomy in the same spatial reference system, possibly taking into account organ deformations often occurring in patients undergoing a RT treatment plan.

RT is a medical therapy that uses controlled high energy ionizing radiation for the treatment of tumors. The radiation damages the cellular DNA, making these cells no longer able to split and reproduce [Dobbs et al., 1998]. This fact is of particular interest because cancerous cells divide more rapidly than healthy cells, reason why cancerous cells are more sensitive to ionizing radiation, resulting in damage cancer cells and the reduction of the irradiated tumor. Healthy cells can also be damaged by irradiation, however they are able to repair much more effectively than cancer cells. Thus, the main goal of RT is to maximize the dose administered to the tumor cells and minimize the dose administered to healthy cells. The beneficial effects on the neoplasia are not immediate; typically more aggressive tumors whose cells divide more quickly, respond faster to the treatment, which results to be painless during the treatment for the patient.

Every tumor, lesion or malformation to be treated is called the target volume (TV), and for purposes of the treatment it is essential to know the location, size and shape of the target, as well as its proximity to OAR. The dose is delivered in several sessions; before each session CT images are acquired for the correct positioning of the patient and to evaluate anatomical alterations that may be presented due to physiological movements (respiration, heartbeat or displacement of body fluids), reduction of the tumor size, patient weight loss because of an alteration in the distribution of muscle mass and / or fat of the patient.

In particular, breathing motion and organ deformation may lead to geometric misses that have the potential of underdosing tumor and overdosing healthy tissue, when RT is used to treat tumors located in thorax, which could increase the risk of toxicity in the OAR [Rosu et al., 2007]. A solution to this type of problem is to plan the irradiated dose taking into account the tumor motion.

In the past few years, the development of four dimensional (4D) CT scanning technology made possible the generation of sequential image datasets for multiple phases of the breathing cycle [Vedam et al., 2003; Low et al., 2003; Pan et al., 2004]. Integration of similar concepts and tools into RT has led to 4D RT treatment planning, which could be defined [Keall et al., 2003] as the “explicit inclusion of the temporal changes of anatomy during the imaging, planning and delivery of radiotherapy.” 4D CT approaches have been examined in many studies of RT for patients with lung cancer evaluating 4D scanning, planning, and treatment delivery [Rosu et al., 2005; Keall et al., 2006; Tewatia, 2006]. RT treatment plans generated using 4D CT images to assess the dose to be dispensed on each structure must be the result of a compromise between adequate administration of ionizing radiation to the TV and the limitation of toxicity effects on OAR. In this context, local rigid or deformable registration methods are important to the RT treatment planning because they are capable to determine the geometric relationship of the structures of interest (TV and OAR) between the phases of the respiratory cycle [Nijkamp et al., 2007; Brock et al., 2006; Wolthaus et al., 2008].

In this context, the aim of this PhD project is to propose and evaluate an innovative elastic registration method, referred in this thesis as the Particle Filter + Optical Flow (PF+OF) approach, capable to recover complex deformations in specific thoracic RT images, like those presented in 4D CT lung images.

Medical Image Registration

Image registration is the process of determining the correspondence between objects in two images, by convention between the source (I_S) and target (I_T) images. To determine correspondences it is necessary to find the geometrical or spatial mapping (transformation) applied to I_S so that it aligns with I_T. From a medical point of view, image registration could be divided into two main streams: rigid and elastic or non-rigid registration methods.

Rigid transformations are those that preserve the distance between all points in the image; they are global transformations described by three parameters of translation and three parameters of rotation, and are equivalent to a change from one Cartesian system of coordinates to another one which differs by shift and rotation. Rigid registrations are often integrated with scale and shear parameters, this kind of transformations are referred to as affine transformations. The affine transformation preserves the parallelism of lines, but not their lengths or their angles. It extends the degrees of freedom of the rigid transformation with a scaling factor for each image dimension and additionally, a shearing in each dimension.

Because most of the human body cannot be seen as rigid body, non-rigid registration techniques are introduced for the correction of elastic deformations that may occur due to anatomical motions or morphological changes. In literature a great number of different elastic image registration methods are reported. One important classification could be done between points or surface based methods and intensity based methods. In the first category, corresponding points or surfaces on the two images, I_S and I_T, are used to find the existing global deformation. They have the disadvantage of needing to know corresponding points or contours in the images, which could be time consuming, costly and not always easy to obtain, but the advantage of being more locally accurate in the areas used for calculation if corresponding point are accurately chosen (i.e. the accuracy of these registration methods strictly depends on the accuracy of corresponding points placement or surfaces delineation). Methods belonging to this class are thin-plate spline [Bookstein, 2002], Wendland functions [Fornefett et al., 2001], elastic body splines [Kohlrausch et al., 2005] and finite element based methods [Brock et al., 2005]. On the other hand, intensity based methods (also called voxel property based methods) use only image intensity information to recover the spatial transformation connecting the images, consequently being more automatic and less costly but more sensitive to image noise or intensity mismatching. Most used methods belonging to this category are the optical-flow approach [Horn et al., 1981] and Thirion's Demons algorithm [Thirion, 1998], B-spline free-form deformation [Rueckert et al., 1999], calculus of variation based methods [Lu et al., 2004] and level-set methods [Vemuri et al., 2003].

For medical image registration algorithms, the major difficulty currently resides in their computational complexity. Although the speed of computers has been constantly growing, the need to decrease the computational time of methods persists. Moreover, the demand for higher robustness and accuracy of the registration usually enforce solutions utilizing the iterations or backtracking, which also produce increase of computational complexity of the method [Maintz et al., 1998; Mani et al., 2013]. In this work we proposed an algorithm with a good balance between accuracy and complexity. The proposed PF+OF approach consists in two steps: first, a global accurate affine registration using the Particle Filter (PF) is performed; second, the transformation is locally refined using a discrete implementation of the Horn-Schunck Optical Flow (OF) method with four control parameters.

The PF can be seen as a recursive implementation of Monte Carlo based statistical signal processing, in which the key idea is to obtain a posterior probability density function (*pdf)* from a set of random samples with associated weights, which allows one to estimate state variables defining a dynamic system [Arce-Santana et al., 2010]. As the number of samples becomes very large, this Monte Carlo characterization becomes an equivalent representation to the usual functional description of the posterior *pdf*, and the PF approaches the optimal Bayesian estimate. This algorithm has recently adapted to solve the rigid image registration problem in [Arce-Sanatana et al., 2009] and has increasingly been proved to be accurate, robust and, because of its parallelizable structure, it can be also considered a fast algorithm [Arce-Sanata et al., 2010; Arce-Santana et al., 2012; Mejia-Rodriguez et al., 2011; Reducindo, 2010].

On the other hand, OF methods consider that the differences between two images (target and source) could be described as motion of voxels based on the OF equation:

$$u\nabla a(x) = b(x) - a(x)\,, \tag{1}$$

where *a(x)* and *b(x)* refer to the intensity value of a voxel *x* in the target and source images respectively, and *u* is the velocity component of the optical flow. Sequences of ordered images allow the estimation of motion as either instantaneous image velocities or discrete image displacements. In general, OF methods try to calculate the motion between two image frames, taken at times t and Δt, at every voxel position. Equation (1) has two unknowns and cannot be solved as such; this is known as the aperture problem of OF algorithms and to deal with it and find the OF u another set of equations is needed, given by some additional constraint. One technique to solve the OF is used in [Arce-Santana et al., 2010] which is based on a discrete reformulation of the Horn-Schunck method [Horn et al., 1981], where it is minimized the next energy function:

$$\Psi(d) = \sum_{\forall r} \left[I_T(r) - I_S(r + d(r)) \right]^2 + \lambda \sum_{<r,s>} \| d(r) - d(s) \|_2^2 \,, \tag{2}$$

where d is the displacement field, r is the coordinates vector of the pixel or voxel, $<r,s>$ represents the nearest neighbors of r, λ is a regularization constant to control the flow homogeneity, and ||.|| represents the Euclidean norm. In this case the regularization term is expressed in probabilistic terms in the form of a prior Markov Random Field [Marroquin, 2000].

Particle Filter +Optical Flow Registration Approach.

Given a source and a target images, I_S and I_T, the basic idea of the parametric registration based on PF is to estimate the parameters vector Par of a geometrical transformation (e.g. affine) by an stochastic search over an optimization surface (cost function). This goal is achieved by using a set of N_S test points called particles $(Par_1, \cdots, Par_{N_S})$, and their associated weights $(W_1, \cdots, W_{N_S})$ calculated by a *likelihood* function $p(z|Par_j)$ for a measurement z between the images:

$$W_j = \frac{1}{\sqrt{2\pi}\sigma_\eta} \exp\left\{ \frac{-\left(2-\mathrm{NMI}\left\{I_T(\mathbf{r}), I_S\left(T(\mathbf{r}|Par_j)\right)\right\}\right)}{2\sigma_\eta^2} \right\}, \qquad j = 1, \cdots, N_S; \tag{3}$$

where $\mathbf{r}$ is the coordinates vector *(x,y,z)* of a voxel, $T(\mathbf{r}|Par)$ is a geometrical transformation depending on the parameters vector Par, σ_η^2 is the noise variance in the measurement z, and $\mathrm{NMI}(\cdot,\cdot)$ represents the normalized mutual information between two images.

Weights W_j are used to approximate *a posteriori pdf* $p\left(Par_j|z\right)$ of the unknown parameters vector Par given a measurement z. In this way, for a window of k observations $(z^1, \cdots, z^k)$, the estimated vector $\widehat{Par}^k$ of the parametric transformation can be computed by the expected value of the approximated *pdf* as follows:

$$\widehat{Par}^k = E[Par|z^1, \cdots, z^k] \approx \sum_{j=1}^{N} W_j^k Par_j^k, \tag{4}$$

Once carried out the initial parametric registration using the PF, the remaining displacements $d(\mathbf{r})$ are obtained by an OF technique, in particular by minimizing the following non-linear quadratic energy function:

$$\Psi_{opt}(d) = \sum_{\forall r} \left[I_T(r) - I_S(r + d(r))\right]^2 + \lambda^T \sum_{<r,s>} (d(r) - d(s))^2 + \beta \sum_{\forall r} \| d(r) \|^2 , \tag{5}$$

where $\langle \mathbf{r}, \mathbf{s} \rangle$ represents the nearest neighbors of $\mathbf{r}$, λ^T is the vector containing the regularization terms λ_x, λ_y and λ_z to control the flow homogeneity in every direction of the image, ||.|| represents the Euclidean norm, and β is a regularization term to control the optical flow field velocity. The non-linear quadratic cost function in eq, (5) can be linearized by conducting a first order Taylor approximation on the data term $\sum_{\forall r}[I_T(r) - I_S(r + (d(r))]^2$ and the solution for the quadratic problem can be obtained deriving with respect to $d(\mathbf{r})$, and then solving the resulting system of linear equations by the iterative Gauss-Seidel technique. Thus, the PF+OF elastic registration algorithm can be achieved in the next three steps:

1. Parametric Registration (Rigid). Find the parameters vector $\widehat{Par}$ of the perspective transformation $T(\mathbf{r}|\widehat{Par})$ that provide the best alignment between $I_T(\mathbf{r})$ and $I_S(\mathbf{r})$, and compute the initial (rigid) displacement vector field $d_0(\mathbf{r})$.
2. Optical Flow. Find the displacements between I_T and $\tilde{I}_S$ by an OF iterative scheme, $d(\mathbf{r}) = d_1(\mathbf{r}) + d_2(\mathbf{r}) + \cdots + d_k(\mathbf{r})$, until convergence is achieved; where at each k-th iteration the OF is computed over $I_T(\mathbf{r})$ and $\tilde{I}_S^k(\mathbf{r})$, where $\tilde{I}_S^k(\mathbf{r}) \triangleq \tilde{I}_S\left(\mathbf{r} + \sum_{\boldsymbol{i=1}}^{\boldsymbol{k-1}} d_i(\mathbf{r})\right)$.
3. Elastic Registration. Finally, we can obtain the vector field of the non-rigid deformation by adding the rigid vector field to the one obtained by the iterative OF, i.e., $V(\mathbf{r}) \triangleq d_0(\mathbf{r}) + d(\mathbf{r})$. Consequently, we can deduce the elastic registered image as $I_R(\mathbf{r}) \triangleq I_S(\mathbf{r} + V(\mathbf{r}))$.

Experimental Protocol

The PF+OF registration technique was evaluated in particular with two 4D CT medical images datasets. As a first step, registration algorithms were evaluated using the POint-validated PIxel-based (POPI) breathing thorax model provided by [Vandemeulebroucke et al., 2007]; the POPI model consists of a dataset of 4D CT thorax images binned into 10 respiratory phases (00%, 10%, 20%, ..., 90%) acquired from a real patient; CT images from phase 10 (onset of inspiration) were always used as I_T, the nine remaining phases were used as I_S, thus leading to a total of nine registrations. Then, a clinical images dataset formed by 4D CT images from studies of 5 patients treated for locally advanced non-small cell lung cancer (NSCLC) with Helical Tomotherapy (HT) was use to complement the evaluation of the proposed registration algorithm. For each patient, images from the inspiratory and expiratory phases were registered, using the first one as the target image.

In addition, a performance comparison between the PF+OF method and other fluid-like non-parametric registration algorithms already proposed in RT for the registration in the thoracic district due to their high performance and accuracy, Demons and

Diffeomorphic Demons [Peyrat et al., 2008; Janssens, 2009; Castillo, 2009; Zhong, 2010], was performed analyzing anatomical structures of clinical interest.

Differences in structures between correspondence respiratory phases before and after the registration process were calculated using standard indices usually adopted for registration accuracy assessment [Wang et al., 2008; Heimann et al., 2009; Faggiano et al., 2011-a; Ecabert et al., 2011]: the Dice similarity coefficient (DICE), that measures the overlap between two structures; the Average Symmetric Distance (ASD), that gives an idea about the mean mismatch; the Maximum distance between structures (DMax), a quantitative value of the worst mismatch; and the Percentage of Distance Bigger than the Voxel Dimension (%DBVD), a metric of all misalignments bigger than the voxel thickness between structures. For the POPI model, the Target Registration Error (TRE) was also computed as the error distance between coordinates of available landmarks in the target and source images.

Results

An example of the results found with the PF+OF approach with both datasets is presented in figure 1, where it is possible to observe a proper recovery of the misalignments due to the respiratory motion presented in the 4D CT lung images.

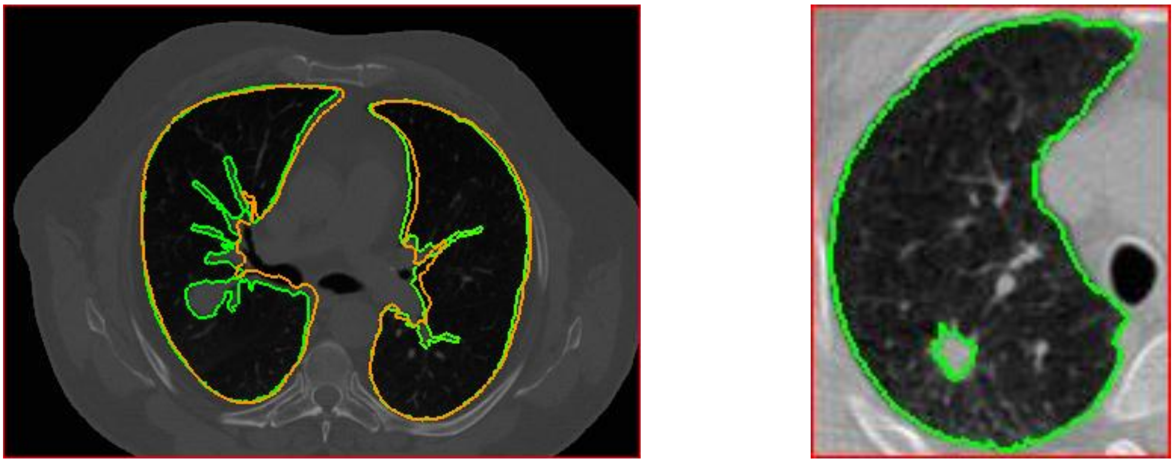

(a) (b)

Figure1. Examples of the registration results achieved by the PF+OF proposed approach using the POPI model (a), and the clinical images dataset (b). In both cases the green contours represent the structures of interest (lungs and GTV) after the registration process.

In this image is possible to observe the good performance achieved by the proposed method, being able to recover complex misalignments, in particular in the tumor zone, due to the respiratory motion.

Quantitative analysis performed by the registration accuracy indices, shows a good improvement achieved by PF+OF with respect to the indices values found before the registration process (Pre). Considering the POPI model the results found (PF+OF vs. Pre) were : ASD - 0.87±0.12 vs. 2.01±0.64 mm; DICE - 0.96±0.01 vs. 0.94±0.01; DMax - 33.12±2.95 vs. 35.59±2.59 mm; %DBVD - 8.77±9.80 vs. 40.33±11.05 %; and TRE - 1.65±0.68 vs. 3.13±1.95 mm. Considering the clinical images dataset results were: ASD lungs - 1.74±0.43 vs. 4.02±2.17 mm, ASD GTV - 1.43±0.10 vs. 3.08±1.57 mm; DMax lungs - 63.21±18.90 vs. 77.89±43.93 mm, DMax GTV - 12.06±4.64 vs. 14.36±6.75 mm; DICE lungs - 0.94±0.02 vs. 0.87±0.09, DICE GTV - 0.72±0.06 vs. 0.52±0.09; %DBVD lungs - 27.16±11.79 vs. 46.65±29.03 %, %DBVD GTV - 33.74±19.58 vs. 62.19±25.91. These results are comparable to the ones found with Demons and Diffeomorphic Demons algorithms. As a matter of fact, no significant differences were found between PF+OF and the Demons based algorithms.

Conclusion

In this work, a novel non rigid registration approach was presented, based on a global accurate affine registration using the Particle Filter followed by an elastic local transformation using a discrete implementation of the Horn-Schunck Optical Flow with four control parameters that gives to the user the possibility to better control the flow field.

The results have shown that our elastic registration method is capable to recover complex deformations presented in the thoracic district caused by the respiratory motion and is comparable to the state of the art algorithms, suggesting that the PF+OF approach could be useful in a clinical RT context, for applications such as assessing the dose to be dispensed on the gross target volume (GTV) and organs at risk (OAR) of RT treatment plans generated by the use of 4D CT images.

Publications

Papers on international peer-reviewed journals

- Claudio Fiorino, Giovanna Rizzo, Elisa Scalco, Sara Broggi, Maria Luisa Belli, Italo Dell'Oca, Nicola Dinapoli, Francesco Ricchetti, **Aldo Mejia Rodriguez**, Nadia Di Muzio, Riccardo Calandrino, Giuseppe Sanguineti, Vincenzo Valentini, Giovanni Mauro Cattaneo. "Density variation of parotid glands during IMRT for head–neck cancer: Correlation with treatment and anatomical parameters", Radiotherapy and Oncology, 2012.
- Isnardo Reducindo, **Aldo R. Mejia-Rodriguez**, Edgar R. Arce-Santana, Daniel U. Campos-Delgado, Flavio Vigueras-Gomez, Elisa Scalco, Anna M. Bianchi, Giovanni M. Cattaneo, Giovanna Rizzo. "Multimodal Non-Rigid Registration Methods Based on Local Variability Measures in CT and MR Brain Images", IET Image Processing, March 2013 (Submitted).

Conference proceedings

- **A. R. Mejia-Rodriguez**, E. Arce-Santana, E. Scalco, D. Tresoldi, M. Mendez, A. Bianchi, G. Cattaneo, and G. Rizzo. "Elastic registration based on particle filter in radiotherapy images with brain deformations", in Engineering in Medicine and Biology Society, EMBC, 2011 Annual International Conference of the IEEE, pp. 8049-8052.
- **Mejia-Rodriguez A.R.**, Scalco E., Tresoldi D., Belli M.L., Bianchi A.M., Fiorino C. and Rizzo G. "Analysis of 3D anatomical structures in radiotherapy: a mesh-based

approach", 3rd Italian Bioengineering National Group Congress, Rome, Italy, June 2012. Poster Session.

- **Aldo R. Mejia-Rodriguez**, Elisa Scalco, Daniele Tresoldi, Anna M. Bianchi, Edgar R. Arce-Santana, Martin O. Mendez, Giovanna Rizzo. "A Mesh-Based Approach for the 3D Analysis of Anatomical Structures of Interest in Radiotherapy", in Engineering in Medicine and Biology Society, EMBC, 2012 Annual International Conference of the IEEE, San Diego, California August 27 – September 3 2012.
- Isnardo Reducindo, Edgar R. Arce-Santana, Daniel U. Campos-Delgado, Flavio Vigueras-Gomez, **Aldo R. Mejia-Rodriguez**, Giovanni M. Cattaneo, Giovanna Rizzo. "Registro Elástico de Imágenes Médicas Multimodales Basado en Estadísticos Condicionales de la Distribución Conjunta de Intensidades", Encuentro en Telecomunicaciones y Análisis de Señales (ETAS) 2012. San Luis Potosí, México, Noviembre 2012.
- Isnardo Reducindo, Edgar R. Arce-Santana, Daniel U. Campos-Delgado, Flavio Vigueras-Gomez, **Aldo R. Mejia-Rodriguez**, Giovanni M. Cattaneo, Giovanna Rizzo. "Non-rigid Multimodal Medical Image Registration Based on the Conditional Statistics of the Joint Intensity Distribution" Procedia Technology, Volume 7, 2013, Pages 126-133.
- I. Reducindo, **A.R. Mejia-Rodriguez**, E.R. Arce-Santana, D.U. Campos-Delgado, G. Rizzo. " Non-rigid Multimodal MRI Registration by Local Uncertainty Quantification and Fluid Models", IX International Seminar on Medical Information Processing and Analysis (SIPAIM), Mexico City, November 2013 (accepted).

Contents

Chapter 1

Introduction

Modern approaches in oncology are based on the use of different imaging modalities in order to better define the morphological and biological characteristics of tumors. Moreover, imaging can be used in radiotherapy (RT) to better control irradiation, monitoring the therapy and preserving organs at risk (OAR) [Hill et al., 2001]. This approach requires the use of registration techniques able to correctly remap the patient anatomy in the same spatial reference system, taking into account organ deformations due to breathing, reduction of the tumor treated with radiation, or side effects (weight loss or increase / reduction of OAR surrounding the tumor) often occurring in patients undergoing a RT treatment [Faggiano et al., 2011-b]. In particular, when RT is used for the treatment of Non-Small-Cell Lung Cancer (NSCLC), lung parenchyma can significantly modify its volume and shape [Fox, 2009]; as a direct consequence, dose discrepancies can occur between the planned cumulative dose distribution and the actual cumulative dose [Mageras et al., 2007]. This is a major issue in lung cancer as lung parenchyma is one of the most radiosensitive healthy tissues in the thorax; in addition a proper correction of respiratory motion is needed in order to achieve an accurate cumulative dose distribution [Orban et al., 2007]. In this context, accurate image registration algorithms capable to correct motion of both lung and tumor along the respiratory cycle are needed.

Medical image registration methods have been studied for many years [Hill, 2001], and, for practical purposes, they can be divided into two main streams: rigid registration

(RR), and elastic or non-rigid registration (NRR) [Zitova et al., 2003; Modersitzki, 2004]. In RR methods a global transformation is applied to every voxel in the image to be registered; they have been studied extensively, where techniques based on gradient descent [Nocedal et al., 2006; Pluim et al., 2000] are most commonly used to optimize a similarity metric (e.g. Mutual Information [Wells et al., 1996; Pluim et al., 2003]) and to obtain the spatial transformation that aligns the target and source images. Other options based on global optimization methods such as genetic algorithms [Man et al., 2001] and particle filtering [Arulampalam et al., 2002], have begun to play an important role in this field [Das et al., 2010; Arce-Santana et al., 2012]. On the other hand, NRR methods estimate a transformation for each voxel, incorporating restrictive assumptions (e.g. smoothness in the deformation field) in order to make the problem well-posed. In the literature, one of the most common methods to solve the elastic registration process is based on splines, where a family of functions is used to approximate the complex deformations, but despite their good performance a main drawback of these methods is their complexity and high computational cost [Xuan et al., 2006; Klein et al., 2009; Faggiano et al., 2011-a]. Another common approach to solve the NRR problem is based on the optical flow (OF) concept, where algorithms work under the assumption of intensity conservation between images, making possible to describe deformations as motion of voxels in the images to be registered [Horn et al., 1981; Guerrero et al., 2004; Zhang et al., 2008].

The aim of this work is to propose and evaluate an innovative elastic registration method capable to recover complex deformations in the thoracic district, like those presented in RT 4D CT lung images. Our approach consists in two steps: first, a global accurate affine registration using a Particle Filter (PF) methodology is performed; second, the transformation is locally refined using a discrete iterative Optical Flow (OF) implementation. In PF an iterative stochastic search of the rigid transformation parameters is carried out using a Monte Carlo model. This iterative process has proved to be accurate and capable to recover complex rigid deformations and, because of the algorithm structure is highly parallelizable, is also considered a fast solution to the RR problem [Arce-Santana et al., 2009; Arce-Santana et al., 2012]. For the NRR step, our proposed OF is a discrete implementation of the Horn-Schunck OF with four control parameters instead of one used in the original method [Horn et al., 1981], making possible to control the flow in each dimension of the image (x,y,z), and the velocity of the flow field.

This novel registration technique, PF followed by an OF process (PF+OF), is specifically configured for its use with 4D CT images of the thoracic district in patients with NSCLC undergoing RT treatment. To evaluate registration accuracy, differences in anatomical structures of interest (tumor and OAR), before and after registration, were calculated by using standard indices adopted for accuracy assessment. In addition, PF+OF results were compared with some of the state of the art algorithms used in medical imaging, such as Demons [Thirion, 1998] and Diffeomorphic Demons [Vercauteren et al., 2008].

This project was developed at the Institute of Bioimaging and Molecular Physiology from the National Research Council (IBFM-CNR) in Milan (Italy), in collaboration with the Medical Physics Department of San Raffaele Hospital in Milan (Italy) and the Faculty of Sciences from the Autonomous University of San Luis Potosi (Mexico).

In Chapter 2 a brief description of the clinical scope and the related image registration techniques proposed in literature for their use in RT are shown. In Chapter 3, theoretical basis of PF and OF to solve the image registration problem and a detail description of the proposed PF+OF implementation are presented. The experimental protocol to validate and compare the PF+OF approach with the Demons and Diffeomorphic Demons algorithms using 4D CT lung images is presented in Chapter 4. Results are shown in Chapter 5 and, finally, in Chapter 6 discussion and conclusions of the PhD work are presented; further research possibilities are also discussed in the last chapter of this work.

In addition, three appendices are also presented in this thesis, which describes the preliminary results of future research paths, in which the proposed PF+OF algorithm is involved. Appendix A presents the validation and accuracy evaluation of the proposed method using 2D CT and MR brain images with simulated and real deformations of brain structures. In Appendix B, initial results of the proposed registration method to overcome the intensity conservation constrain of OF and solve multimodal image registration cases by applying an intensity mapping based on local variability measures (LVM) are shown. Finally, Appendix C details an alternative to assess the registration accuracy fully in 3D, analyzing structures of interest under a mesh-based approach.

Chapter 2

Image Registration Methods for Radiotherapy Applications

Medical images are used for diagnosis, treatment planning, disease monitoring and image guided surgery; they are acquired using a variety of imaging modalities like Computed Tomography (CT), X-ray, Magnetic Resonance Imaging (MRI), Positron Emission Tomography (PET), Ultrasound (US), among others. Images obtained using different modalities need to be compared and/or combined for analysis and decision making. To monitor disease progress and growth of abnormal structures, images are acquired from subjects at different times or with different imaging modalities; therefore misalignment between images is inevitable and this reduces the accuracy of further analysis. Image Registration plays an important role in medical image analysis, because is a task capable to reliably estimate the geometric transformation such that two images can be precisely aligned; its application in radiotherapy (RT) is particularly useful.

In this chapter, a brief description of the clinical goal of RT, is presented. In addition, description of medical image registration methods, alongside with the usual validation strategies used in clinical applications, are presented.

2.1 Radiotherapy treatment - Basic concepts

RT is a medical therapy that uses controlled high energy ionizing radiation for the treatment of tumors. The radiation damages the cellular DNA, making these cells no longer able to split and reproduce [Dobbs et al., 1998]. This fact is of particular interest because cancerous cells divide more rapidly than healthy cells, reason why cancerous cells are more sensitive to ionizing radiation, therefore resulting in damage cancer cells and the reduction of the irradiated tumor. Healthy cells can also be damaged by irradiation, however they are able to repair much more effectively than the cancer cells. The main goal of RT is to maximize the dose administered to the tumor cells and minimize the dose administered to healthy cells. The beneficial effects on the neoplasia are not immediate; typically more aggressive tumors whose cells divide more quickly, respond faster to the treatment, which results to be painless during the treatment for the patient.

Radiation can be administered with two different approaches:

1. By administration of radiation through an external beam generated by a device that conveys high energy radiation (X-rays, gamma rays or photons) to the tumor.
2. By an internal irradiation conveyed from the inside of the body by placing the radioactive material directly inside the tumor (brachytherapy).

An example of a complete typical process followed by a RT treatment is presented in figure 2.1. According to the International Commission on Radiation Units and Measurements (ICRU), every tumor, lesion or malformation to be treated is called the target volume (TV), and for purposes of the treatment it is essential to know the location, size and shape of the TV as well as its proximity to organs at risk (OAR). In addition, several volumes related to both tumor and normal tissues have been defined for use in the treatment-planning and reporting processes of RT. Delineation of these volumes is an obligatory step in the planning process, as absorbed dose cannot be prescribed, recorded, and reported without specification of target volumes and volumes of normal tissue at risk. The volumes to be defined are [Journal of the ICRU, Vol 10 No 1 (2010), Report 83, Oxford University Press]:

- GTV (gross tumor volume), the volume containing the gross demonstrable extent of the tumor.
- CTV (clinical target volume), the volume that has to be radiated, allowing margins around GTV for subclinical disease including any other tissues with presumed tumor. The CTV must receive adequate dose to achieve the therapeutic aim.
- ITV (internal target volume), this volume allows margins on the CTV for positional and shape changes during therapy.
- PTV (planning target volume) takes into account the asymmetric nature of positional uncertainties and patient movements combined subjectively so that the prescribed dose is received by the CTV.

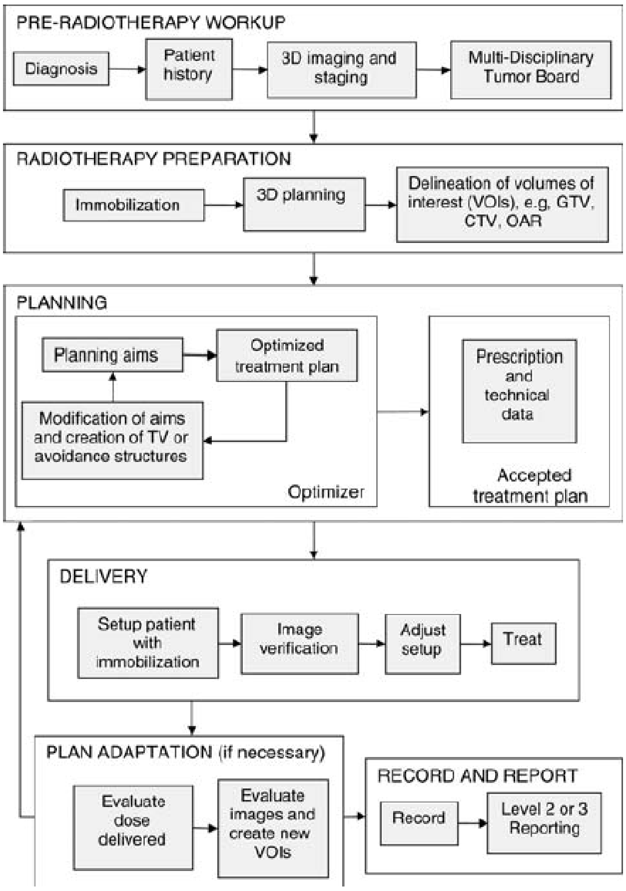

Figure 2.1. Flowchart of a typical course of radiotherapy (image taken from [Journal of the ICRU, Vol 10 No 1 (2010), Report 83, Oxford University Press]).

Taking into account these definitions, it is possible to state that GTV, CTV, and OAR correspond, respectively, to volumes of known (GTV), and/or suspected tumor infiltration (CTV), and volumes of normal tissues that might be irradiated and affect the treatment prescription (OAR). These volumes have an anatomical/physiological basis, in contrast to the ITV and the PTV, which are concepts introduced to ensure that the absorbed dose delivered to the corresponding CTV and OAR match the prescription constraints. A visual representation of the defined volumes used in a RT context is shown in figure 2.2.

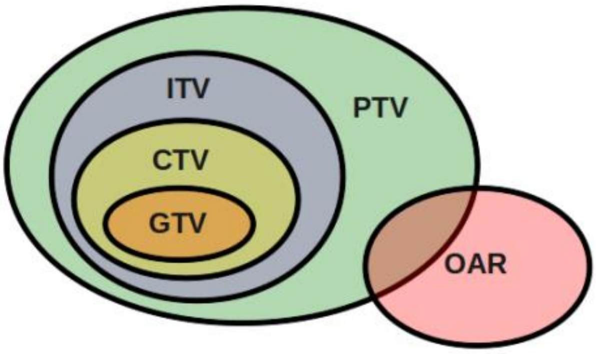

Figure 2.2. ICRU volumes definition: GTV (gross tumor volume), CTV (clinical target volume), ITV (internal target volume), PTV (planning target volume), organs at risks (OAR).

The dose is delivered in several sessions; before each session CT images are acquired for the correct positioning of the patient and to evaluate anatomical alterations that may be presented due to physiological movements (respiration, heartbeat or displacement of body fluids), reduction of the size of the tumor, weight loss of the patient because of an alteration in the distribution of muscle mass and / or fat of the patient.

It has been proved in [Brock, 2007] that the update of the treatment plan may be useful in the dose administration error resulting from the anatomical changes (physiological and pathological) of the patient, which can deliver a dose to the GTV and the OAR structures different from the functional dose planned to treat a particular disease. In this context, image registration methods are useful for the RT treatment planning because they have the potential to estimate and recover deformations presented in the images acquired at different times during the treatment.

On the other hand, breathing motion and organ deformations may lead to geometric misses that have the potential of underdosing tumor and overdosing healthy tissue, when RT is used to treat tumors located in thorax, which could increase the risk of toxicity in the OAR

[Rosu et al., 2007]. A solution to this type of problem is to plan the irradiated dose taking into account the tumor motion.

Historically, the three-dimensional (3D) anatomical description of the patient used for RT treatment planning was acquired during free breathing CT scanning, and thus was affected by motion artifacts [Balter et al., 1996; Wong et al., 1999; Shimizu et al., 2000]. This has made TV definition prone to errors and inaccuracies, as well as the estimation of the dose to be received by the patient. Voluntary breath hold or active breathing control techniques [Wong et al., 1999; Dawson et al., 2001], and deep inspiration breath hold [Hanley et al., 1999; Rosenzwaig et al., 2000; Mah et al., 2000], improved the quality of the CT images, but usually limited the geometrical information to just one phase of the breathing cycle. As a result, the subsequent delivery of the radiation only during a selected phase or portion of the breathing cycle significantly reduced the duty cycle. In the past few years, the development of the four dimensional (4D) CT scanning technology made possible the generation of sequential image datasets for multiple phases of the breathing cycle [Vedam et al., 2003; Low et al., 2003; Pan et al., 2004]. Integration of similar concepts and tools into RT has led to 4D RT treatment planning, which could be defined [Keall et al., 2003] as the “explicit inclusion of the temporal changes of anatomy during the imaging, planning and delivery of radiotherapy.” 4D CT approaches has been examined in many studies of RT for patients with lung cancer evaluating 4D scanning, planning, and treatment delivery [Rosu et al., 2005; Keall et al., 2006; Tewatia, 2006]. RT treatment plans generated using 4D CT images to assess the dose to be dispensed on each structure must be the result of a compromise between adequate administration of ionizing radiation to the TV and the limitation of toxicity effects on OAR. In this context, local rigid or deformable registration methods are important to the RT treatment planning because they are capable to determine the geometric relationship of the structures of interest (TV and OAR) between the phases of the respiratory cycle [Nijkamp et al., 2007; Brock et al., 2006; Wolthaus et al., 2008].

2.2 Medical Image Registration Methods

Image registration is the process of determining the correspondence between objects in two images, by convention between the source (I_S) and the target (I_T) image. To determine correspondences it is necessary to find the geometrical or spatial mapping (transformation) applied to I_S so that it aligns with I_T. From a medical point of view, image registration could be divided into two main streams: rigid and elastic or non-rigid registration methods.

Rigid transformations are those that preserve the distance between all points in the image; they are global transformations described by three parameters of translation and three parameters of rotation, and are equivalent to a change from one Cartesian system of coordinates to another one which differs by shift and rotation. The first works related to the registration of medical images attempted to realign brain images from the same patient acquired with different image modalities (MRI and CT or PET) or the bones when neither skull nor dura has been opened [Crumet al., 2004]. It is popular because in many common medical images the rigid body constraint leads to a good approximation and it has relatively few parameters to be determined. Rigid registrations are often integrated with scale and shear parameters, this kind of transformations are referred to as affine transformations. The affine transformation preserves the parallelism of lines, but not their lengths or their angles. It extends the degrees of freedom of the rigid transformation with a scaling factor for each image dimension and additionally, a shearing in each dimension. In medical imaging this type of transformations are capable to partially compensate problems due to differences in the calibration between scanners or large scale differences between subjects.

Because most of the human body cannot be seen as rigid body, non-rigid registration techniques are introduced for the correction of the elastic deformation that may occur due to anatomical motions or morphological changes. In literature a great number of different elastic image registration methods are reported. One important classification could be done between points or surface based methods and intensity based methods.

In the first category, corresponding point or surfaces on the two images I_S and I_T are used to find the existing global deformation. They have the disadvantage of needing to know corresponding point or contours in the images which could be time consuming, costly and not always easy to obtain, but the advantage of being more locally accurate in the areas used for calculation if corresponding point are accurately chosen (i.e. the accuracy of these registration methods strictly depends on the accuracy of corresponding points or surfaces delineation). Methods belonging to this class are thin-plate spline [Bookstein, 2002], Wendland functions [Fornefett et al., 2001], elastic body splines [Kohlrausch et al., 2005] and finite element based methods [Brock et al., 2005]. On the other hand, intensity based methods (also called voxel property based methods) use only image intensity information to recover the spatial transformation connecting the images consequently being more automatic and less costly but more sensitive to image noise or intensity mismatching. Most used methods belonging to this category are optical-flow [Horn et al., 1981] and Thirion's

Demons algorithm [Thirion, 1998], B-spline free-form registration [Rueckert et al., 1999], calculus of variation based methods [Lu et al., 2004] and level-set methods [Vemuri et al., 2003]. In the next paragraphs, some of the registration methods mentioned above used in a RT context will be briefly described.

Thin-plate spline registration method

The thin-plate spline (TPS) method [Bookstein, 2002; Chui et al., 2003], estimates the deformation through the minimization of the distance between corresponding points in the images to be registered. To determine the transformation function the following energy function have to be minimized:

$$E(f) = \min \sum_{j=1}^{k} \| p_j - f(q_j) \|^2 + \lambda T \| Lf \|^2 , \qquad (2.1).$$

where $\sum ||p_j - f(q_j)||^2$ is the distance to be minimized between the reference points p_j and the deforming points q_j, f is a TPS of the form $f(x) = \phi(x) \cdot c + x \cdot d$ (where c is a matrix of non rigid coefficients, d is an affine matrix and $\phi(x)$ is vector related to the TPS kernel), λT is a deformation weight term that controls the degree of deformation of the transformation function, and $||Lf||^2$ is a smoothness measure of f. For more details in the implementation the reader is refer to [Chui et al., 2003; Vasquez Osorio et al., 2009]. Each control point belonging to a thin-plate spline has a global influence on the transformation in that, if its position is perturbed, all other points in the transformed image change. This can be a disadvantage because it limits the ability to model complex and localized deformations and because, as the number of control points increases, the computational cost associated with moving a single point rises steeply. An example of the use of this approach in RT is presented in [Vasquez Osorio et al., 2008] where a thin-plate elastic registration algorithm was applied to head-and-neck cancer (HNC) patients with a planning contrast-enhanced CT and one contrast-enhanced CT acquired two weeks after, with the purpose to performed a local regional evaluation of anatomical changes of parotid and submandibular glands using deformation calculated by image registration.

B-spline free-form registration method

B-splines Free-Form Deformation (FFD) proposes to deform an image by manipulating a regular grid of points distributed over the image with a variable spacing to ensure maximum flexibility in the control of the precision of the deformation of the grid. The estimation of the local strain on the nodes of the grid and the deformation on the voxels of the image, which do not match with the control points, require a B-Spline interpolation [Rueckert et al., 1999]. B-spline functions are define as polynomial basis function of n>0 degree, and could be define also as the convolution of splines of order n-1 with the spline of zero degree B^0. In particular, FFD methods used the familiar 1-D cubic B-splines:

$$\beta^{(3)}(x) = \begin{cases} \frac{1}{6}\left(4 - 6x^2 + 3|x|^3\right), & 0 \le |x| < 1 \\ \frac{1}{6}\left(2 - |x|\right)^3, & 1 \le |x| < 2 \\ 0, & 2 \le |x| \end{cases} , \tag{2.2}$$

B-spline based non-rigid registration techniques are popular due to their general applicability, transparency and computational efficiency. Their main disadvantage is that special measures are sometimes required to prevent folding of the deformation field and these measures become more difficult to enforce at finer resolutions. Orban et al. [Orban et al., 2007] computed dense displacement fields using a combination of rigid and a b-splines FFD registration between Respiratory Correlated - CT (RC-CT) images in order to improve the treatment planning in RT for NSCLC by adding information in tumor delineation and dose planning. In [Faggiano et al., 2011-a], they proposed and validated a registration method based on FFD and mutual information to elastically register planning kilo voltage CT (kVCT) images with daily mega voltage CT (MVCT) images in order to estimate lung parenchyma modification of NSCLC patients during Tomotherapy treatment

Optical-flow methods

Fluid registration, also known as optical flow (OF), methods consider that the differences between target and source images could be described as motion of voxels based on the OF equation:

$$u\nabla a(x) = b(x) - a(x), \tag{2.3}$$

where *a(x)* and *b(x)* refer to the intensity value of a voxel x in the target and source images respectively and *u* is the velocity component of the flow. Given a sequence of two images, OF methods find voxels correspondence by computing a displacement field describing the apparent motion represented by matching the intensity gradients in the two images. In order to solve the OF equation, another set of equations is needed, given by some additional constraint, for example a term of smoothness in the flow field. All optical flow methods introduce additional conditions for estimating the actual flow. In literature the principal methods to solve the OF process are the Horn-Schunck [Horn et al., 1981] and Lucas-Kanade [Lucas et al., 1981] methods; current OF methods are mainly variations of these methods [Bruhn et al., 2003; Zhang et al., 2008]. The main drawback of OF methods is that usually their additional constrains limit the velocity of the flow making it difficult to recover large deformations. In addition, OF methods are constrained by the assumption of intensity conservation between images, thus, methods are limited to monomodal cases. Castillo et al. [Castillo et al., 2009] evaluated an Optical Flow (OF) registration method and a landmark-based moving least-squares algorithm using a large number of landmarks (>1100) for the registration of 4D CT thoracic treatment planning data. Their results demonstrate that large landmark point sets provide an effective means for objective evaluation of deformable image registration algorithms with a narrow uncertainty range, based on the high performance found in both studied methods, suggesting that this strategy could be used for quality assurance of registration methods on a routine clinical basis.

Thirion's Demons algorithm

In [Thirion, 1998], the author proposed to consider non-parametric non-rigid registration as a diffusion process. He introduced demons that push according to local characteristics of the images in a similar way Maxwell did for solving the Gibbs paradox (thermodynamic). The forces are inspired from the OF equations, thus the algorithm can be considered as a variant of a fluid NRR method. However the main difference is that instead of having a flow field in the entire image, in the Demons algorithm the forces are applied in the borders of the objects inside the images (figure 2.1).

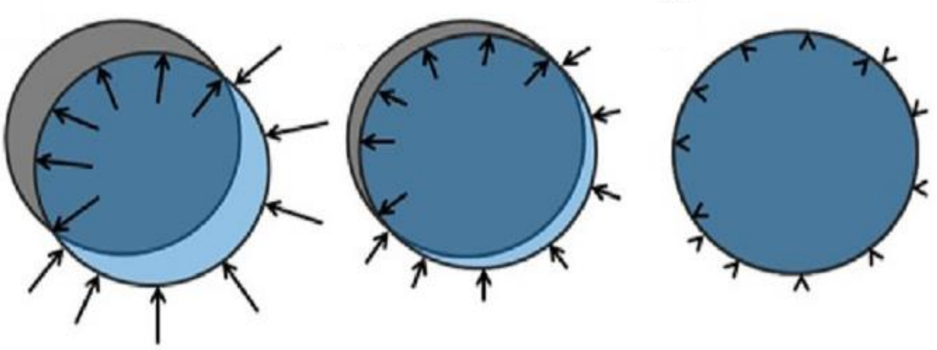

(a) (b) (c)

Figure 2.1Illustration of the demons forces (a) with target image (I_T) in gray and source image (I_S) in transparent blue; the demons indicated by vector arrows warp the image by applying a force in the direction of the image gradient. In (b), there is a better overlap between the images and, as a result, the corresponding force is reduced, indicated by shorter vectors. In (c), the images overlap and there is no applied force by the demons because there is no difference in the gradient.

The method alternates between computation of the forces and regularization by a Gaussian smoothing. The goal of Demons, similar to the OF algorithm, is the minimization of intensity differences between voxels in the target (I_T) and source (I_S) images. The intensity difference between the two images determines the applied force and its direction; when the difference between the two is greater than zero, I_S moves in the direction of I_T ; however, when the difference is less than zero, I_S moves against I_T. The demons stop exerting force when the images overlap completely. The optical flow equation was used to calculate the force applied by the demons, but is renormalized because of the effects of small image intensity gradients. Demons algorithm is a very accurate method, however it requires a great deal of computation time, which is a major drawback for many clinical applications. Furthermore, another limitation of the demons algorithm is that it does not provide diffeomorphic transformations [Vercauteren et al., 2009]. Wang et al. proposed a modified version of the original demons algorithm (implemented for CT image guided RT [(Xie *et al* 2003, Guimond *et al* 2001]) by introducing an ‘active force’ along with an adaptive force strength adjustment during the iterative process [Wang et al., 2005]. This modification led to a 40% speed improvement over the original algorithm and a high tolerance of large organ deformations. The proposed accelerated Demons was tested with: 1) a set of mathematical transformations for a series of patient’s CT images; 2) a physically deformable pelvic phantom; and 3) in physician-drawn contours outlining the tumor volumes and certain anatomical structures in the original CT images along with the CT images acquired during subsequent treatments or during a different respiratory phase for a lung cancer case under different conditions. Their results suggest that the accelerated demons algorithm has significant potential for delineating and tracking doses in targets and critical structures during CT guided RT.

Diffeomorphic registration methods.

Diffeomorphisms is a mathematical condition in which an invertible function, that maps one differentiable manifold to another, exist such that both the differentiable function and its inverse are smooth. For the registration problem, a diffeomorphism means that it preserve the topology of the objects and prevent folding which is often physically impossible. They are considered to be a good working framework when no additional information about the spatial transformation is available. Diffeomorphic image registration usually relies on the computationally heavy solution of some partial differential equations [Avants et al., 2008; Beg et al., 2005]. Vercauteren et al. [Vercauteren et al., 2009] proposed a non-parametric diffeomorphic image registration algorithm based on the demons algorithm. The main idea of the Diffeomorphic Demons (DDem) algorithm is to adapt the entire space of displacement fields optimized by the Demons algorithm to a space of diffeomorphic transformations by combining a recently developed Lie group framework on diffeomorphisms and an optimization procedure for Lie groups. Another widely used algorithm in RT is the Diffeomorphic Morphons (DMor) [Janssens et al., 2009], which is an algorithm based on matching of edges and lines. The difference between this algorithm and OF and DDem is that the computation of the field is based on the local phase difference rather than the intensity difference between images. The phase difference between periodic signals with the same frequency allows the estimation of the spatial difference between these signals. The morphon iteratively deforms a source image into a target image by morphing the moving image [Wrangsjo et al., 2005]. In addition to the diffeomorphism property, methods such as DDem and DMor have the advantages that their transformations are smoother and closer to the true transformations in terms of Jacobians; but their main drawback is the complexity of their methods which results in high computational time. In [Janssens et al., 2011]. a Diffeomrphic version of the Demons and Morphons algorithms were validated in the context of RT for lung cancer patients on several 4D respiratory-correlated CT scans of the thorax with and without variable contrast enhancement. Their results suggest that diffeomorphic methods managed to estimate the deformations in a breathing thorax, with high accuracy, accomplishing the property of invertibility. Moreover, the Diffeomorphic Morphons managed to accurately estimate the deformations between images with variable contrast, while the Demons based method led to misalignment of anatomical structures affected by the contrast variation.

2.3 Validation of registration methods

Because of the impact of image registration in RT, it is important to assess the accuracy of registration methods before being applied in a clinical context. The accuracy of the registration process depends on the quality of the images to be registered, the image information content, the spatial transformation model, cost function and optimization process used to achieved the registration. In addition, the validation of the registration have to take into account the specific experimental protocol, the main purpose why registration would be used, e.g. repositioning of the patient, or recovery of misalignment of OAR and/or TV in images acquired at different times.

Perform a visual inspection is the most immediate way of evaluating the result of a registration process. In this case, expert observers qualitatively evaluated the resulting images and assign a score based on some user-defined criteria; this type of assessment gives a rough idea of the algorithms performance but has the disadvantage of being dependent on the user, different observers may have different opinions about the registration result.

To overcome this limitation, quantitative indices that reflect the performance of the algorithm are used. Pearson's Correlation coefficient (CC) and the Target Registration Error (TRE) are examples of standard indices which provide a global measure of the registration performance [Castadot et al., 2008; Fiorino et al., 2006]. CC is a measure of the correlation between the intensities of corresponding voxels in the two images within a volume *A*, and is defined as:

$$CC = \frac{\sum_{i\in A}(x_i - X)(y_i - Y)}{\sqrt{\left(\sum_{i\in A}(x_i - X)^2\right)\left(\sum_{i\in A}(y_i - Y)^2\right)}}, \tag{2.4}$$

where x_i is the intensity of the ith voxel in the fixed image and y_i is the intensity of the corresponding voxel in the registered image; X and Y are the voxel intensities averaged in the considered volume A. On the other hand, TRE uses markers positioned respectively on the images to be registered, thus is possible to evaluate the distance error between markers. TRE is defined as:

$$TRE = \sqrt{(x_i - x_j)^2 + (y_i - y_j)^2 + (z_i - z_j)^2}\ , \tag{2.5}$$

where (x_i, y_i, z_i) are the coordinates of the markers in the target image and (x_j, y_j, z_j) are the correspondent coordinates in the source image. In this case to obtain a robust validation a large number of markers are needed, this represent a drawback because the definition and positioning of the markers is a highly time-consuming task.

Previous metric examples, as mentioned before, provide a global idea of the registration performance. For a more specific evaluation some metrics design to give information about a particular structure of interest are highly used in RT. These indices need the contours or segmentations of the structures to be analyzed. In this case comparisons are made by volume or center of mass difference evaluation [Lee et al., 2008], through surfaces or contours distance calculation such as the average Symmetric Distance (ASD) or the Maximum Symmetric Distance (MSD) [Heimann et al., 2009] or by volume overlap indices analysis [Dice, 1945; Zouet al., 2004; Faggiano et al., 2011-a; Faggiano et al., 2011-b]. ASD and MSD indices gives information about the mean and worst mismatch found between to structures, they are defined as:

$$\mathrm{ASD(A,B)} = \frac{1}{|\mathrm{C(A)}| + |C(B)|}\left(\sum_{p_A\in C(A)} d(p_A, C(B)) + \sum_{p_B\in C(B)} d(p_B, C(A))\right), \tag{2.6}$$

$$MSD(A,B) = \max\left\{\max_{p_A\in C(A)} d(p_A, C(B)), \max_{p_B\in C(B)} d(p_B, C(A))\right\}, \tag{2.7}$$

where C_A and C_B are the two contours to be evaluated p_A and p_B are the corresponding points to be evaluated in A and B respectively and d(.) is the Euclidean distance between a point p, located in a contour, and its closest voxel in the other contour.

The DICE similarity coefficient indicates the overlapping ratio between the two volumes of interest. It is defined as:

$$DICE = \frac{2 \times |A \cap B|}{|A| + |B|}, \tag{2.8}$$

where A and B are the two sets of voxels to evaluate. The perfect match between the volumes of interest gives a DICE equal to one, whereas two disjoint volumes lead to zero. The main drawback for these indices is the presence of inter-observer and intra-observer variabilities, meaning that the accuracy of the evaluation depends on the accuracy of the contour delineation or the segmentation. For this problem, some approaches to automatically propagate contours or segment structures have been studied. In these cases is necessary to verify if the uncertainties of the automatic contour fall within those achieved by human observers [Duma et al., 2010; Faggiano et al., 2011-b].

It is important to mention that the validation indices described in this chapter are used in clinical settings, despite their drawbacks, since each one of them provides useful information regarding the images or deformation fields obtained by a particular registration method. Furthermore, nowadays it does not exist a common consolidated strategy to perform validation of registration methods because the validation process is highly dependent of the clinical scope of the registration. However, a good strategy for the evaluation of registration methods is to combine several of the indices presented here to get a proper information about the accuracy and robustness of the methods.

Chapter 3

Particle Filter + Optical Flow Registration Approach

After almost three decades that medical image registration methods have been studied [Hill et al., 2001], their major difficulty currently resides in its computational complexity. Although the speed of computers has been growing, the need to decrease the computational time of methods persists. Moreover, the demand for higher robustness and accuracy of the registration usually enforce solutions utilizing the iterations or backtracking, which also produce increase of computational complexity of the method [Maintz et al., 1998; Mani et al., 2013]. In this work we proposed an algorithm with a good balance between accuracy and complexity carrying out, first, a global transformation using the Particle Filter (PF), followed by an iterative Optical Flow (OF) process. The PF is accurate, robust and, because of its parallelizable structure, it can be also considered a fast algorithm; while the proposed iterative OF algorithm is accurate enough and has a considerable lower mathematical complexity with respect to other accurate fluid like algorithms such as Demons and Diffeomorphic Demons.

In this chapter, the basis of the PF and OF is introduced. Then, the theory to adapt both methods to the image registration problem and the proposed algorithm to achieve a 3D elastic registration guided by the proposed PF + OF approach is described.

3.1 Particle Filter

PF is a method based on Bayesian estimation that uses a Monte Carlo algorithm to estimate states of nonlinear dynamic systems by estimating a probability density function [Arulampalam et al., 2002; Ristic et al., 2004]. Monte Carlo methods are very flexible because they do not require any assumptions about the probability distributions of the data. From a Bayesian perspective, sequential Monte Carlo methods make possible to compute a posterior probability distributions of interest parameters. As a result, they are being applied to a large number of engineering problems such as target tracking, computer vision, blind deconvolution, statistical model diagnosis, neural network training, optimal control, reinforcement learning, signal enhancement, financial modeling and time series analysis, among others [Doucet et al., 2001].

3.1.1 Bayesian Estimations Basis

A dynamic system can be modeled with two equations: the state evolution equation and the measurement equation (see figure 3.1). First, to define the state evolution model, consider that the evolution of states of a dynamic system is described by:

$$x_k = f_k(x_{k-1}, v_{k-1}), \tag{3.1}$$

where $f_k()$ is a possibly nonlinear function of the state x_{k-1}, and v_{k-1} is independent and identically distributed (iid) noise. Note that the current state only depends on the previous state, i.e. it is a first order Markov process. Thus, it is possible to recursively estimate the state vectors x_k from a set of measurements described by the following model:

$$z_k = h_k(x_k, n_k), \tag{3.2}$$

where $h_k(\cdot)$ is a measurement function which could also possibly be nonlinear, and n_k are iid noise samples.

Using eqs. 3.1 and 3.2 it is possible to estimate x_k based on the set of available measurements $z_{1:k} = (z_i;\ i = 1, \ldots, k)$ by computing the probability density function (*pdf*) $p(x_k \mid z_{1:k})$. This *pdf* can be obtained recursively defining two stages equations: prediction and update. As it is shown in figure 3.2, suppose that $p(x_{k-1} \mid z_{1:k-1})$ is accessed at time k -*1*, then the *pdf* of the state system at time k can be described in prediction stage via the Chapman-Kolmogorov equation:

$$p(x_k \mid z_{1:k-1}) = \int p(x_k \mid x_{k-1})\, p(x_{k-1} \mid z_{1:k-1})\, ds_{k-1}\ , \tag{3.3}$$

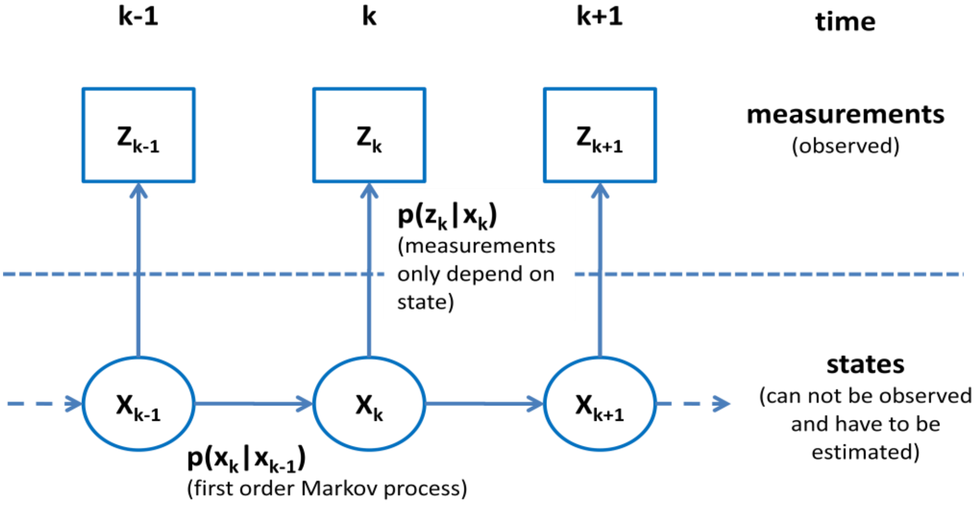

Figure 3.1. Graphical representation of a dynamic system space.

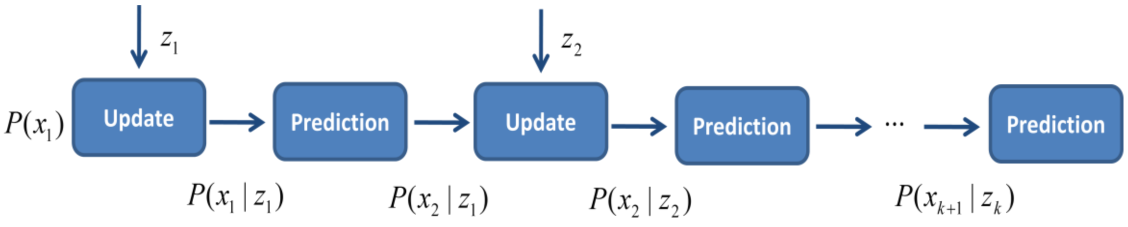

Figure 3.2. Sequence of prediction and update stages.

At time k, a measurement z_k is available. Using the Bayes theorem, we can update the prior (update stage) via:

$$p(x_k \mid z_{1:k}) = \frac{p(z_k \mid x_k)\, p(x_k \mid x_{k-1})}{p(z_k \mid z_{1:k-1})}, \tag{3.4}$$

where the normalizing constant:

$$p(z_k \mid z_{1:k-1}) = \int p(z_k \mid x_k)\, p(x_k \mid z_{1:k-1}) ds_k , \tag{3.5}$$

depends on the likelihood function $p(z_k|x_k)$ defined by the measurement model described on eq. (3.2) and the known statistics of n_k.

In some cases, noises v_k and n_k are independent and Gaussian with known means and covariance. In addition, if functions $f_k(.)$ and $h_k(.)$ are known linear functions, the updated *pdf* $p(x_k|z_{1:k})$ could be given by the well-known Kalman filter [Arulampalam, 2002] if the state variable s_k is continuous.

However, in many applications, functions $f_k(.)$ and $h_k(.)$ are not linear and noises v_k and n_k may not be Gaussian. To solve these cases, the PF becomes an accurate and robust option for practical applications [Ristic, 2004, Doucet, 1998].

3.1.2 Particle Filter Basis

The PF can be seen as a recursive implementation of Monte Carlo based statistical signal processing. The key idea of the PF is to obtain a posterior *pdf* from a set of random samples with associated weights, which allows one to estimate state variables defining a dynamic system [Arce-Santana et al., 2010]. As the number of samples becomes very large, this Monte Carlo characterization becomes an equivalent representation to the usual functional description of the posterior *pdf*, and the PF approaches the optimal Bayesian estimate.

In the PF algorithm, the distribution $p(x_k|z_{1:k})$ is described by samples (*particles*) $\{(x_k^i, w_k^i : i=0, \ldots, N_s)\}$, where the x_k^i represent the particle values at time k, w_k^i are the associated weights such that $\sum w_k^i=1$, and N_s is the number of particles. Then, the posterior density at time k can be approximated as:

$$p(x_k \mid z_{1:k}) \approx \sum_{i}^{Ns} w_k^i \delta(x_k - x_k^i) , \tag{3.6}$$

where δ is the Kronecker delta function. It can be shown that when $Ns \to \infty$, the above approximation can approach the true posterior density $p(x_k|z_{1:k})$.

PF thus consists on the recursive propagation of the weights and support points while each measurement is received sequentially. It is composed of two stages [Arce-Santana et al., 2009]:

1. *Prediction stage*: each of the state variables (particles) is modified using eq. (3.1), through a recursive propagation of the particles at time k.
2. *Update stage:* the weights of the particles are recalculated according to the measurements z_k from eq. (3:2), in order to obtain representative samples of $p(x_k|z_{1:k})$.

It is important to mention that a common problem in the prediction stage is that after a few iterations, all but one particle will have a negligible weight. This phenomenon is known as the Degeneracy Problem [Doucet et al., 1998], and implies that a huge computational effort is devoted to updating particles whose contribution to the approximation of $p(x_k|z_{1:k})$ is almost zero. A suitable measure of degeneracy is the effective sample size *Neff* introduced in [Bergman, 1999] and [Arulampalam et al., 2002], which is defined as:

$$N_{eff} = \frac{N_s}{1+Var(w_k^{*i})} , \tag{3.7}$$

where $Var(w_k^{*i})$ is referred as the true weight which cannot be evaluated exactly. Yet we can obtain an estimate $\hat{N}_{eff}$ of N_{eff} which is described as:

$$\hat{N}_{eff} = \frac{1}{\sum_{i=1}^{Ns} (w_k^i)^2}, \tag{3.8}$$

where w_k^i is the normalized weight. It is clear that effective sample size $N_{eff} \leq Ns$ and a small N_{eff} represents severe degeneracy. The simplest method to mitigate the degeneracy effect is to use a very large number of particles (Ns). However, this will increase computational load, which is often impractical. Therefore, resampling is used as another way to resolve this problem.

The basic idea of resampling is to replace old set of particles, samples, and weights with a new set of samples with their respective new weights such that the sample probability density can better reflect the true posterior density [Ying Liu et al., 2006] (see figure 3.3).

At time $k-1$ the particles that represent $p(x_k|z_k)$ are used to obtain new particles. Then, the stage of each of these particles is modified according to the prediction eq. (3.3). Finally, the weights w_k^i of the particles are updated guided by the likelihood function $p(z_k|x_k)$ in order to get the representative samples of $p(x_k|z_k)$. Weights are normalized before the resampling stage.

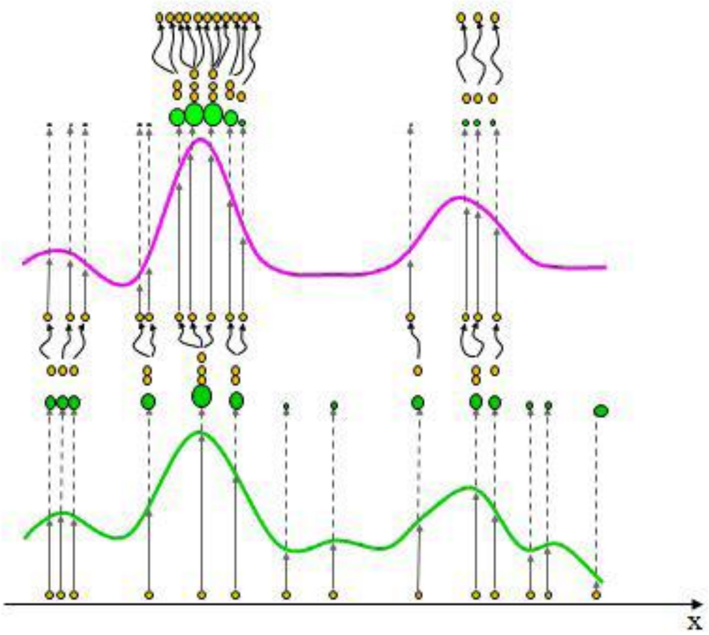

Fig. 3.3. Process of resampling.

3.1.3 Image Registration Based on Particle Filter

In [Arce-Santana et al., 2009], the PF algorithm was adapted to solve the image registration problem in 2D. In this section of the chapter, the extension of the PF algorithm to its 3D implementation is presented. Given a target and a source images, I_T and I_S respectively, the observation model is described as:

$$I_T(x, y, z) = F(I_S(T(x, y, z))), \tag{3.9}$$

where *F(.)* represents an intensity relationship between images, and *T(.)* could be an affine transformation:

$$T([x,y,z]) = \begin{pmatrix} 1 & 0 & 0 & d_x \\ 0 & 1 & 0 & d_y \\ 0 & 0 & 1 & d_z \\ 0 & 0 & 0 & 1 \end{pmatrix} \begin{pmatrix} \lambda_x & 0 & 0 & 0 \\ 0 & \lambda_y & 0 & 0 \\ 0 & 0 & \lambda_z & 0 \\ 0 & 0 & 0 & 1 \end{pmatrix} \begin{pmatrix} 1 & 0 & 0 & 0 \\ 0 & Cos\theta_x & -Sin\theta_x & 0 \\ 0 & Sin\theta_x & Cos\theta_x & 0 \\ 0 & 0 & 0 & 1 \end{pmatrix} \cdots$$

$$\cdots \begin{pmatrix} Cos\theta_y & 0 & Sin\theta_y & 0 \\ 0 & 1 & 0 & 0 \\ -Sin\theta_y & 0 & Cos\theta_y & 0 \\ 0 & 0 & 0 & 1 \end{pmatrix} \begin{pmatrix} Cos\theta_z & -Sin\theta_z & 0 & 0 \\ Sin\theta_z & Cos\theta_z & 0 & 0 \\ 0 & 0 & 1 & 0 \\ 0 & 0 & 0 & 1 \end{pmatrix} \begin{pmatrix} x \\ y \\ z \\ 1 \end{pmatrix}, \qquad (3.10)$$

where $d_{x,}$, λ_x and θ_x are the translation, scale and rotation angle factors on the x axis respectively; $d_{y,}$, λ_y and θ_y are the factors for the y axis; and $d_{z,}$, λ_z and θ_z are the factors for the z axis.

In order to carry out the registration, the state variables are assumed as the vector (s_k^i)=[$d_{xk}^i, d_{yk}^i, d_{zk}^i, \lambda_{xk}^i, \lambda_{yk}^i, \lambda_{zk}^i, \theta_{xk}^i, \theta_{yk}^i, \theta_{zk}^i]^{\mathrm{T}}$ which is formed from the geometric affine transformation parameters. Then the state equation of image registration is defined as a simple random walk:

$$\begin{pmatrix} d_{xk}^i \\ d_{yk}^i \\ d_{zk}^i \\ \lambda_{xk}^i \\ \lambda_{yk}^i \\ \lambda_{zk}^i \\ \theta_{xk}^i \\ \theta_{yk}^i \\ \theta_{zk}^i \end{pmatrix} = \begin{pmatrix} d_{xk-1}^i \\ d_{yk-1}^i \\ d_{zk-1}^i \\ \lambda_{xk-1}^i \\ \lambda_{yk-1}^i \\ \lambda_{zk-1}^i \\ \theta_{xk-1}^i \\ \theta_{yk-1}^i \\ \theta_{zk-1}^i \end{pmatrix} + \begin{pmatrix} v_{d_x} \\ v_{d_y} \\ v_{d_z} \\ v_{\lambda_x} \\ v_{\lambda_y} \\ v_{\lambda_z} \\ v_{\theta x} \\ v_{\theta y} \\ v_{\theta z} \end{pmatrix}, \qquad (3.11)$$

we can see that the prediction equation is just the preceding value disturbed by the noise vector $v = [v_{d_x}, v_{d_y}, v_{d_z}, v_{\lambda_x}, v_{\lambda_y}, v_{\lambda_z}, v_{\theta_x}, v_{\theta_y}, v_{\theta_z}]^T$.

Here, we apply Gaussian and independent noise for each parameter with zero mean and different standard deviation $\sigma_\theta, \sigma_\lambda, \sigma_d$ respectively.

The update equation is given as the equation below in order to evaluate how well each new particle value s_k^i fits the observation model

$$F(I_S(T(x,y,z))) = I_T(x,y,z) + \gamma(x,y,z)\,, \tag{3.12}$$

where the *γ(x, y, z)* is iid noise, with zero mean and standard deviation σ_γ. Because I_T and I_S are considered to be monomodal images, the image intensity at corresponding points between the two images should be the same. In this way is possible to consider *F(.)* as the identity; and the observation model could be described as:

$$I_S(T(x,y,z)) = I_T(x,y,z) + \gamma(x,y,z)\,, \tag{3.13}$$

In order to accelerate the process, we consider a set of *m* uniformly distributed voxels $C = \{(x_i, y_i, z_i); i = 1, \dots, m\}$ in I_T and I_S. Thus, the likelihood function can be described as:

$$p(z_k \mid s_k^i) = \prod_{[x,y,z]\in C} p(I_T(x,y,z), F(I_S(T(x,y,z))) \mid s_k^i)\,, \tag{3.14}$$

In the next section of this chapter, the detail implementation of the image registration guided by the PF is presented.

3.1.4 PF Image Registration Proposed Algorithm

Given a set of N_S particles and their weights at time *k-1*, $\{(s_{k-1}^i, w_{k-1}^i): i = 1,2,\dots,N_S\}$, where the state values are given by the transformation parameters $(s_k^{i-1}) = [\, d_{xk}^{i-1}, d_{yk}^{i-1}, d_{zk}^{i-1}, \lambda_{xk}^{i-1}, \lambda_{yk}^{i-1}, \lambda_{zk}^{i-1}, \theta_{xk}^{i-1}, \theta_{yk}^{i-1}, \theta_{zk}^{i-1}]^{\mathrm{T}}$; the next steps have to be completed in order to achieve the registration process:

1. For each particle, compute the cumulative probability as:

$$c_{k-1}^{0} = 0, \tag{3.15}$$

$$c_{k-1}^{i} = c_{k-1}^{i-1} + w_{k-1}^{i};\ i = 1, 2, \ldots, N_S, \tag{3.16}$$

2. For each particle s_{k-1}^{i}, do the resampling as shown below:

   (a) Generate a uniform random value $u \in [0; 1]$.

   (b) Find the smallest index j such that $c_{k-1}^{i} \geq u$.

   (c) Select the state $s_{k-1}^{\wedge i} = s_{k-1}^{j}$.

3. In the prediction stage, obtain the new samples at time k, using the equation:

$$s_k^i = s_{k-1}^i + v_{k-1}, \tag{3.17}$$

4. In the update stage, for each new particle s_k^i, compute the corresponding weight w_k^i,according to the likelihood function:

$$p(z_k \mid s_k^i) = \prod_{[x,y]\in C} p(I_T(x,y,z), F(I_S(T(x,y,z))) \mid s_k^i), \tag{3.18}$$

5. Normalize the weights, such that $\sum_i w_k^i = 1$. Meanwhile, update the variances of the noise components v_k, in order to gradually reduce the variability in the optimization search.

6. Once the weights of the particles have been computed, we could evaluate the mean of the particles to achieve the estimation:

$$E[d_{xk} \mid z_k] = \sum_{i}^{N_S} w_k^i d_{xk}^i \; , \tag{3.19}$$

$$E[d_{yk} \mid z_k] = \sum_{i}^{N_S} w_k^i d_{yk}^i \; , \tag{3.20}$$

$$E[d_{zk} \mid z_k] = \sum_{i}^{N_S} w_k^i d_{zk}^i \; , \tag{3.21}$$

$$E[\lambda_{xk} \mid z_k] = \sum_{i}^{N_S} w_k^i \lambda_{xk}^i \; , \tag{3.22}$$

$$E[\lambda_{yk} \mid z_k] = \sum_{i}^{N_S} w_k^i \lambda_{yk}^i \; , \tag{3.23}$$

$$E[\lambda_{zk} \mid z_k] = \sum_{i}^{N_S} w_k^i \lambda_{zk}^i \; , \tag{3.24}$$

$$E[\theta_x \mid z_k] = \sum_{i}^{N_S} w_k^i \theta_{xk}^i \; , \tag{3.25}$$

$$E[\theta_y \mid z_k] = \sum_{i}^{N_S} w_k^i \theta_{yk}^i \; , \tag{3.26}$$

$$E[\theta_z \mid z_k] = \sum_{i}^{N_S} w_k^i \theta_{zk}^i \; , \tag{3.27}$$

Step 1 to 5 are iteratively executed until the number of iterations defined by the user are completed or when the estimation of the effective sample size $\hat{N}_{eff}$ is bigger than a threshold N_t, defined by the user.

In the update stage, calculation of the likelihood is based on a similarity measure, i.e. similar gray value distance, mutual information (MI), etc. Since particle filtering is a technique based on Bayesian estimation, it is necessary to define a likelihood function [Simon, 2006, Trees, 2001]. For a given measurement z (between I_T and I_S) and a parameter vector s, the likelihood function $p(z|s)$ could be given as:

$$p(z \mid s) = \frac{1}{\sigma\sqrt{2\pi}} \exp\left\{ -\frac{(SM(I_T(x,y,z), I_S(T(x,y,z))))^2}{2\sigma^2} \right\}, \tag{3.28}$$

where the (x,y,z) are the voxel coordinates on I_T, $T(\cdot)$ is a parametric transformation between I_T and I_S, σ is the noise standard deviation of the measurements, and $SM(:)$ is the similarity metric which is used to compare the two images. Thus, SM should approach zero when similarity between corresponding voxels in both images increases [Reducindo et al., 2010].

Different measures would result in different registration accuracy. Besides, it is performed by using only a selected set of image voxels, and therefore, the number of voxels in this set and how they are sampled may also affect the registration process. In this work we used as similarity metric the normalized mutual information (NMI). Although metrics based on mutual information (MI) are a standard for multimodal registration, it has been proved in [Zhiyong et al., 2006] that NMI performs accurately, is stable and robust in both monomodal and multimodal registration of different dimensions. Moreover, NMI has been proved to be the similarity measure with better performance for parametric registration based on PF [Reducindo et al., 2011]. Given a target and a source images I_T and I_S , the NMI is given by:

$$NMI(I_T, I_S) = \frac{H(I_T) + H(I_S)}{H(I_T, I_S)}, \tag{3.29}$$

where $H(I_T)$ and $H(I_T)$ are the marginal entropies of I_T and I_T respectively, and $H(I_T, I_S)$ is the joint entropy. Based on the NMI properties [Studholme et al., 1999], this metric is always bounded by 2, therefore the SM defined in eq. (3.28) in terms of the NMI is given by:

$$SM(I_T, I_S) = 2 - NMI(I_T, I_S), \tag{3.30}$$

3.2 Optical Flow

3.2.1 Optical Flow Basis

Optical flow (OF) could be defined as the pattern of apparent motion of objects, surfaces, and edges in a visual scene caused by the relative motion between an observer (an eye or a camera or an image acquisition sensor) and the scene [Horn, 1981; Horn, 1993].

Sequences of ordered images allow the estimation of motion as either instantaneous image velocities or discrete image displacements. In general, OF methods try to calculate the motion between two image frames, taken at times t and Δt, at every voxel position. These methods are called differential since they are based on local Taylor series approximations; they use partial derivatives with respect to the spatial and temporal coordinates. For simplicity reasons the 2D+t dimensional OF case is shown, however 3D or n-D cases are similar. In a given image, a voxel located at (x, y, t) with intensity $E(x, y, t)$ will have moved by Δx, Δy and Δt between two image frames, and the following constraint equation can be given:

$$E(x,y,t) = E(x+\Delta x, y+\Delta y, t+\Delta t)\,, \tag{3.31}$$

Assuming voxel movement to be small, eq. (3.31) can be developed using Taylor series as:

$$E(x+\Delta x, y+\Delta y, t+\Delta t) = E(x,y,t) + \frac{\partial E}{\partial x}\Delta x + \frac{\partial E}{\partial y}\Delta y + \frac{\partial E}{\partial t}\Delta t\,, \tag{3.32}$$

From eq. (3.32) it follows that:

$$\frac{\partial E}{\partial x}\Delta x + \frac{\partial E}{\partial y}\Delta y + \frac{\partial E}{\partial t}\Delta t = 0\,, \tag{3.33}$$

$$\frac{\partial E}{\partial x}\frac{\Delta x}{\Delta t} + \frac{\partial E}{\partial y}\frac{\Delta y}{\Delta t} + \frac{\partial E}{\partial t}\frac{\Delta t}{\Delta t} = 0\,, \tag{3.34}$$

$$\frac{\partial E}{\partial x}V_x + \frac{\partial E}{\partial y}V_y + \frac{\partial E}{\partial t} = 0\,, \tag{3.35}$$

where V_x and V_y are the x and y components of the velocity or OF. The derivatives of the image at (x,y,t) can be rewritten as E_x, E_y and E_t respectively, leading to:

$$E_x V_x + E_y V_y = -E_t\,, \tag{3.36}$$

or

$$\nabla E^T \cdot \vec{V} = -E_t\,, \tag{3.37}$$

Equation 3.36 is known as the *instantaneous optical flow equation*. This is an equation in two unknowns and cannot be solved as such. This is known as the aperture problem of OF algorithms; to deal with it and find the optical flow $\vec{V}$ another set of equations is needed, given by some additional constraint. One algorithm that can be used was originally proposed by Horn and Schunck [Horn et al., 1981], which seeks to minimize the following energy function:

$$\xi = \iint \xi_b^2 + \alpha^2 \xi_c^2 dxdy\,, \tag{3.38}$$

where ξ_b is the error in the intensity changes between image frames, or between target and source images, and it is equal to the instantaneous optical flow equation $\xi_b = E_x u + E_y v + E_t$, α is a regularization term to control the flow speed, and ξ_c is the additional constrain which searches to minimize the square of the magnitude of the gradient of the OF velocity, also known as the smoothness measurement of the displacement flow, and is defined as:

$$\xi_c^2 = \left(\frac{\partial u}{\partial x}\right)^2 + \left(\frac{\partial u}{\partial y}\right)^2 + \left(\frac{\partial v}{\partial x}\right)^2 + \left(\frac{\partial v}{\partial y}\right)^2 , \tag{3.39}$$

Other technique to solve the OF is used in [Arce-Santana et al., 2010] which is based on a discrete reformulation of the Horn-Schunck method where it is minimized the next energy function:

$$\Psi(d) = \sum_{\forall r} \left[I_T(r) - I_S(r + d(r)) \right]^2 + \lambda \sum_{<r,s>} \| d(r) - d(s) \|_2^2 , \tag{3.40}$$

where d is the displacement field, r is the coordinates vector of the pixel or voxel, $<r,s>$ represents the nearest neighbors of r, λ is a regularization constant to control the flow homogeneity, and $||.||$ represents the Euclidean norm. In this case the regularization term is expressed in probabilistic terms in the form of a prior Markov Random Field [Marroquin, 2000].

The quadratic cost functions in eqs. (3.38) and (3.40) have a similar structure, since both include a data error term and a regularization term, and in both equations their optimal solution can be computed by solving a system of linear equations for each pixel or voxel using efficient iterative methods such as the Gauss-Seidel technique [Barret et al., 1994].

In this work we develop a variant of the discrete reformulation of the classical Horn-Schunk method studied in [Arce-Sanatana et al., 2010] by adding regularization terms to eq. (3.40) in order to have a finer control in the OF field.

3.2.2 Optical Flow Image Registration Proposed Algorithm

Given a target and source images I_T and I_S in 3D, the energy function proposed to solve the OF includes a data error term and two regularization terms. This energy function is formulated as:

$$\Psi_{opt}(d) = \sum_{\forall r} \left[I_T(r) - I_S(r + d(r)) \right]^2 + \lambda^T \sum_{<r,s>} (d(r) - d(s))^2 + \beta \sum_{\forall r} \| d(r) \|^2 , \tag{3.41}$$

where d represents the displacement flow field, r is the coordinates vector (x,y,z) of a voxel, $<r,s>$ represents the nearest neighbors of r, $\lambda^T = [\lambda_x, \lambda_y \lambda_z]^T$ is the vector containing regularization constants to control the flow homogeneity in every direction of the image, $||.||$ represents the Euclidean norm, and β is a constant that weights the velocity control term of the OF field. Main modifications of the proposed energy function with respect to eq. (3.40) are, first, the use of a vector λ^T in the homogeneity regularization term:

$$\lambda^T \sum_{<r,s>} (d(r) - d(s))^2 , \tag{3.42}$$

instead of a global λ in the regularization term, which gives to the user the possibility to control the homogeneity in every direction of the image according to its resolution; and second, the addition of a velocity regularization term:

$$\beta \sum_{\forall r} \| d(r) \|^2 , \tag{3.43}$$

which controls the velocity of the whole field; big values of β will lead to slow (more controlled) displacements of the OF field. The non-linear quadratic cost function (3.41) can be linearized by conducting a first order Taylor approximation on the data term:

$$I_S'\big(\mathbf{r} + d(\mathbf{r})\big) \approx I_S'(\mathbf{r}) + \nabla I_S'(\mathbf{r})^T d(\mathbf{r}), \tag{3.44}$$

Then, the minimum solution for the quadratic problem can be obtained by a direct calculation of the stationary optimality conditions of eq. (3.41) with respect to $d(\mathbf{r})$:

$$\begin{aligned}\frac{\partial \Psi_{opt}(d)}{\partial d(r)} &= -2G(r)\nabla I_S(r)^T + 2\nabla I_S(r)^T d(r)\nabla I_S(r)^T \\ &\quad + 2N_s\lambda^T d(r) - 2\lambda^T \sum_{s\in<r,s>} d(s) + 2\beta d(r)^T\end{aligned}, \tag{3.45}$$

where $G(r) = I_T(r) - I_S(r)$ and $\nabla I_S(r) = [\nabla_x(r) \quad \nabla_y(r) \quad \nabla_z(r)]^T = \left[\frac{\partial I_S(r)}{\partial d_x} \quad \frac{\partial I_S(r)}{\partial d_y} \quad \frac{\partial I_S(r)}{\partial d_z}\right]^T$

Rearranging eq. (3.45) we obtain:

$$G(r)\nabla I_S(r)^T + \lambda^T \sum_{s\in<r,s>} d(s) = \nabla I_S(r)^T d(r)\nabla I_S(r)^T + N_s\lambda^T d(r) + \beta d(r)^T, \tag{3.46}$$

which can be express in terms of each dimension of the image as follows:

$$\begin{aligned}G(r)\nabla_x(r) + \lambda_x \sum_{s\in<r,s>} d_x(s) &= \nabla_x(r)^2 d_x(r) + \nabla_x(r)(\nabla_y(r)d_y(r) + \nabla_z(r)d_z(r)) \\ &\quad + N_s\lambda_x d_x(r) + \beta d_x(r)\end{aligned}, \tag{3.47}$$

$$\begin{aligned}G(r)\nabla_y(r) + \lambda_y \sum_{s\in<r,s>} d_y(s) &= \nabla_y(r)^2 d_y(r) + \nabla_y(r)(\nabla_x(r)d_x(r) + \nabla_z(r)d_z(r)) \\ &\quad + N_s\lambda_y d_y(r) + \beta d_y(r)\end{aligned}, \tag{3.48}$$

$$\begin{aligned}G(r)\nabla_z(r) + \lambda_z \sum_{s\in<r,s>} d_z(s) &= \nabla_z(r)^2 d_z(r) + \nabla_z(r)(\nabla_x(r)d_x(r) + \nabla_y(r)d_y(r)) \\ &\quad + N_s\lambda_z d_z(r) + \beta d_z(r)\end{aligned}, \tag{3.49}$$

Finally, the solution to the optimization problem in (3.41) is obtained by solving the system of linear equations depending of $d_x(r)$, $d_y(r)$ and $d_z(r)$, described by (3.47), (3.48) and (3.49), which can be solved for iteratively with Gauss-Seidel.

3.3 Particle Filter + Optical Flow Image Registration Approach

The theorical basis of PF and OF presented in this chapter can be summarized as follows. Given a source and target images I_S and I_T, first, the basic idea of the parametric registration based on PF is to estimate the parameters vector Par of a geometrical transformation (e.g. affine) by an stochastic search over an optimization surface (cost function). This goal is achieved by using a set of N_s test points called particles $\left(Par_1, \cdots, Par_{N_s}\right)$, and their associated weights $\left(W_1, \cdots, W_{N_s}\right)$ calculated by a *likelihood* function $p\left(z|Par_j\right)$ for a measurement z between the images:

$$W_j = \frac{1}{\sqrt{2\pi}\sigma_\eta} \exp\left\{\frac{-\left(2 - \mathrm{NMI}\left\{I_T(\mathbf{r}), I_S\left(T\left(\mathbf{r}|Par_j\right)\right)\right\}\right)}{2\sigma_\eta^2}\right\}, \qquad j = 1, \cdots, N; \tag{3.50}$$

where **r** is the coordinates vector *(x,y,z)* of a voxel, $T(\mathbf{r}|Par)$ is a geometrical transformation depending on the parameters vector Par, σ_η^2 is the noise variance in the measurement z, and $\mathrm{NMI}(\cdot,\cdot)$ represents the normalized mutual information between two images.

Weights W_j are used to approximate *a posteriori pdf* $p\left(Par_j|z\right)$ of the unknown parameters vector Par given a measurement z. In this way, for a window of k observations $(z^1, \cdots, z^k)$, the estimated vector $\widehat{Par}^k$ of the parametric transformation can be computed by the expected value of the approximated *pdf* as follows:

$$\widehat{Par}^k = E[Par|z^1, \cdots, z^k] \approx \sum_{j=1}^{N} W_j^k Par_j^k, \tag{3.51}$$

Once carried out the initial parametric registration by using the PF, the remaining displacements $d(\mathbf{r})$ are obtained by using an OF technique, in particular by minimizing the non-linear quadratic energy function described in eq. 3.41,

$$\Psi_{opt}(d) = \sum_{\forall r}\left[I_T(r) - I_S(r + d(r))\right]^2 + \lambda^T \sum_{<r,s>}(d(r) - d(s))^2 + \beta \sum_{\forall r} \| d(r) \|^2 .$$

This non-linear quadratic cost function in can be linearized by conducting a first order Taylor approximation on the data term, as shown in eq. (3.45), and the solution for the quadratic problem can be obtained deriving with respect to $d(\mathbf{r})$, and then solving the resulting system of linear equations (equation 3.47, 3.48 and 3.49) by the iterative Gauss-Seidel technique.

Hence, the initial estimation $d_0(\mathbf{r})$ can be refined by accumulating the displacements obtained after solving the optimization in (3.45) recursively. Thus, the PF+OF elastic registration algorithm can be achieved in the next three steps:

1. Parametric Registration (Rigid). Find the parameters vector $\widehat{Par}$ of the perspective transformation $T\left(\mathbf{r}|\widehat{Par}\right)$ that provide the best alignment between $I_T(\mathbf{r})$ and $I_S(\mathbf{r})$, and compute the initial (rigid) displacement vector field $d_0(\mathbf{r})$.
2. Optical Flow. Find the displacements between I_T and $\tilde{I}_S$ by an OF iterative scheme, $d(\mathbf{r}) = d_1(\mathbf{r}) + d_2(\mathbf{r}) + \cdots + d_k(\mathbf{r})$, until convergence is achieved; where at each k-th iteration the OF is computed over $I_T(\mathbf{r})$ and $\tilde{I}_S^k(\mathbf{r})$, where $\tilde{I}_S^k(\mathbf{r}) \triangleq \tilde{I}_S\left(\mathbf{r} + \sum_{\boldsymbol{i=1}}^{\boldsymbol{k-1}} d_i(\mathbf{r})\right)$.
3. Elastic Registration. Finally, we can obtain the vector field of the non-rigid deformation by adding the rigid vector field to the one obtained by the iterative OF, i.e., $V(\mathbf{r}) \triangleq d_0(\mathbf{r}) + d(\mathbf{r})$. Consequently, we can deduce the elastic registered image as $I_R(\mathbf{r}) \triangleq I_S\left(\mathbf{r} + V(\mathbf{r})\right)$.

Chapter 4

PF+OF for Registration of 4D CT Lung Images - Experimental Protocol

In this chapter, the experimental protocol to evaluate the developed algorithms, PF, OF and the combination of them, PF+OF, using two datasets is presented. First, a 4D CT lung images dataset from a controlled model was studied; then a dataset of 4D CT lung clinical images from five patients treated with RT was used to analyze the performance of the proposed registration approaches. In addition, performance comparison between the proposed methods and other non-parametric algorithms already proposed in RT for the registration process in the thoracic district [Wang, 2005; Peyrat, 2008; Murphy, 2011], Demons (Dem) and Diffeomorphic Demons (DDem), is performed analyzing anatomical structures of clinical interest.

4.1 Controlled Images Dataset

As a first step, registration algorithms were evaluated using the POint-validated PIxel-based (POPI) breathing thorax model provided by [Vandemeulebroucke et al., 2007].

The POPI model consists of a dataset of 4D CT thorax images binned into 10 respiratory phases (00%, 10%, 20%, ..., 90%) acquired from a real patient (figure 4.1); in addition to the images, authors provide also 41 associated anatomical landmarks with their respective spatial information (spatial coordinates). The landmarks are anatomically homologous points that were manually delineated by radiologists at all 10 phases of the original 4D CT image sets based on anatomical features that correspond to various locations in the lung such as carina, calcified nodules, division branch of pulmonary artery, etc. Landmarks were used to evaluate the registration accuracy by the estimation of the distance between markers before and after the registration process. The POPI model consisted of CT images of 512× 512×141 voxels with a voxel dimensions of 0.97 × 0.97 × 2.00 mm^3 (2.00 mm is the slice thickness). CT images from phase 10 (onset of inspiration) were always used as the target image I_T, the nine remaining phases were used as the source image I_S, thus leading to a total of nine registrations.

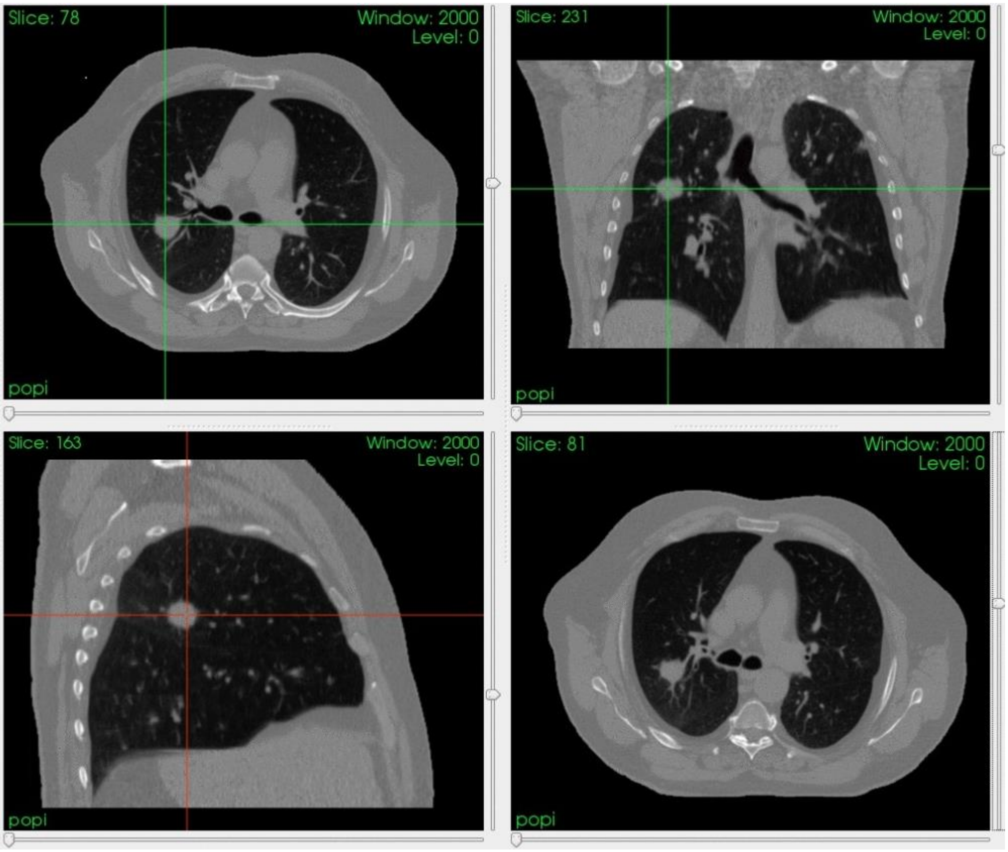

Figure 4.1. POPI model 4DCT image with the respective axial, sagittal and coronal view of the gross target volume (GTV).

4.2 Clinical Images Dataset

Clinical images dataset was formed by 4D CT images from studies of 5 patients treated for locally advanced NSCLC with Helical Tomotherapy (HT). For each patient, images from the inspiratory and expiratory phases were registered, using the first one as target image; an example of the complex deformation found between the inspiratory and expiratory phases is shown in figure 4.2. In figure 4.3, an example of the CT image from an inspiratory phase is shown, in which contours of the lungs and the tumor are delineated with the correspondent RT dose planning, where the most irradiated zone correspond to the purple one (GTV); the upper right image shows a volumetric representation of the right lung (green), left lung (blue) and GTV (purple) are also presented. For this images dataset, registration methods were used with the purpose of the alignment of volumetric structures of interest, which leads to the recovery of information about the movement of lungs and tumor due to respiration, information that could be used for the definition/modification of the dose distribution of the RT treatment plan. Furthermore, the robustness of the proposed algorithm is tested taking into account the intra-subject variability, where different morphologies of the anatomical structures of interest, tumor (TV) and lungs, are presented (figure 4.4). The number of slices in these images ranged from 72 to 128, and each slice was 512 x 512 pixels with a voxel size equal to 0.98 x 0.98 x 2.50 mm^3.

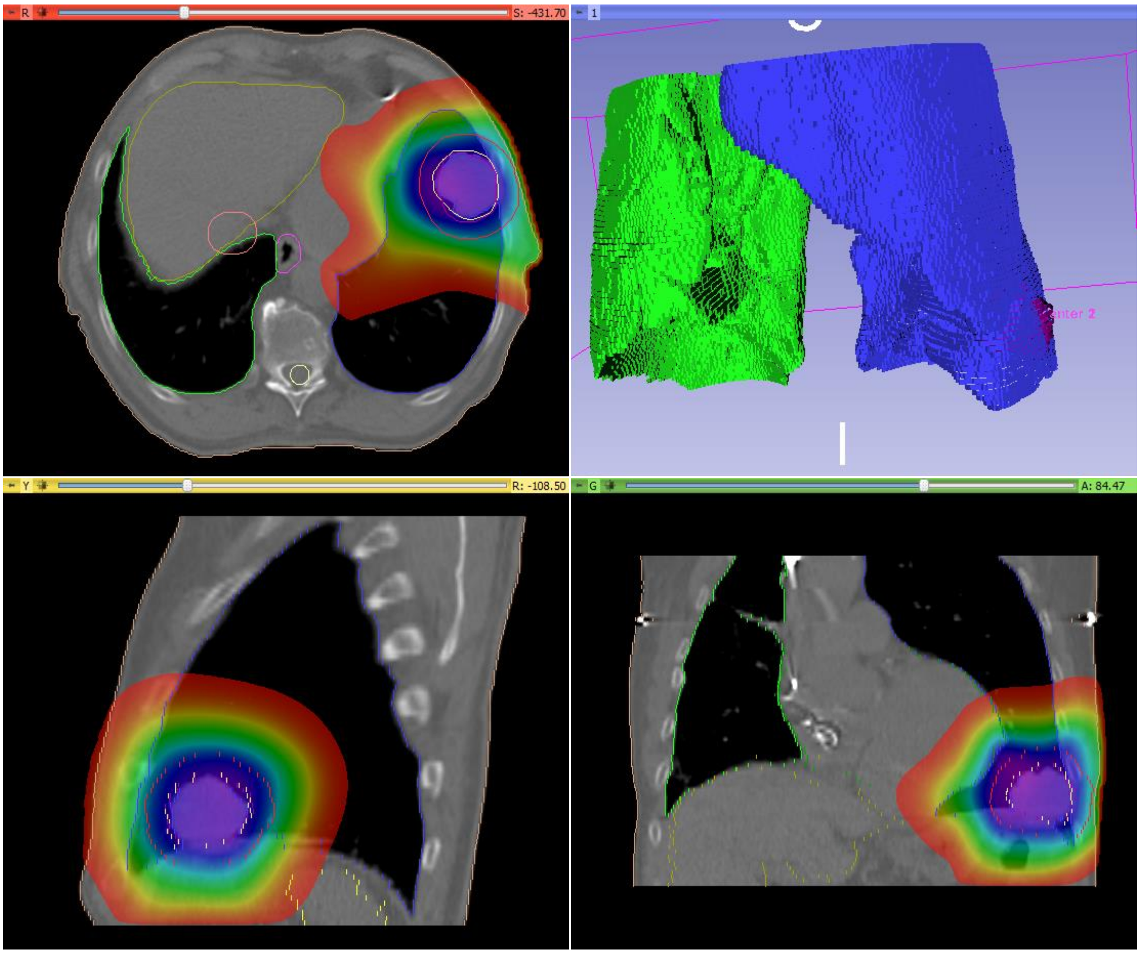

Figure 4.2. Example of a CT image from the thoracic district used for the RT dose planning.

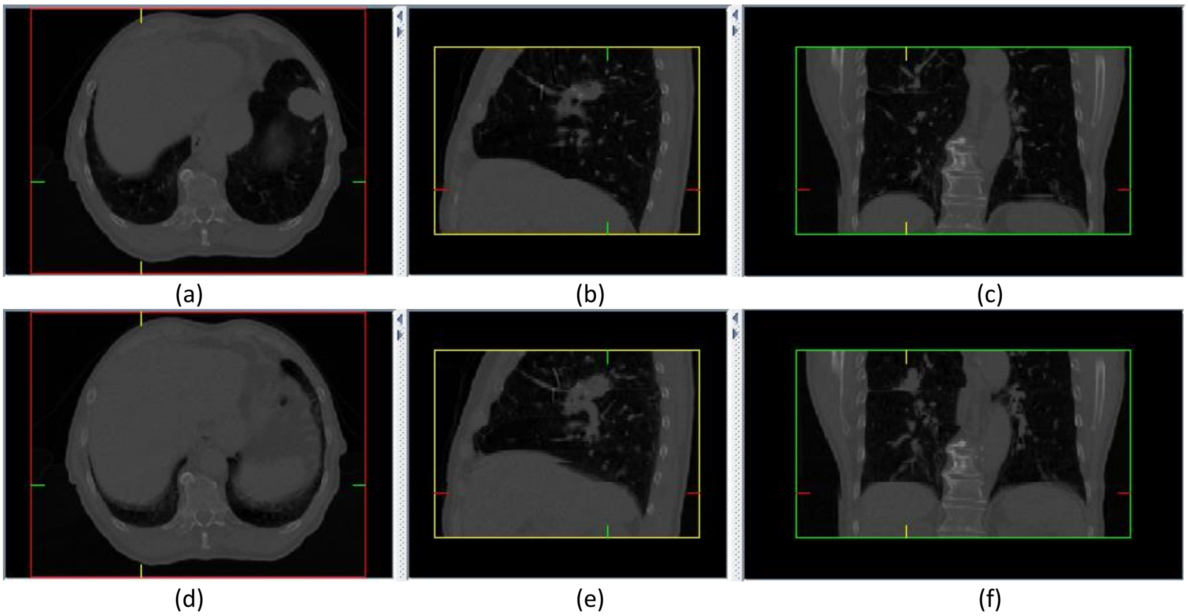
(a) (b) (c)

(d) (e) (f)

Figure 4.3. Example of the complex lung deformation found between the inspiratory ((a), (b) and (c)) and expiratory ((d), (e) and (f)) phases presented in their respective axial, sagittal and coronal view.

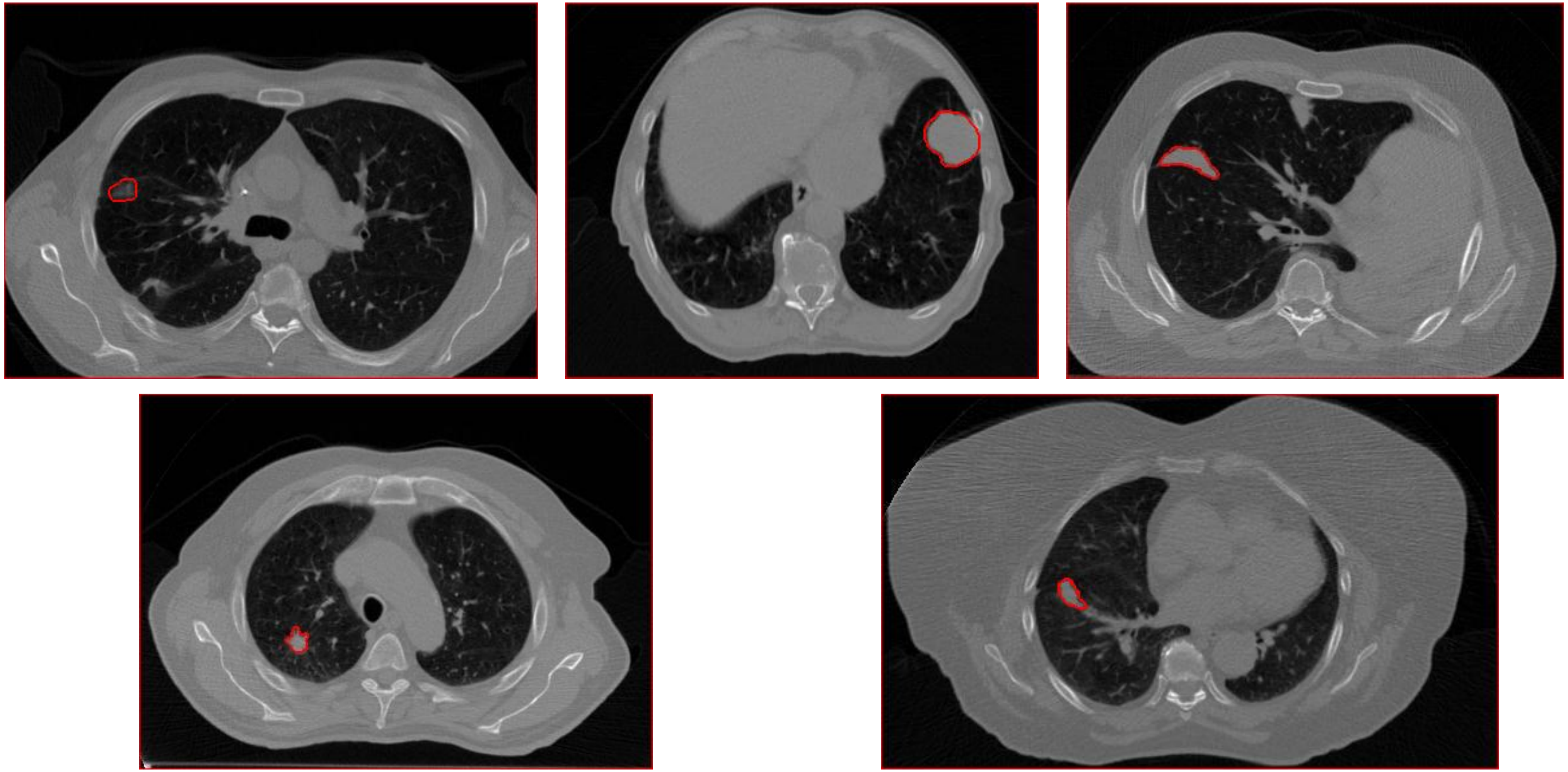

Figure 4.4. Visualization of the 4D CT lung images studied from five patients treated for locally advanced non-small cell lung cancer (NSCLC). For each patient the tumor is located by a red contour.

4.3 Pre-processing

In order to reduce the computing time of the registration process, reduction of all volumetric images was performed without losing useful information, eliminating only the unnecessary areas which had no relevant information related to the lungs. The reduction of the images was performed using the software MIPAV [McAuliffe et al., 2001]. Three or four slices in excess of the district of interest at the front and back of the image were used as rule to reduce the images, to avoid that any artifacts introduced by the registration process could interfere with the sections containing the structures of interest. In addition, several background voxels corresponding to the air surrounding the patient were eliminated, however representative voxels of this area near the district of interest are considered; the reason to eliminate theses voxels is, because of noise in the image background voxels have slightly different values to the ideal background value (around -1000) and even if these voxels are not strictly part of the district of interest, they are considered by the registration algorithms. The last pre-processing step was the reassignment of the origin. This procedure is necessary because the reduction of the volume modify the size of the image in every direction moving the origin of image, which always corresponds to the upper left corner of the first slice in agreement with the RAI (Right to left, Anterior to posterior, Inferior to superior) convention (figure 4.5).

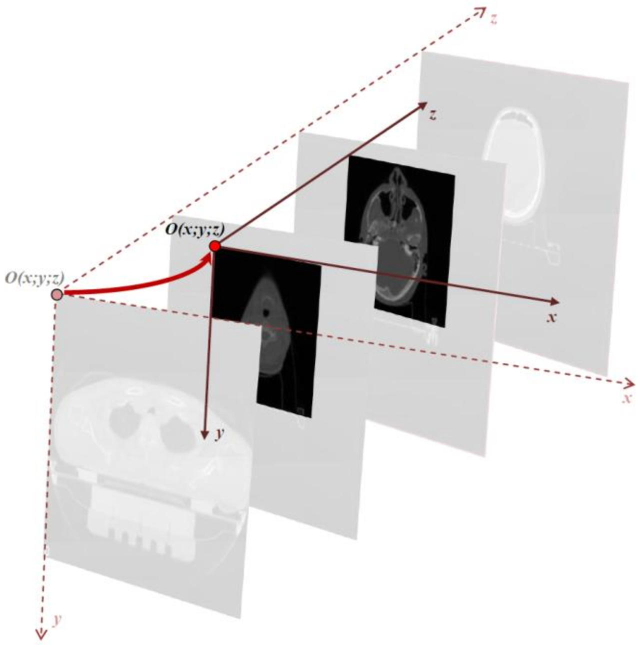

Figure 4.5. Example of reassignment of an image origin.

4D CT images from the POPI model, after the pre-processing steps, consisted of 422x300x51 voxels; due to the reduction on the images, the original 41 markers provided were cut off to 30 landmarks. 4D CT images from the clinical dataset remained with a variable dimension from 365x282x48 to 472x332x128 voxels after the pre-processing stage.

4.4 Implementation and Parameters of Image Registration Algorithms

The proposed registration algorithms have been implemented using C++language and the standard libraries included in the Insight Toolkit (ITK) v.4.2 [Ibanez et al., 2003]. For PF, the settings for all registrations included 500 particles and a maximum of 500 iterations; the iterative process stops when it reaches the maximum number of iterations or when the estimation of the effective sample size $\hat{N}_{eff}$ is bigger than the stop criteria N_t $=1x10^{-6}$. Estimation of OF was achieved with a maximum of 300 iterations and smoothness control parameters $\lambda_x = 6000$, $\lambda_y = 6000$, $\lambda_z = 15000$ and $\lambda_w = 200000$; the OF iterative process was stopped if the changes measures in terms of the sum of squared differences (SSD) were less than 1.0%. Dem and DDem algorithms were implemented, also in C++ language, in an iterative and multiscale scheme with the same settings proposed by the authors [Janssens et al., 2009], that is using eight scales with a maximum of 20 iterations at each scale and a Gaussian smoothing with a standard deviation $\sigma=2$.

Registrations were executed in a standard PC with an Intel Core i5 CPU running at 2.27GHz. Registration times were about 6 min for Dem, 10 min for DDem, 55 min for PF and 20 min for OF. It is important to mention that in this work the comparison between the proposed method PF+OF, Dem and DDem was evaluated in terms of the registration accuracy and not in terms of executing time; in the present implementation PF and OF are not adopted multi-resolution schemes, thus leading to speed computational disadvantages. In a near future this drawback will be overcome by a multiscale implementation of the PF+OF approach, however in this work speed processing was not considered as an important factor to evaluate the proposed NRR method PF+OF, eliminating the computational time advantage of the multiscale implementation of Dem and DDem.

4.5 PF+OF – Original Version vs. Four Control Parameters Version

For a better understanding of reasons to add control parameters to the presented 3D implementation of the OF approach originally proposed by [Arce-Santana, et al., 2010], which have only one control parameters (see eqs. 3.40 and 3.41), two particular registration were performed. In these experiments, phases 10, 30 and 60 from the POPI model were used, to perform the registration between phases 10-30 and 10-60 (in both cases phase 10 was used as the target image). These phases were selected in order to evaluate the performance of the two versions of the PF+OF approach with two different patterns of complex deformation, beginning of the inspiration (phase 10) versus the middle of the inspiration (phase 30) and the onset of the expiration (phase 60), being the last one the more complex deformation.

The value of λ for the PF+OF version with one control parameter was set to 6000 (as λ_x and λ_y); the rest of the algorithm parameters were set as described in section 4.4 of this chapter.

4.6 Registration Accuracy

In order to validate the registration accuracy, for each registration method the manual segmentation of anatomical structures of interest, the lungs and the tumor (Gross Target Volume - GTV), were performed by expert observers in RT images using the Treatment Plan System (TPS).

From these segmentations, differences in structures between correspondence respiratory phases registered before and after the registration process were calculated using standard indices usually adopted for registration accuracy assessment [Wang et al., 2008; Heimann et al., 2009; Faggiano et al., 2011-a; Ecabert et al., 2011]: the Dice similarity coefficient (DICE), the Average Symmetric Distance (ASD), the Maximum distance between structures (DMax), and the Percentage of Distance Bigger than the Voxel Dimension (%DBVD). For the POPI model, the Target Registration Error (TRE) was also computed.

DICE is an index that measures the overlap between two structures described by binary masks. Hence given two different binary masks A and B representing the area delimited by a contour, DICE was calculated as:

$$DICE = 2\frac{\#(A \cap B)}{\# A + \# B} \tag{4.1}$$

where # denotes the cardinality of the set. DICE ranges from 0 (no spatial overlap) to 1 (complete overlap).

Likewise, given two contours C_A and C_B, the ASD index first calculates for each contour pixel $p_B \in C_B$, the Euclidean distance between p_B and its closest pixel in C_A. In order to provide symmetry, the same process is applied to the contour pixels $p_A \in C_A$ with respect to C_B. The ASD is then defined as the average of all computed distances:

$$ASD = \frac{1}{|C_A| + |C_B|}\left(\sum_{p_A \in C_A} d(p_A, C_B) + \sum_{p_B \in C_B} d(p_B, C_A)\right) \tag{4.2}$$

where $d(p,C) = min_{q \in C} ||p-q||_2$. Therefore, a perfect match between contours C_A and C_B is expressed as a zero value for ASD.

DMax calculates the maximum distance between the analyzed overlapped contours, where zero means a perfect overlap. As a result, DMax provides an estimation of the worst local distance mismatch and is defined as:

$$DMax = \max\left\{\max_{p_A \in C_A} d(p_A, C_B), \max_{p_B \in C_B} d(p_B, C_A)\right\} \tag{4.3}$$

%DBVD estimates the percentage of mismatching distances bigger than a permissive threshold value, defined by the user, such as the thickness of the voxel, being 0% a perfect match between structures. Given two sets G_A and G_B defined as:

$$G_A = \{p_A \in C_A \mid d(p_A, C_B) > VoxelDim\} \tag{4.4}$$

$$G_B = \{p_B \in C_B \mid d(p_B, C_A) > VoxelDim\} \tag{4.5}$$

where *VoxelDim* is the image voxel dimension (slice thickness) value, then the %DBVD is calculated as follows:

$$\%DBVD = \frac{\#G_A + \#G_B}{\#C_A + \#C_B} x100 \tag{4.6}$$

TRE index is the residual misalignment between the original landmarks positions in the target image (x_i, y_i, z_i) and the updated positions (x'_i, y'_i, z'_i) obtained after applying the transformation field to landmarks in the source image; TRE is define as follows:

$$TRE = \sqrt{(x'_i - x_i)^2 + (y'_i - y_i)^2 + (z'_i - z_i)^2} \tag{4.7}$$

4.7 Comparison

In this work, the PF and OF algorithms were tested individually and together as the proposed PF+OF approach; individual evaluation of the algorithms was assessed for a better understanding of the impact of the affine transformation, achieved by PF, in the proposed OF algorithm. Thus, the comparison of the registration accuracy was performed between accuracy values computed before the registration and values obtained after the registration by PF, OF, Dem, DDem and PF+OF approaches.

For the POPI model, accuracy indices were calculated using the lung segmentations provided together with the 4D CT images, and 30 anatomical landmarks. For the clinical dataset, segmentations of the lungs and GTV were considered for the computing of registration accuracy indices; no landmarks were available for this dataset, therefore the TRE index was not considered for the evaluation.

After a rejection of normality on the data in both datasets, for each accuracy index, a Kruskall-Wallis test was performed to assess the presence of significant differences among the studied methods ($p<0.05$). Then, a comparison between each possible pair of algorithms was performed by a Wilcoxon rank-sum test to verify significant differences between each registration approach.

Chapter 5

Results

5.1 Registration Accuracy on the POPI Model

5.1.1 PF+OF versions comparison

The experiments designed to show the differences between using one or four control parameters in the PF+OF approach are presented in figures 5.1 and 5.2. Figure 5.1 exhibits the 10-30 phases registration result obtained by both versions of the algorithm, where is possible to observe that both algorithms were capable to recover the warps caused by this particular respiratory motion. The 10-60 registration results are presented in figure 5.2, where is possible to observe that considering the largest deformation found within the POPI model, inspiration and expiration phases images, it is possible to observe a proper recovery of the misalignments by the proposed PF+OF version with four control parameters, while the one control parameter version is capable to recover the respiratory motion but adds artefact to the image due to inhomogeneities in the deformation field.

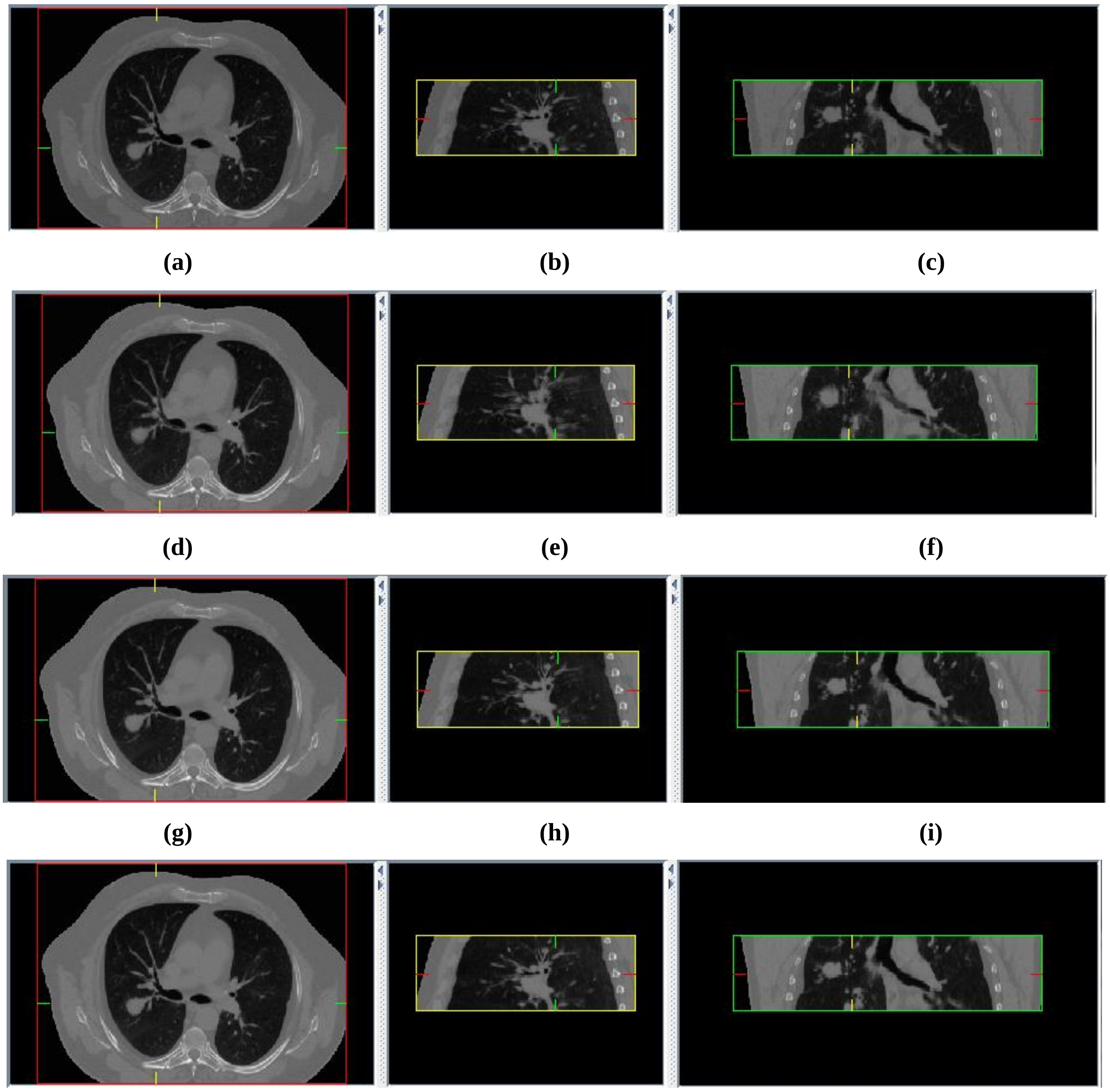

(a) **(b)** **(c)**

(d) **(e)** **(f)**

(g) **(h)** **(i)**

(j) **(k)** **(l)**

Figure 5.1. Comparison between PF+OF versions. Images correspond to: POPI model phase 10 image (I_T), sub-images (a), (b) and (c); POPI model phase 30 image (I_S), sub-images (d), (e) and (f); registration result obtained by the PF+OF with one control parameter, sub-images (g), (h) and (i); registration result obtained by the PF+OF with four control parameters, sub-images (j), (k) and (l). Each image is viewed by its axial, sagittal and coronal anatomical planes.

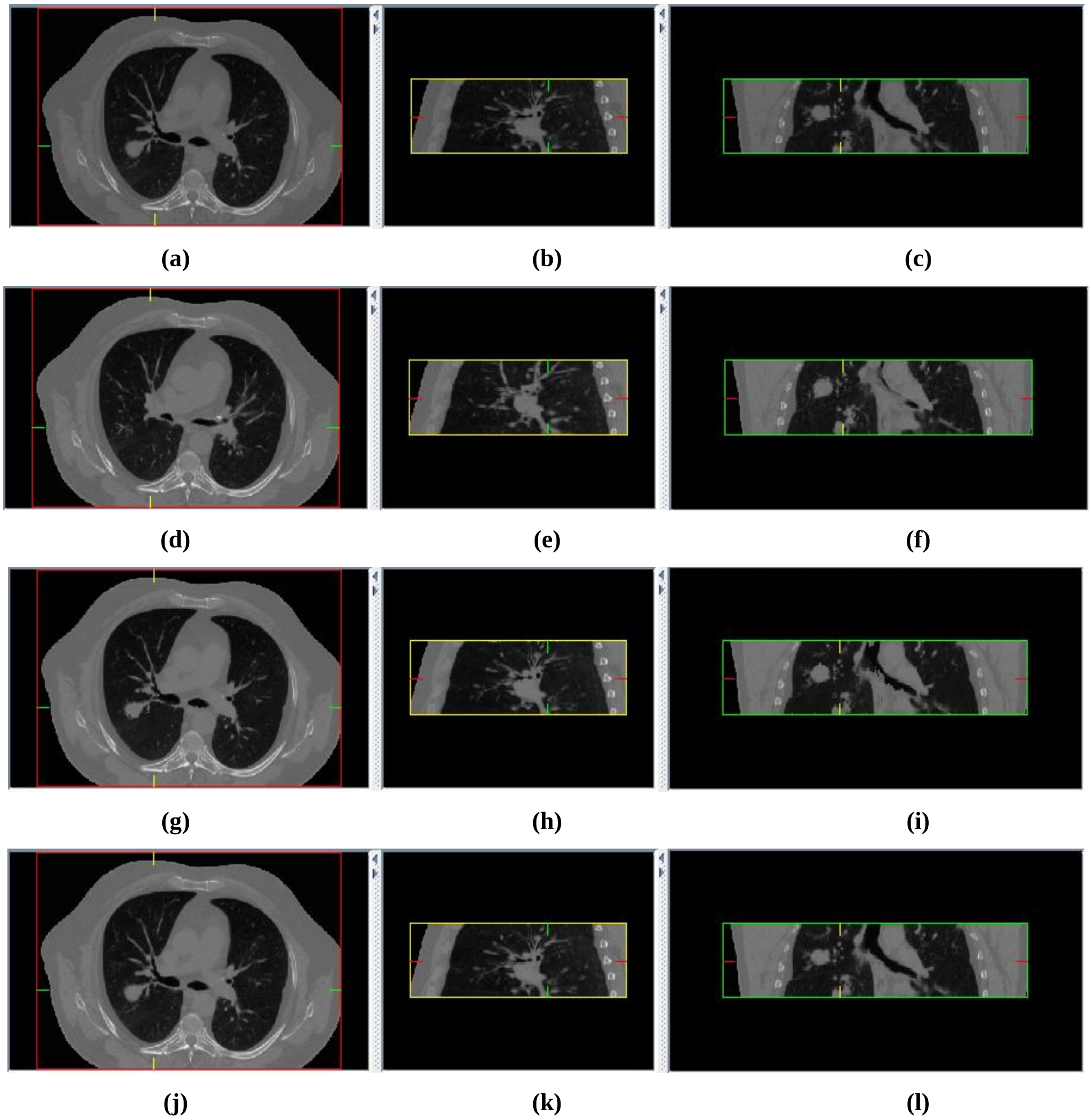

(a) (b) (c)

(d) (e) (f)

(g) (h) (i)

(j) (k) (l)

Figure 5.2. Comparison between PF+OF versions. Images correspond to: POPI model phase 10 image (I_T), sub-images (a), (b) and (c); POPI model phase 60 image (I_S), sub-images (d), (e) and (f); registration result obtained by the PF+OF with one control parameter, sub-images (g), (h) and (i); registration result obtained by the PF+OF with four control parameters, sub-images (j), (k) and (l). Each image is viewed by its axial, sagittal and coronal anatomical planes.

5.1.2 Algorithms comparison on the POPI model

Figure 5.3 shows an example of the registration results obtained by the different registration algorithms studied in this work using the POPI model in terms of the analysis of the lungs; in particular, here is shown the registration between the most distant respiratory phases (10 and 60). In figures 5.1 (a) to 5.1 (e) is possible to visually assess each algorithm (PF-(a), Dem - (b), DDem - (c), OF - (d), PF+OF -(e)) by comparing their corresponding lung contours with the ones of the source image before the registration process (orange contours). Figure 5.1 (f) is a zoom in the zone of the gross target volume (GTV) in which contours of the four NRR algorithms studied in this work are superimposed to the target image, where is possible to observe that Dem, DDem and PF+OF (yellow, blue and green contours respectively) have similar performance, and that OF (red contour) behaves similarly to the other NRR algorithms in the border of the lung but presents some misalignments when considering the GTV zone.

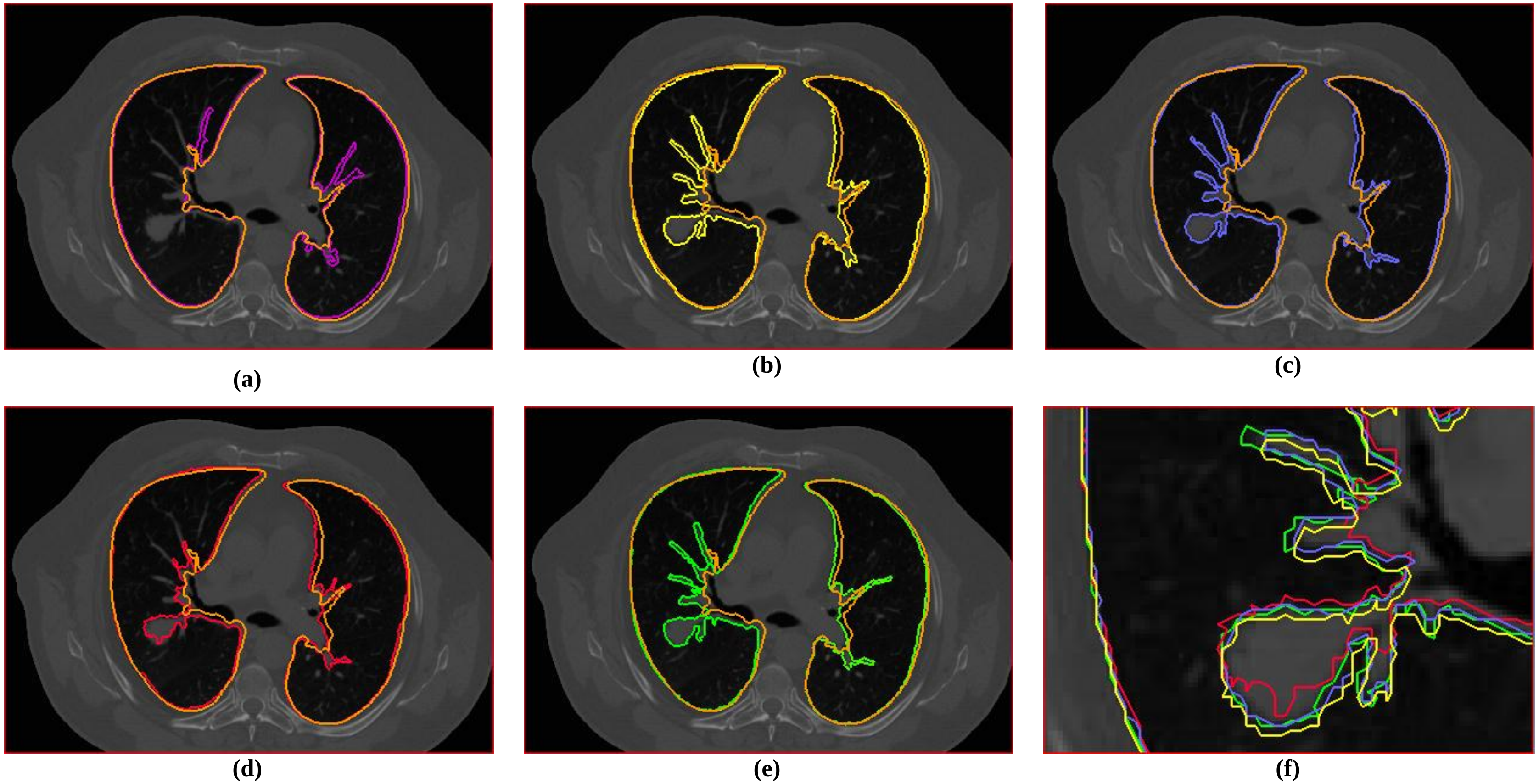
(a) (b) (c)

(d) (e) (f)

Figure 5.3. Results achieved by the analyzed registration methods using phases 10 (target image) and 60 (source image) of the POPI model. Figures (a) to (e) present the phase 10 image with two superimposed lungs contours: lungs contours of the phase 60 image before the registration process (orange), and lungs contours of the phase 60 image after the registration using : (a) Particle Filter (PF) - purple, (b) Demons (Dem) - yellow, (c) Diffeomorphic Demons (DDem) - blue, (d) Optical Flow (OF) - red and (e) PF followed by OF (PF+OF) - green. Figure (f) shows a zoom into the tumor zone where contours of Dem, DDem, OF and PF+OF are presented superimposed for visual comparison.

Tables 5.1 to 5.5 present the overall results by using the accuracy indices described in chapter 4. For each index, six conditions were analyzed: before registration (1-Pre), and after each registration with the studied algorithms: Particle Filter (2-PF), Demons (3-Dem), Diffeomorphic Demons (4-DDem), Optical Flow (5-OF) and PF followed by OF (6-PF+OF). Complementing each table, figures 5.4 to 5.8 present the correspondent box plot in order to have a visual representation of the performance for each registration algorithm on every index.

Table 5.1 present the results for the ASD index, where is possible to observe that all four NRR methods improve the ASD value with respect to Pre and the RR performed by the PF; for this index the best value is achieved by PF+OF (0.87±0.12 mm). Significant differences were found between the 4 NRR methods with respect to Pre and PF; in addition PF+OF was also significantly different from DDem, but not from the rest of the NRR approaches. Figure 5.4 gives a visual representation that the performance is similar between Dem, DDem, OF and PF+OF (all with a mean and median values less than 1 mm).

DICE results are presented in table 5.2. also for this index, all 4 NRR algorithms have a better mean value (0.96) against Pre and PF values (0.94); taking into account the median value, PF+OF is slightly better (0.01 bigger) than the rest of the NRR methods. This fact is possible to be observed in figure 5.5. For this index, significant differences were found between the 4 NRR approaches with respect to Pre, and only OF and PF+OF were also significantly different with respect to PF; however no significant differences were found among NRR methods.

Results for the DMax index are shown in table 5.3, where is possible to observe that NRR methods decrease the Pre and PF DMax values around 2 mm; particularly DDem presented the best mean value (31.66±1.52 mm) being 1.46 mm (4%) smaller than the proposed PF+OF algorithm. In addition, only Demons based methods are statistically different from Pre, and DDem was also significantly different from PF and OF; PF+OF did not present statistically differences at all. In figure 5.6 is possible to observe that all NRR registration algorithms improve DMax by decresing the Pre value at least 2 mm, and corroborate that the best performances, in terms of the median value, were obtained by Dem and DDem.

Table 5.4 shows the results for %DBVD index; in this case all registration algorithms (PF and the 4 NRR methods) show a significant improve with respect to Pre, but only registration algorithms involving the OF process were significantly different with respect to PF, and the best performance correspond to PF+OF with a mean value of 8.77±9.80 % of distances bigger than the voxel thickness (2mm). The large std value in PF+OF is due to a maximum value of 32.25%, found on Reg10-60; it is important to note that this maximum value also is presented in all the other algorithms. Figure 5.7 corroborates that PF+OF is the best performer (in terms of both mean and median values) for %DBVD, despite the outlier value of Reg10-60 that is visible on the box plot.

Finally, for the POPI model analysis, TRE values are presented in table 5.5. Analyzing this index, all four NRR approaches improve the Pre and PF values going from values above 3 mm to values below 2 mm; however only Demons based methods show results around an error of 1 mm. In this case PF+OF was 0.7mm higher than DDem, which has the best value (0.95±0.25 mm). In figure 5.8 it is possible to appreciate that DDem and Dem were the best performers, while OF and PF+OF presented values below 2 mm. Demons based algorithms were significantly different with respect to PF, and DDem was also statistically different in comparison with OF and PF+OF.

Table 5.1. POPI model registration accuracy. Comparison between six different conditions: before registration (1-Pre), Particle Filter (2-PF), Demons (3-Dem), Diffeomorphic Demons (4-DDem), Optical Flow (5-OF) and PF followed by OF (6-PF+OF) in terms of the Average Symmetric Distance (ASD). For each condition, nine ASD values corresponding to the registration performed between phase 10 and the nine remaining phases (00, 20, 30, ..., 90), alongside with the corresponding mean, standard deviation (std) and median values are presented. Presence of significant differences was assessed by a Kruskall-Wallis test (p<0.05). Differences between conditions are carried out by Wilcoxon rank-sum test; p-values for each comparison are presented at the end of the table, by matching columns and rows of each studied condition.

	ASD					
	1 Pre	***2 PF***	***3 Dem***	***4 DDem***	***5 OF***	***6 PF+OF***
R10-00	1.22	1.08	0.83	0.84	0.84	0.76
R10-20	1.19	1.18	0.80	0.83	0.85	0.77
R10-30	1.73	1.35	0.90	0.93	0.89	0.81
R10-40	2.41	1.97	1.06	1.07	1.06	0.95
R10-50	2.81	2.45	1.25	1.21	1.21	1.06
R10-60	2.80	2.63	1.18	1.17	1.13	1.06
R10-70	2.45	1.99	1.03	1.05	0.93	0.83
R10-80	2.00	1.60	0.92	0.95	0.84	0.81
R10-90	1.49	1.22	0.84	0.87	0.80	0.80
mean	***2.01***	***1.72***	***0.98***	***0.99***	***0.95***	***0.87***
std	***0.64***	***0.57***	***0.16***	***0.14***	***0.14***	***0.12***
median	***2.00***	***1.60***	***0.92***	***0.95***	***0.89***	***0.81***
Kruskall-Wallis	1.30E-06					
Wilcoxon	3,4,5,6	3,4,5,6	1,2	1,2,6	1,2	1,2,4
p-values						
1-Pre	x					
2-PF	0.29	x				
3-Dem	1.65E-04	0.00	x			
4-DDem	8.23E-05	2.88E-04	0.72	x		
5-OF	8.23E-05	2.88E-04	0.85	0.53	x	
6-PF+OF	4.11E-05	4.11E-05	0.11	0.04	0.12	x

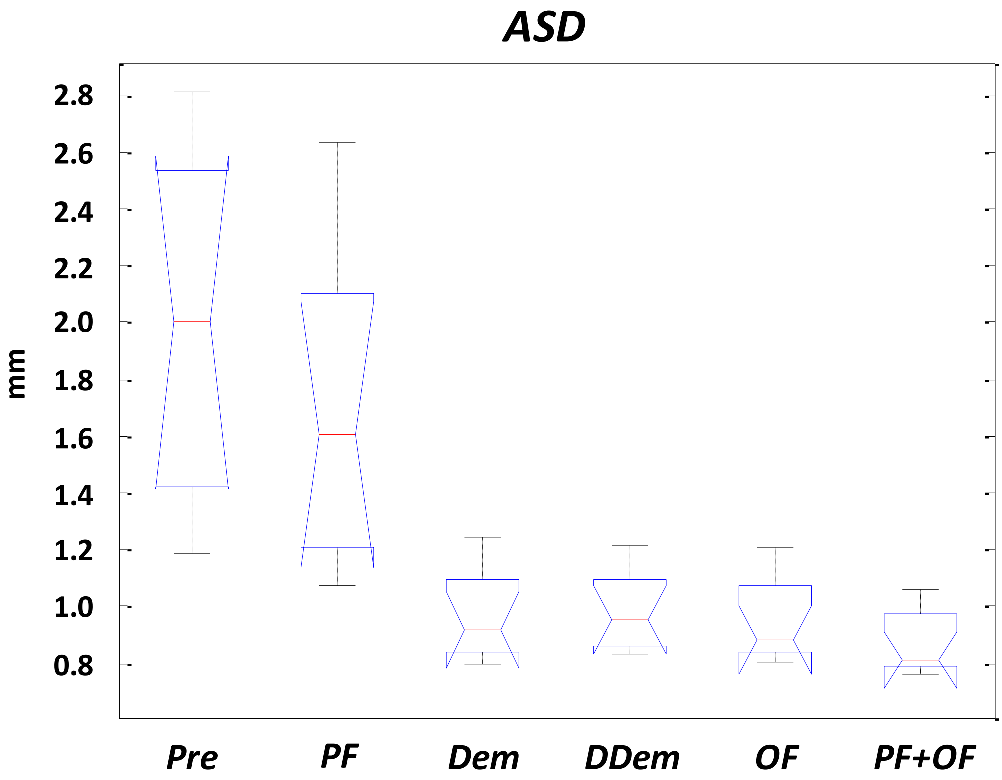

Figure 5.4. Box plot of the Average Symmetric Distance (ASD) index estimated for each of the six conditions studied using the POPI model dataset: before registration (Pre), Particle Filter (PF), Demons (Dem), Diffeomorphic Demons (DDem), Optical Flow (OF) and PF followed by OF (PF+OF). For each condition the box plot presents the median value (red line) bounded by the maximum and minimum values.

Table 5.2. POPI model registration accuracy. Comparison between six different conditions: before registration (1-Pre), Particle Filter (2-PF), Demons (3-Dem), Diffeomorphic Demons (4-DDem), Optical Flow (5-OF) and PF followed by OF (6-PF+OF) in terms of the Dice similarity coefficient (DICE). For each condition, nine DICE values corresponding to the registration performed between phase 10 and the nine remaining phases (00, 20, 30, ..., 90), alongside with the corresponding mean, standard deviation (std) and median values are presented. Presence of significant differences was assessed by a Kruskall-Wallis test (p<0.05). Differences between conditions are carried out by Wilcoxon rank-sum test; p-values for each comparison are presented at the end of the table, by matching columns and rows of each studied condition.

DICE

	1	***2***	***3***	***4***	***5***	***6***
	Pre	***PF***	***Dem***	***DDem***	***OF***	***PF+OF***
R10-00	0.96	0.95	0.97	0.97	0.96	0.94
R10-20	0.96	0.96	0.97	0.97	0.97	0.97
R10-30	0.95	0.96	0.96	0.96	0.97	0.97
R10-40	0.94	0.93	0.95	0.95	0.96	0.95
R10-50	0.93	0.94	0.95	0.95	0.96	0.97
R10-60	0.93	0.91	0.95	0.95	0.96	0.94
R10-70	0.94	0.94	0.95	0.95	0.96	0.96
R10-80	0.94	0.95	0.96	0.96	0.97	0.97
R10-90	0.95	0.96	0.97	0.97	0.97	0.97
mean	***0.94***	***0.94***	***0.96***	***0.96***	***0.96***	***0.96***
std	***0.01***	***0.02***	***0.01***	***0.01***	***0.00***	***0.01***
median	***0.94***	***0.95***	***0.96***	***0.96***	***0.96***	***0.97***
Kruskall-Wallis	0.01					
Wilcoxon	3,4,5,6	5,6	1	1	1,2	1,2
p-values						
1-Pre	x					
2-PF	0.82	x				
3-Dem	0.02	0.06	x			
4-DDem	0.02	0.06	1.00	x		
5-OF	8.64E-04	2.30E-03	0.23	0.23	x	
6-PF+OF	0.03	0.04	0.71	0.71	0.77	x

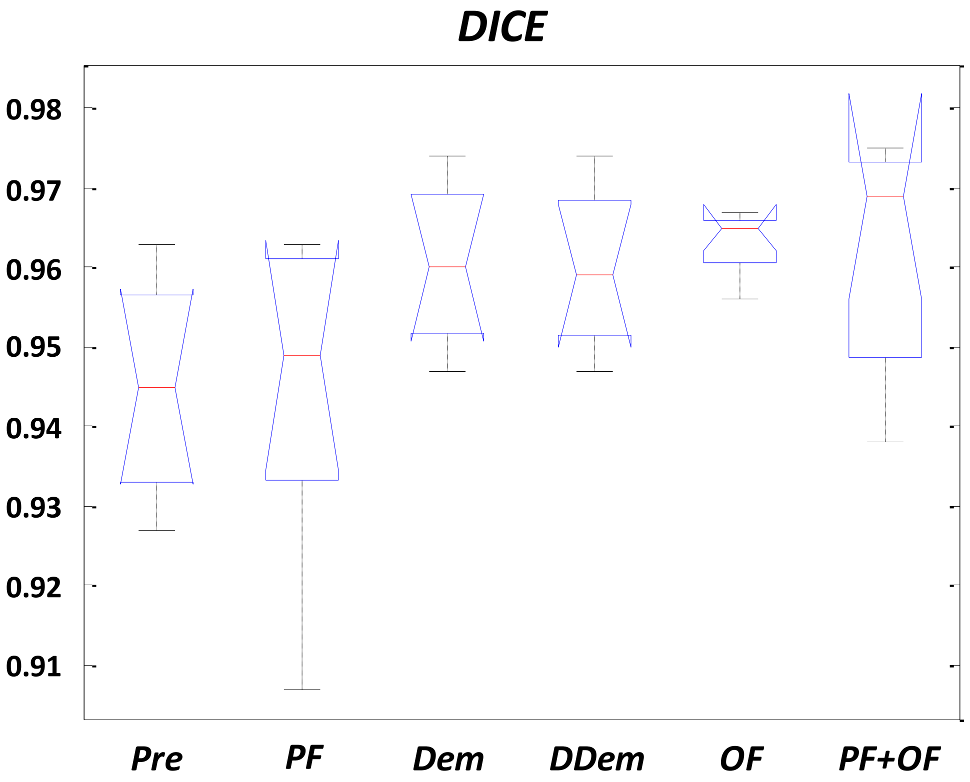

Figure 5.5. Box plot of the Dice similarity coefficient (DICE) index estimated for each of the six conditions studied using the POPI model dataset: before registration (Pre), Particle Filter (PF), Demons (Dem), Diffeomorphic Demons (DDem), Optical Flow (OF) and PF followed by OF (PF+OF). For each condition the box plot presents the median value (red line) bounded by the maximum and minimum values.

Table 5.3. POPI model registration accuracy. Comparison between six different conditions: before registration (1-Pre), Particle Filter (2-PF), Demons (3-Dem), Diffeomorphic Demons (4-DDem), Optical Flow (5-OF) and PF followed by OF (6-PF+OF) in terms of the Maximum distance (DMax). For each condition, nine DMax values corresponding to the registration performed between phase 10 and the nine remaining phases (00, 20, 30, ..., 90), alongside with the corresponding mean, standard deviation (std) and median values are presented. Presence of significant differences was assessed by a Kruskall-Wallis test (p<0.05). Differences between conditions are carried out by Wilcoxon rank-sum test; p-values for each comparison are presented at the end of the table, by matching columns and rows of each studied condition.

	DMax					
	1 Pre	***2 PF***	***3 Dem***	***4 DDem***	***5 OF***	***6 PF+OF***
R10-00	31.81	31.88	31.04	31.27	33.59	30.32
R10-20	34.97	33.63	31.14	33.04	33.17	32.52
R10-30	32.81	30.16	30.66	30.88	32.15	30.32
R10-40	38.09	33.33	33.84	33.20	33.33	33.33
R10-50	37.92	36.57	37.70	31.20	35.40	35.22
R10-60	38.14	38.10	33.84	29.89	38.09	37.92
R10-70	38.29	38.14	34.64	34.40	37.11	36.97
R10-80	35.06	32.46	30.66	30.66	31.89	30.84
R10-90	33.20	33.20	30.41	30.41	30.88	30.66
mean	***35.59***	***34.16***	***32.66***	***31.66***	***33.96***	***33.12***
std	***2.59***	***2.81***	***2.50***	***1.52***	***2.43***	***2.95***
median	***35.06***	***33.33***	***31.14***	***31.20***	***33.33***	***32.52***
Kruskall-Wallis	0.04					
Wilcoxon	3,4	4	1	1,2,5	4	-
p-values						
1-Pre	x					
2-PF	0.37	x				
3-Dem	0.02	0.37	x			
4-DDem	2.06E-03	0.04	0.50	x		
5-OF	0.23	0.81	0.29	0.03	x	
6-PF+OF	0.07	0.45	0.98	0.50	0.31	x

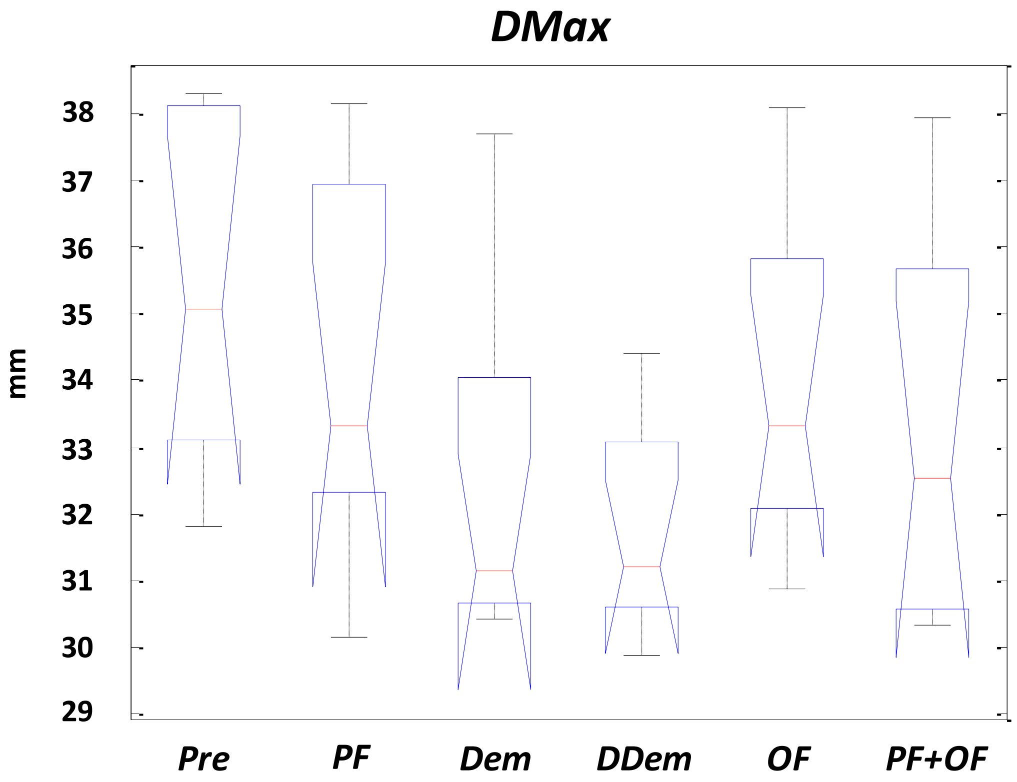

Figure 5.6. Box plot of the Maximum distance (DMax) index estimated for each of the six conditions studied using the POPI model dataset: before registration (Pre), Particle Filter (PF), Demons (Dem), Diffeomorphic Demons (DDem), Optical Flow (OF) and PF followed by OF (PF+OF). For each condition the box plot presents the median value (red line) bounded by the maximum and minimum values.

Table 5.4. POPI model registration accuracy. Comparison between six different conditions: before registration (1-Pre), Particle Filter (2-PF), Demons (3-Dem), Diffeomorphic Demons (4-DDem), Optical Flow (5-OF) and PF followed by OF (6-PF+OF) in terms of the Percentage of Distances bigger than the Voxel Dimension (%DBVD). For each condition, nine %DBVD values corresponding to the registration performed between phase 10 and the nine remaining phases (00, 20, 30, ..., 90), alongside with the corresponding mean, standard deviation (std) and median values are presented. Presence of significant differences was assessed by a Kruskall-Wallis test (p<0.05). Differences between conditions are carried out by Wilcoxon rank-sum test; p-values for each comparison are presented at the end of the table, by matching columns and rows of each studied condition.

	%DBVD					
	1	***2***	***3***	***4***	***5***	***6***
	Pre	***PF***	***Dem***	***DDem***	***OF***	***PF+OF***
R10-00	27.08	7.95	3.05	3.37	4.74	2.80
R10-20	24.15	24.58	4.19	5.73	7.18	5.47
R10-30	36.50	24.03	8.21	5.11	10.74	3.50
R10-40	45.50	30.96	30.88	23.18	18.10	16.23
R10-50	51.30	25.31	41.76	30.25	22.98	5.13
R10-60	54.09	44.91	44.01	34.81	21.83	32.25
R10-70	51.65	32.70	38.41	31.50	17.57	8.18
R10-80	40.11	17.91	26.82	19.01	11.74	2.41
R10-90	32.59	17.79	2.99	5.05	6.32	2.95
mean	***40.33***	***25.13***	***22.26***	***17.56***	***13.47***	***8.77***
std	***11.05***	***10.52***	***17.58***	***12.94***	***6.85***	***9.80***
median	***40.11***	***24.58***	***26.82***	***19.01***	***11.74***	***5.13***
Kruskall-Wallis	3.96E-04					
Wilcoxon	2,3,4,5,6	1,5,6	1	1	1,2	1,2
p-values						
1-Pre	x					
2-PF	0.01	x				
3-Dem	0.04	0.80	x			
4-DDem	1.85E-03	0.26	0.73	x		
5-OF	4.11E-05	0.01	0.55	0.67	x	
6-PF+OF	1.65E-04	3.99E-03	0.09	0.14	0.06	x

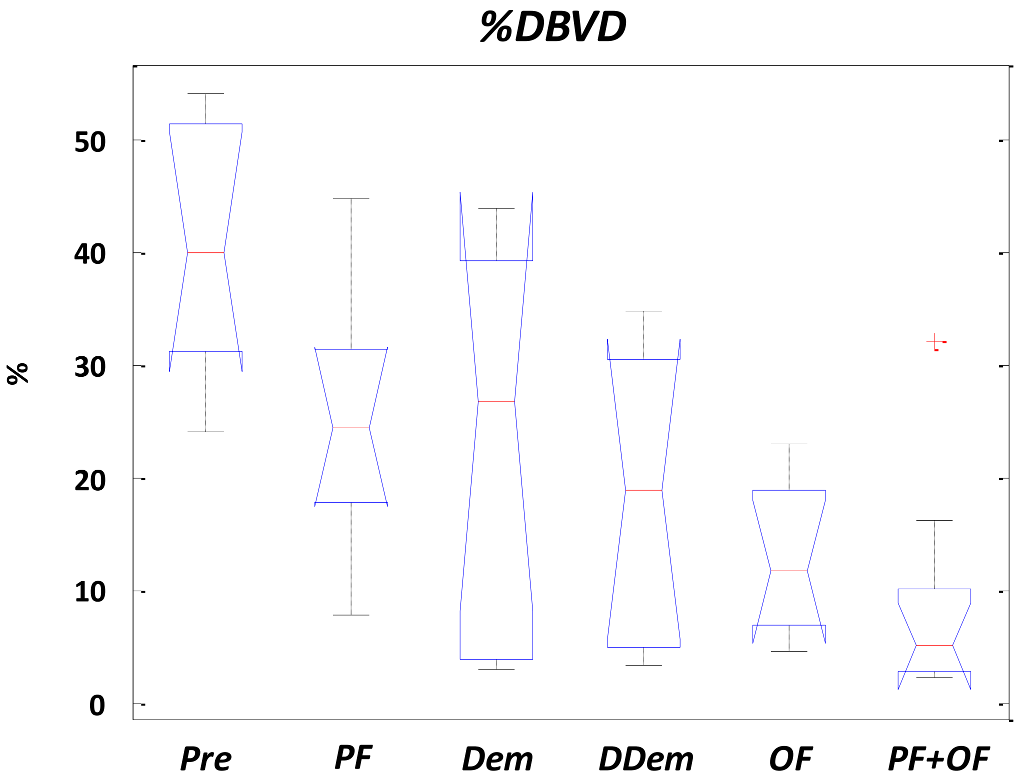

Figure 5.7. Box plot of the Percentage of Distances Bigger than the Voxel Dimension (%DBVD) index estimated for each of the six conditions studied using the POPI model dataset: before registration (Pre), Particle Filter (PF), Demons (Dem), Diffeomorphic Demons (DDem), Optical Flow (OF) and PF followed by OF (PF+OF). For each condition the box plot presents the median value (red line) bounded by the maximum and minimum values.

Table 5.5. POPI model registration accuracy. Comparison between six different conditions: before registration (1-Pre), Particle Filter (2-PF), Demons (3-Dem), Diffeomorphic Demons (4-DDem), Optical Flow (5-OF) and PF followed by OF (6-PF+OF) in terms of the Target Registration Error (TRE). For each condition, nine TRE values corresponding to the registration performed between phase 10 and the nine remaining phases (00, 20, 30, ..., 90), alongside with the corresponding mean, standard deviation (std) and median values are presented. Presence of significant differences was assessed by a Kruskall-Wallis test (p<0.05). Differences between conditions are carried out by Wilcoxon rank-sum test; p-values for each comparison are presented at the end of the table, by matching columns and rows of each studied condition.

	TRE					
	1 Pre	***2 PF***	***3 Dem***	***4 DDem***	***5 OF***	***6 PF+OF***
R10-00	0.50	0.52	0.67	0.62	0.53	0.55
R10-20	0.44	0.52	0.59	0.51	0.48	0.59
R10-30	2.24	2.16	1.33	1.23	2.09	1.47
R10-40	4.27	4.09	1.22	1.09	2.00	1.99
R10-50	5.35	5.32	1.29	1.17	2.36	2.26
R10-60	5.55	5.57	1.08	1.02	2.45	2.41
R10-70	4.46	4.27	1.27	1.15	2.08	2.06
R10-80	3.40	3.19	1.00	0.90	1.88	1.86
R10-90	1.94	1.82	0.88	0.82	1.82	1.70
mean	***3.13***	***3.05***	***1.03***	***0.95***	***1.74***	***1.65***
std	***1.95***	***1.91***	***0.27***	***0.25***	***0.73***	***0.68***
median	***3.40***	***3.19***	***1.08***	***1.02***	***2.00***	***1.86***
Kruskall-Wallis	1.82E-02					
Wilcoxon	-	3,4	2	2,5,6	4	3,4
p-values						
1-Pre	x					
2-PF	0.95	x				
3-Dem	0.05	0.05	x			
4-DDem	0.05	0.03	0.44	x		
5-OF	0.16	0.17	0.05	0.04	x	
6-PF+OF	0.16	0.18	0.04	0.03	0.67	x

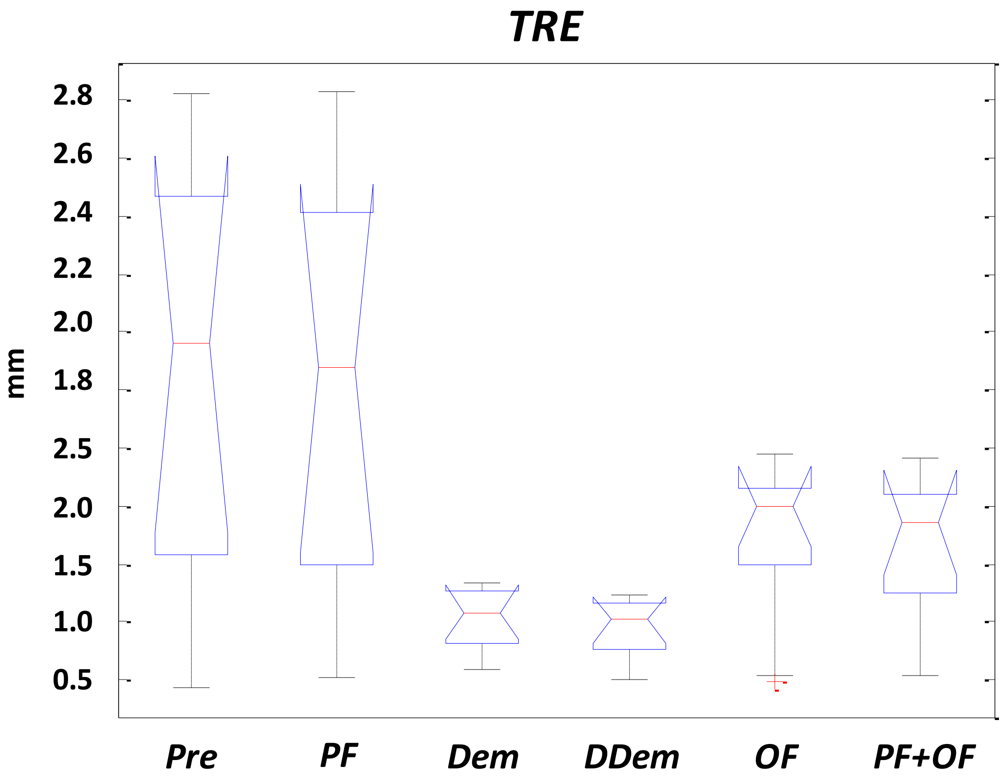

Figure 5.8. Box plot of the Target Registration Error (TRE) index estimated for each of the six conditions studied using the POPI model dataset: before registration (Pre), Particle Filter (PF), Demons (Dem), Diffeomorphic Demons (DDem), Optical Flow (OF) and PF followed by OF (PF+OF). For each condition the box plot presents the median value (red line) bounded by the maximum and minimum values.

5.2 Registration Accuracy on the Clinical Dataset

Figure 5.9 presents an example of the registration results obtained using a 4D CT image from one patient of the clinical images dataset. In figures, from fig.5.9 (a) to (f), it is possible to observe the right lung and the GTV of the inspiratory phase (target image) alongside the contours of both structures of interest obtained from the expiratory phase (source image) in six conditions: before registration Pre - (a), and after the registration achieved by five different algorithms: PF - (b), Dem - (c), DDem - (d), OF - (e) and OF+PF - (f). In this figure, it is possible to visually assess the performance of each registration algorithm taking into account how well each contour is realigned with its correspondent zone in comparison with the overlapped contours presented in figure 5.9 (a), where the misalignment in both structures of interest due to the respiratory motion is clear (structures in the inspiratory phase versus the expiratory phase). Considering the lung, all four NRR algorithms show good performance, being able to recover the misalignments presented at the top and inner sections of the lung. Analyzing GTV contours, it is possible to observe no improvement achieved by PF being nearly identical to Pre, and misalignment recovery achieved by the four NRR approaches. In addition, it is possible to observe that the improvement among elastic registration methods is different, Dem and DDem are very similar qualitatively having an acceptable performance but still having some issues on the border of the tumor; similarly OF has an acceptable performance but is possible to identify some misalignments; and a clear improvement between OF and PF+OF, being the last one the best performer qualitatively for this particular example.

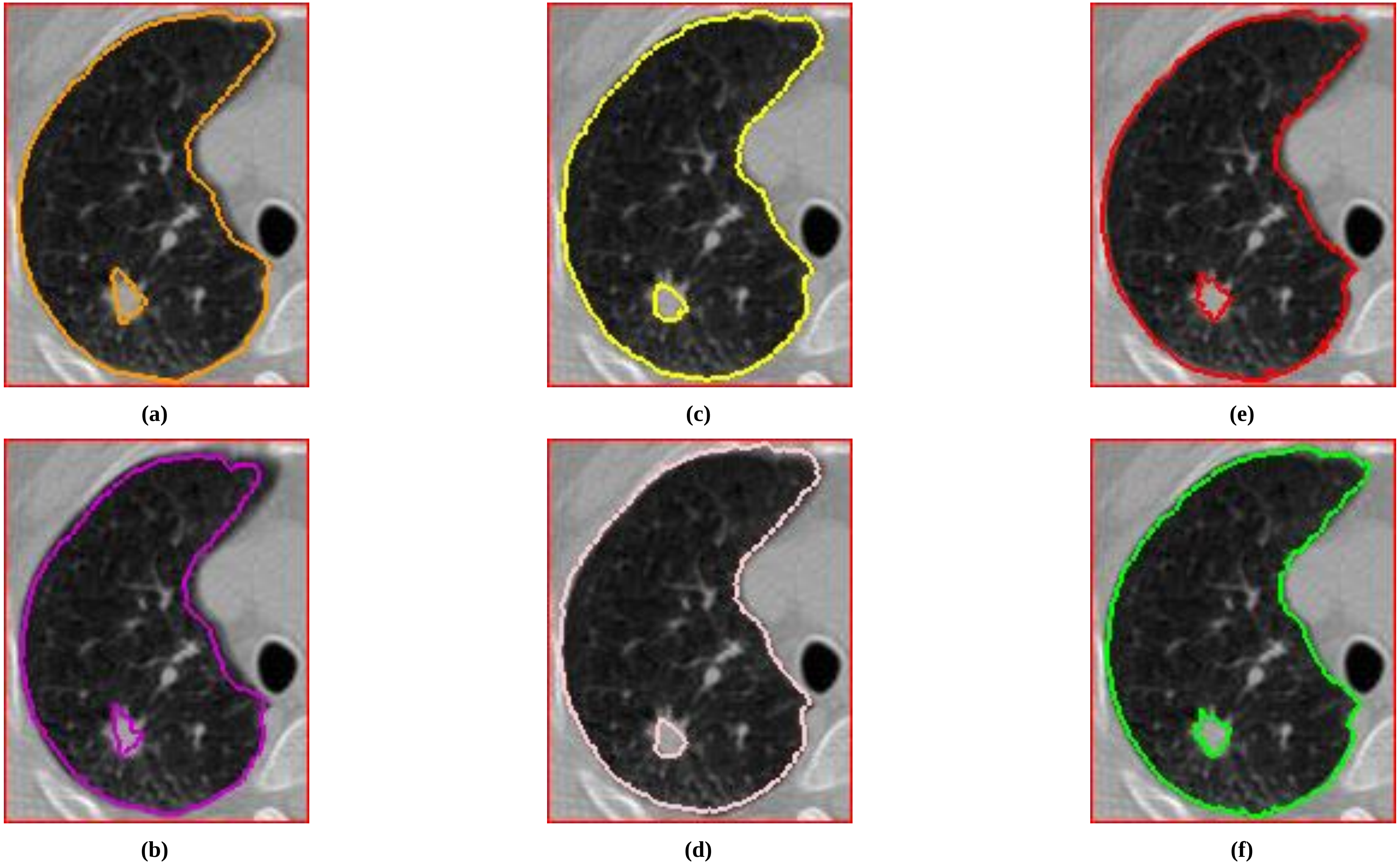

Figure 5.9. Example of the results achieved by all the registration methods using a lung 4DCT image. In each sub-image the target image (inspiratory phase) is presented with the superimposed lung and GTV contours obtained from the source image (expiratory phase) from the six studied conditions: (a) Before registration (Pre) - orange, (b) Particle Filter (PF)- purple, (c) Demons (Dem) - yellow, (d) Diffeomorphic Demons (DDem) - pale pink, (e) Optical Flow (OF)- red, (f) PF followed by OF (PF+OF) - green.

Tables 5.6 to 5.13 summarize the overall registration accuracy results for the clinical images dataset from a quantitative point of view. For each index, results were divided into lungs and GTV for each of the six conditions analyzed in this work: before registration (1-Pre), and after each registration algorithm studied: Particle Filter (2-PF), Demons (3-Dem), Diffeomorphic Demons (4-DDem), Optical Flow (5-OF) and PF followed by OF (6-PF+OF). As in the POPI model results, figures 5.10 to 5.17 present a visual representation of the performance as a box plot for each registration algorithm on every index.

In tables 5.6 and 5.7 the results for the ASD in the lungs and GTV are presented respectively. Considering the lungs, a remarkable improvement was found by all NRR methods, being Dem, DDem and PF+OF the methods with ASD values below 2 mm; in this case PF+OF was 3.5 % bigger than the best value achieved by Dem (1.68±0.50 mm); Significant differences were found between PF+OF, Dem and DDem with respect to Pre and PF but not among them. Considering the GTV structures, the behavior in all registration algorithms was similar, again being PF+OF, Dem and DDem the best performers with ASD values around 1.4 mm; in this particular case, PF+OF presented the best value (1.43±0.10 mm). Despite the similar behavior between lung and GTV values, no significant differences were found considering GTV structures. In figures 5.10 and 5.11 it is possible to observe that PF+OF, Dem and DDem have values below 2 mm in both groups of anatomical structures.

DMax results are shown in tables 5.8 and 5.9. In this case the best values were achieved by Dem, DDem and PF+OF methods, being capable to decrease the Pre in at least 14 mm; the best DMax value, in terms of the mean, was obtained by Dem in both datasets (55.78±18.46 mm for the lungs, and 11.17±3.48 mm for GTV) being 9% and 10% lower than PF+OF for lungs and GTV structures respectively. Figures 5.12 and 5.13 exhibit that all NRR algorithms have a similar median value around 60 mm considering the lungs; while analyzing GTV, Dem is slightly improved with respect to PF+OF. However, in both group of structures, no significant differences were found.

Tables 5.10 and 5.11 present the DICE index results. In this case, PF+OF alongside with the demons based algorithms showed a notable improvement in both datasets (from a Pre DICE mean value of 0.87 to 0.94 for the lungs, and from 0.52 to 0.72 for GTV), being PF+OF the algorithm with the best index values in both, the lungs (0.94±0.03), and GTV (0.72±0.06). Figures 5.14 and 5.15 shown, in both cases, that PF+OF, Dem and DDem have similar behaviors, all of them with improving considerable with respect to Pre. For this index, despite the similar trends found in both datasets, no significant differences were found for the lungs; while considering GTV, Dem, DDem and PF+OF were significantly different with respect to Pre, and only PF+OF was also statistically different with respect to OF.

Finally, analyzing %DBVD in table 5.12 is possible to observe that OF and PF+OF are the algorithms with the largest improvement considering the lungs structures, reducing the original mean Pre value (46.65±29.03 %) to values below 30 %, being PF+OF the best performer with a value of 27.16±11.79 %; for the GTV case, results are presented in table 5.13, where is possible to observe that the best value belongs again to PF+OF (33.37±19.58%). In figure 5.16 is possible to observe that all registration methods improved, in terms of the median value, between 10% (PF) and 20% (PF+OF) with respect to Pre for the lungs; while figure 5.17 shows the behavior for GTV with PF+OF and Dem having the best performances. For this index again, despite improvements achieved, no significant differences were found in both datasets.

Table 5.6. Clinical dataset- Lungs registration accuracy. Comparison between six different conditions: before registration (1-Pre), Particle Filter (2-PF), Demons (3-Dem), Diffeomorphic Demons (4-DDem), Optical Flow (5-OF) and PF followed by OF (6-PF+OF) in terms of the Average Symmetric Distance (ASD). For each condition, ASD values corresponding to the registration performed between inspiratory and expiratory phases of the Right (Rx) and Left (Lx) lungs for each of the five patients, alongside with the corresponding mean, standard deviation (std) and median values are presented. Presence of significant differences was assessed by a Kruskall-Wallis test ($p<0.05$). Differences between conditions are carried out by Wilcoxon rank-sum test; p-values for each comparison are presented at the end of the table, by matching columns and rows of each studied condition.

ASD - Lungs

		1 Pre	***2 PF***	***3 Dem***	***4 DDem***	***5 OF***	***6 PF+OF***
P1	***Rx***	3.12	2.26	1.84	1.84	2.07	1.76
	Lx	2.68	2.37	1.55	1.66	1.89	1.71
P2	***Rx***	6.50	4.94	1.47	1.55	4.06	1.92
	Lx	7.06	4.94	1.35	1.43	3.97	1.90
P3	***Rx***	6.24	5.47	2.83	2.88	4.41	2.55
P4	***Rx***	2.23	2.33	1.22	1.25	1.07	1.09
P5	***Rx***	2.47	2.65	1.63	1.68	1.59	1.64
	Lx	1.90	2.52	1.51	1.55	2.07	1.33
	mean	***4.03***	***3.43***	***1.68***	***1.73***	***2.64***	***1.74***
	std	***2.17***	***1.41***	***0.50***	***0.50***	***1.29***	***0.43***
	median	***2.90***	***2.58***	***1.53***	***1.61***	***2.07***	***1.73***
	Kruskall-Wallis	3.86E-04					
	Wilcoxon	3,4,6	3,4,6	1,2	1,2	-	1,2
	p-values						
	1-Pre	x					
	2-PF	0.63	x				
	3-Dem	1.86E-03	2.95E-03	x			
	4-DDem	1.86E-03	2.95E-03	0.46	x		
	5-OF	1.30E-01	0.08	0.06	0.08	x	
	6-PF+OF	2.18E-03	1.86E-03	0.44	0.57	0.19	x

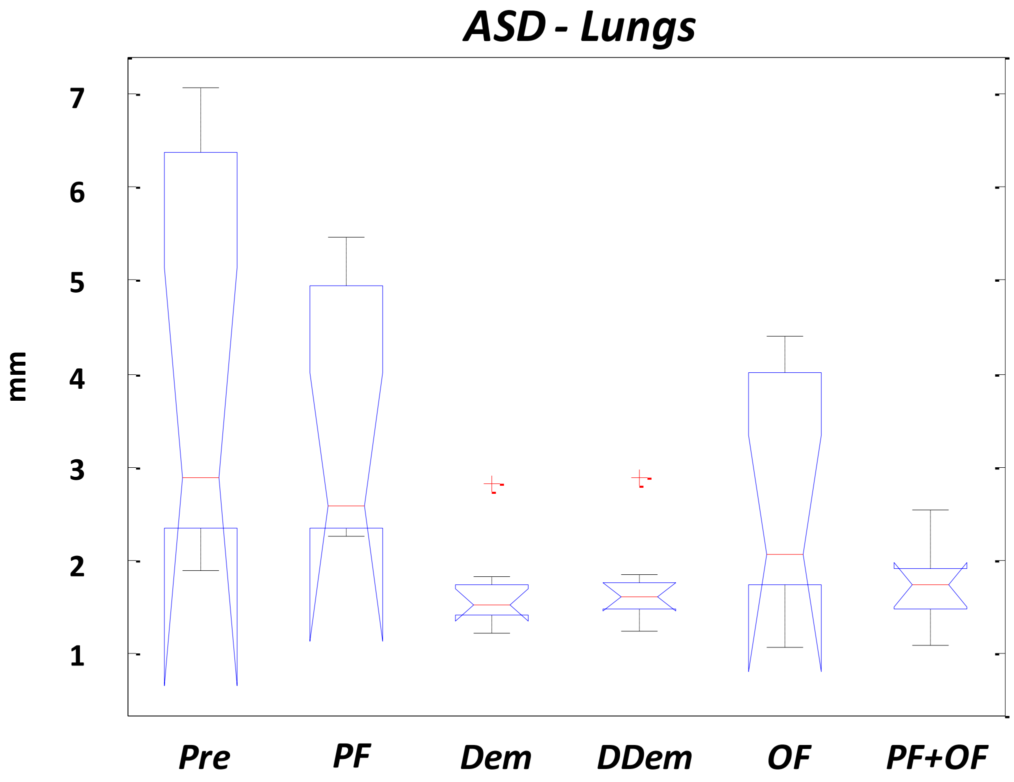

Figure 5.10. Box plot of the Average Symmetric Distance (ASD) index estimated for each of the six conditions studied in the clinical images dataset: before registration (Pre), Particle Filter (PF), Demons (Dem), Diffeomorphic Demons (DDem), Optical Flow (OF) and PF followed by OF (PF+OF). ASD values were calculated from the lung segmentations of the 5 patients studied in the clinical images dataset. For each condition the box plot presents the median value (red line) bounded by the maximum and minimum values.

Table 5.7. Clinical dataset- Gross Target Volume (GTV) registration accuracy. Comparison between six different conditions: before registration (1-Pre), Particle Filter (2-PF), Demons (3-Dem), Diffeomorphic Demons (4-DDem), Optical Flow (5-OF) and PF followed by OF (6-PF+OF) in terms of the Average Symmetric Distance (ASD). For each condition, ASD values corresponding to the registration performed between inspiratory and expiratory phases of the GTV for each of the five patients, alongside with the corresponding mean, standard deviation (std) and median values are presented. Presence of significant differences was assessed by a Kruskall-Wallis test ($p<0.05$).

ASD - GTV

		1 ***Pre***	***2*** ***PF***	***3*** ***Dem***	***4*** ***DDem***	***5*** ***OF***	***6*** ***PF+OF***
P1	***GTV***	1.87	1.65	1.47	1.44	1.66	1.50
P2	***GTV***	4.11	2.73	1.24	1.29	4.19	1.46
P3	***GTV***	5.20	5.55	1.55	1.62	2.88	1.39
P4	***GTV***	2.78	2.72	1.25	1.29	1.56	1.55
P5	***GTV***	1.42	0.89	1.76	1.69	1.35	1.28
	mean	***3.08***	***2.71***	***1.45***	***1.46***	***2.33***	***1.43***
	std	***1.57***	***1.77***	***0.22***	***0.19***	***1.20***	***0.10***
	median	***2.78***	***2.72***	***1.47***	***1.44***	***1.66***	***1.46***
	Kruskall-Wallis	0.10					

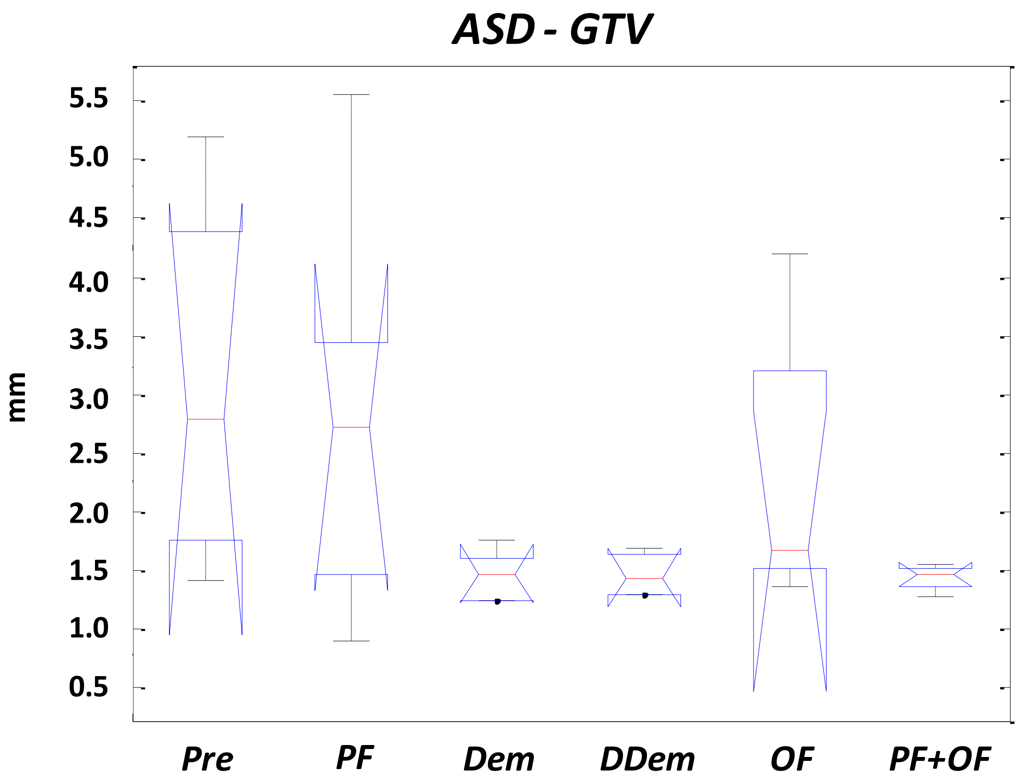

Figure 5.11. Box plot of the Average Symmetric Distance (ASD) index estimated for each of the six conditions studied in the clinical images dataset: before registration (Pre), Particle Filter (PF), Demons (Dem), Diffeomorphic Demons (DDem), Optical Flow (OF) and PF followed by OF (PF+OF). ASD values were calculated from the Gross Target Volume (GTV) segmentations of the 5 patients studied in the clinical images dataset. For each condition the box plot presents the median value (red line) bounded by the maximum and minimum values.

Table 5.8. Clinical dataset- Lungs registration accuracy. Comparison between six different conditions: before registration (1-Pre), Particle Filter (2-PF), Demons (3-Dem), Diffeomorphic Demons (4-DDem), Optical Flow (5-OF) and PF followed by OF (6-PF+OF) in terms of the Maximum distance (DMax). For each condition, DMax values corresponding to the registration performed between inspiratory and expiratory phases of the Right (Rx) and Left (Lx) lungs for each of the five patients, alongside with the corresponding mean, standard deviation (std) and median values are presented. Presence of significant differences was assessed by a Kruskall-Wallis test (p<0.05).

		DMax - Lungs					
		1	***2***	***3***	***4***	***5***	***6***
		Pre	***PF***	***Dem***	***DDem***	***OF***	***PF+OF***
P1	***Rx***	46.27	45.60	44.19	44.19	61.12	51.12
	Lx	49.04	49.07	51.16	53.43	55.24	53.53
P2	***Rx***	101.06	82.37	51.54	51.56	66.81	58.09
	Lx	167.34	158.96	66.82	66.87	143.32	86.96
P3	***Rx***	70.80	71.09	64.52	66.10	72.27	72.27
P4	***Rx***	39.86	39.37	39.28	39.28	37.70	38.48
P5	***Rx***	102.84	101.56	92.60	101.30	94.85	92.60
	Lx	45.91	45.94	36.13	43.95	53.46	52.59
	mean	***77.89***	***74.25***	***55.78***	***58.33***	***73.10***	***63.21***
	std	***43.93***	***40.48***	***18.46***	***20.07***	***32.83***	***18.90***
	median	***59.92***	***60.08***	***51.35***	***52.49***	***63.96***	***55.81***
	Kruskall-Wallis	0.71					

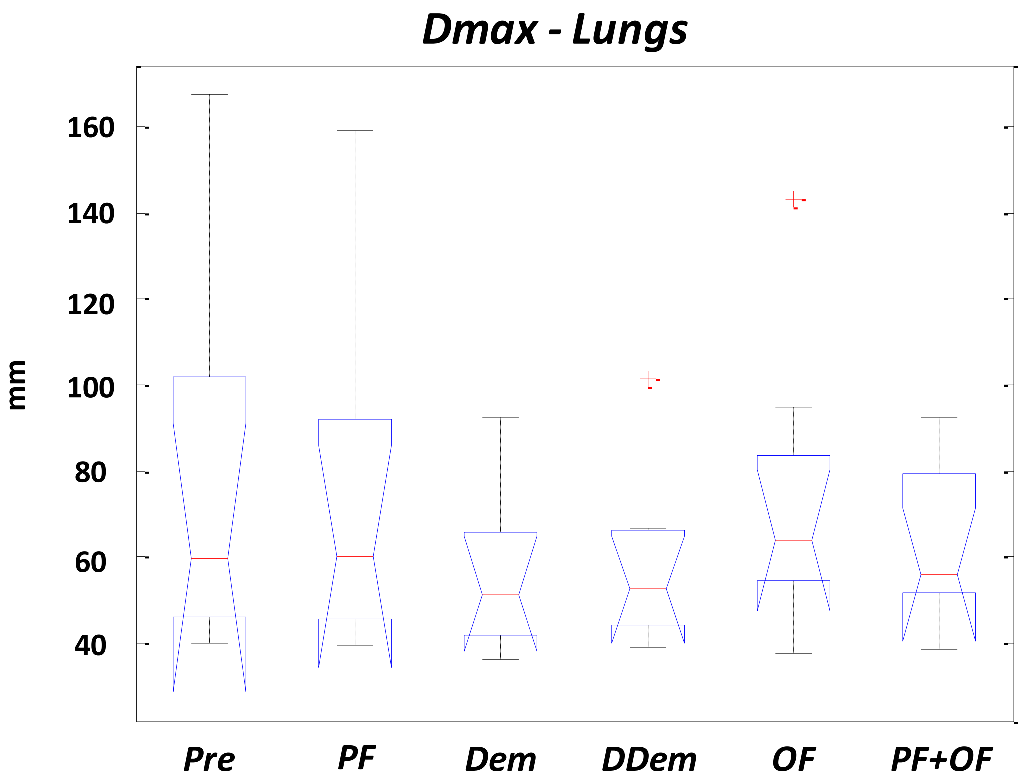

Figure 5.12. Box plot of the Maximum distance (DMax) index estimated for each of the six conditions studied in the clinical images dataset: before registration (Pre), Particle Filter (PF), Demons (Dem), Diffeomorphic Demons (DDem), Optical Flow (OF) and PF followed by OF (PF+OF). DMax values were calculated from the lung segmentations of the 5 patients studied in the clinical images dataset. For each condition the box plot presents the median value (red line) bounded by the maximum and minimum values.

Table 5.9. Clinical dataset- Gross Target Volume (GTV) registration accuracy. Comparison between six different conditions: before registration (1-Pre), Particle Filter (2-PF), Demons (3-Dem), Diffeomorphic Demons (4-DDem), Optical Flow (5-OF) and PF followed by OF (6-PF+OF) in terms of the Maximum distance (DMax). For each condition, DMax values corresponding to the registration performed between inspiratory and expiratory phases of the GTV for each of the five patients, alongside with the corresponding mean, standard deviation (std) and median values are presented. Presence of significant differences was assessed by a Kruskall-Wallis test (p<0.05).

DMax - GTV

		1 ***Pre***	***2*** ***PF***	***3*** ***Dem***	***4*** ***DDem***	***5*** ***OF***	***6*** ***PF+OF***
P1	***GTV***	8.29	7.04	6.25	6.25	9.21	9.21
P2	***GTV***	21.62	17.58	13.10	13.60	25.69	14.66
P3	***GTV***	18.66	22.14	14.52	17.95	15.44	15.75
P4	***GTV***	17.05	17.30	13.14	13.14	15.44	15.44
P5	***GTV***	6.18	7.04	8.84	8.05	9.00	5.26
	mean	***14.36***	***14.22***	***11.17***	***11.80***	***14.96***	***12.06***
	std	***6.75***	***6.83***	***3.48***	***4.68***	***6.78***	***4.64***
	median	***17.05***	***17.30***	***13.10***	***13.14***	***15.44***	***14.66***
	Kruskall-Wallis	0.77					

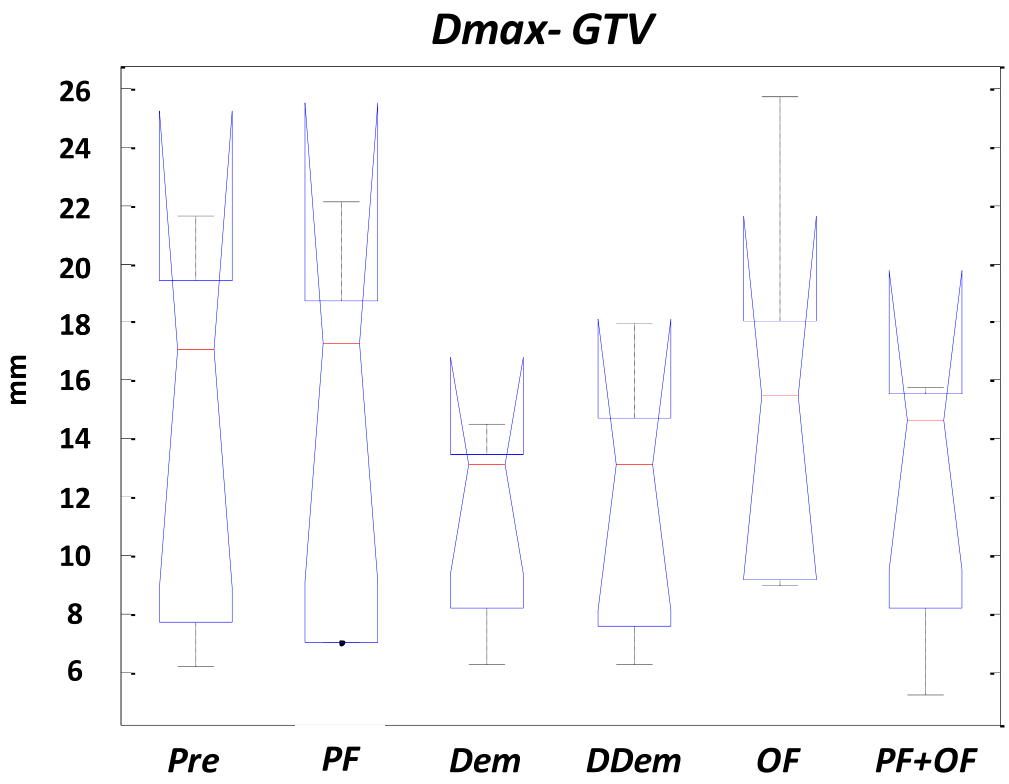

Figure 5.13. Box plot of the Maximum distance (DMax) index estimated for each of the six conditions studied in the clinical images dataset: before registration (Pre), Particle Filter (PF), Demons (Dem), Diffeomorphic Demons (DDem), Optical Flow (OF) and PF followed by OF (PF+OF). DMax values were calculated from the Gross Target Volume (GTV) segmentations of the 5 patients studied in the clinical images dataset. For each condition the box plot presents the median value (red line) bounded by the maximum and minimum values.

Table 5.10. Clinical dataset- Lungs registration accuracy. Comparison between six different conditions: before registration (1-Pre), Particle Filter (2-PF), Demons (3-Dem), Diffeomorphic Demons (4-DDem), Optical Flow (5-OF) and PF followed by OF (6-PF+OF) in terms of the Dice similarity coefficient (DICE). For each condition, DICE values corresponding to the registration performed between inspiratory and expiratory phases of the Right (Rx) and Left (Lx) lungs for each of the five patients, alongside with the corresponding mean, standard deviation (std) and median values are presented. Presence of significant differences was assessed by a Kruskall-Wallis test (p<0.05).

DICE - Lungs

		1	***2***	***3***	***4***	***5***	***6***
		Pre	***PF***	***Dem***	***DDem***	***OF***	***PF+OF***
P1	***Rx***	0.94	0.95	0.96	0.96	0.95	0.96
	Lx	0.96	0.95	0.96	0.96	0.96	0.96
P2	***Rx***	0.76	0.80	0.93	0.93	0.83	0.95
	Lx	0.75	0.79	0.93	0.93	0.81	0.94
P3	***Rx***	0.80	0.82	0.91	0.91	0.89	0.90
P4	***Rx***	0.93	0.92	0.95	0.94	0.96	0.96
P5	***Rx***	0.93	0.91	0.91	0.91	0.93	0.93
	Lx	0.93	0.91	0.92	0.92	0.93	0.92
	mean	***0.87***	***0.88***	***0.94***	***0.93***	***0.91***	***0.94***
	std	***0.09***	***0.07***	***0.02***	***0.02***	***0.06***	***0.03***
	median	***0.93***	***0.91***	***0.93***	***0.93***	***0.93***	***0.95***
	Kruskall-Wallis	0.20					

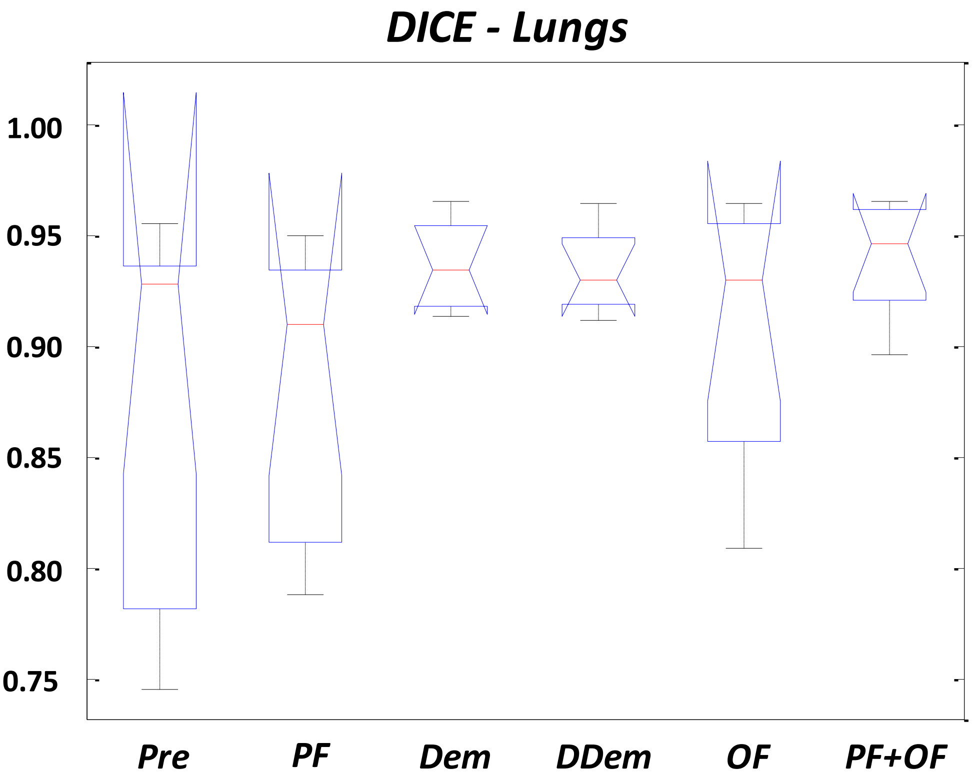

Figure 5.14. Box plot of the Dice similarity coefficient (DICE) index estimated for each of the six conditions studied in the clinical images dataset: before registration (Pre), Particle Filter (PF), Demons (Dem), Diffeomorphic Demons (DDem), Optical Flow (OF) and PF followed by OF (PF+OF). DICE values were calculated from the lung segmentations of the 5 patients studied in the clinical images dataset. For each condition the box plot presents the median value (red line) bounded by the maximum and minimum values.

Table 5.11. Clinical dataset- Gross Target Volume (GTV) registration accuracy. Comparison between six different conditions: before registration (1-Pre), Particle Filter (2-PF), Demons (3-Dem), Diffeomorphic Demons (4-DDem), Optical Flow (5-OF) and PF followed by OF (6-PF+OF) in terms of the Dice similarity coefficient (DICE). For each condition, DICE values corresponding to the registration performed between inspiratory and expiratory phases of the GTV for each of the five patients, alongside with the corresponding mean, standard deviation (std) and median values are presented. Presence of significant differences was assessed by a Kruskall-Wallis test (p<0.05). Differences between conditions are carried out by Wilcoxon rank-sum test; p-values for each comparison are presented at the end of the table, by matching columns and rows of each studied condition.

DICE - GTV

		1	***2***	***3***	***4***	***5***	***6***
		Pre	***PF***	***Dem***	***DDem***	***OF***	***PF+OF***
P1	***GTV***	0.64	0.74	0.76	0.76	0.71	0.73
P2	***GTV***	0.57	0.71	0.81	0.81	0.54	0.81
P3	***GTV***	0.42	0.39	0.78	0.78	0.63	0.74
P4	***GTV***	0.47	0.49	0.69	0.69	0.62	0.69
P5	***GTV***	0.52	0.51	0.53	0.54	0.64	0.63
	mean	***0.52***	***0.57***	***0.71***	***0.72***	***0.63***	***0.72***
	std	***0.09***	***0.15***	***0.11***	***0.11***	***0.06***	***0.06***
	median	***0.52***	***0.51***	***0.76***	***0.76***	***0.63***	***0.73***
	Kruskall-Wallis	0.04					
	Wilcoxon	3,4,6	-	1	1	6	1,5
	p-values						
	1-Pre	x					
	2-PF	0.84	x				
	3-Dem	0.03	0.10	x			
	4-DDem	0.03	0.10	1.00	x		
	5-OF	0.15	0.60	0.22	0.15	x	
	6-PF+OF	0.02	0.20	0.79	0.73	0.05	x

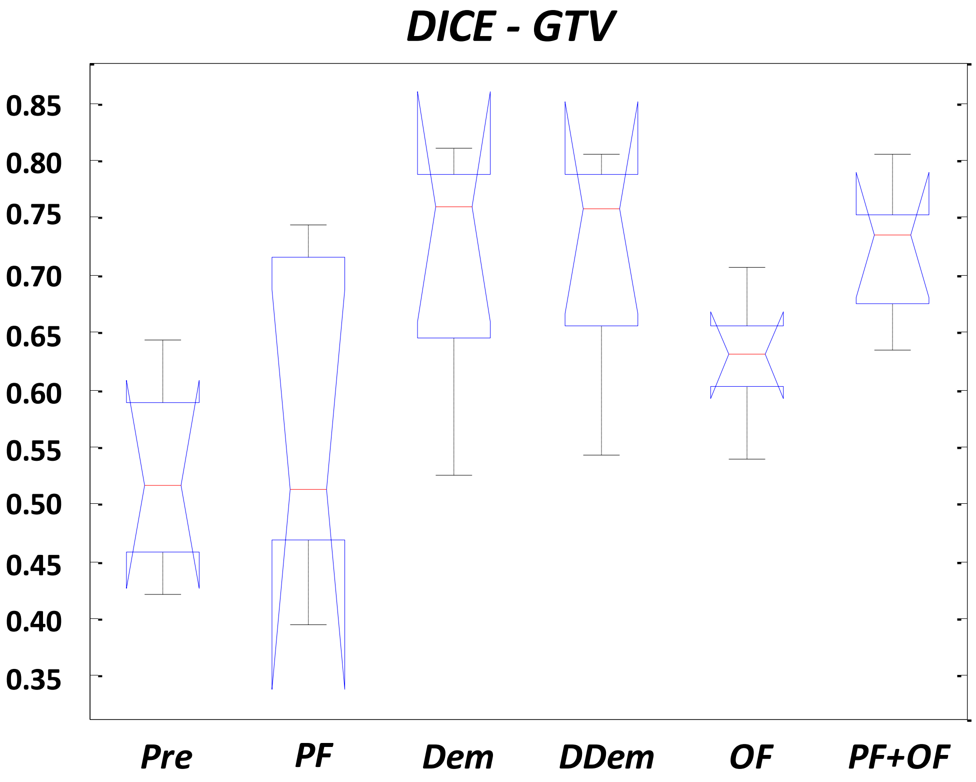

Figure 5.15. Box plot of the Dice similarity coefficient (DICE) index estimated for each of the six conditions studied in the clinical images dataset: before registration (Pre), Particle Filter (PF), Demons (Dem), Diffeomorphic Demons (DDem), Optical Flow (OF) and PF followed by OF (PF+OF). DICE values were calculated from the Gross Target Volume (GTV) segmentations of the 5 patients studied in the clinical images dataset. For each condition the box plot presents the median value (red line) bounded by the maximum and minimum values.

Table 5.12. Clinical dataset- Lungs registration accuracy. Comparison between six different conditions: before registration (1-Pre), Particle Filter (2-PF), Demons (3-Dem), Diffeomorphic Demons (4-DDem), Optical Flow (5-OF) and PF followed by OF (6-PF+OF) in terms of the Percentage of Distances bigger than the Voxel Dimension (%DBVD). For each condition, %DBVD values corresponding to the registration performed between inspiratory and expiratory phases of the Right (Rx) and Left (Lx) lungs for each of the five patients, alongside with the corresponding mean, standard deviation (std) and median values are presented. Presence of significant differences was assessed by a Kruskall-Wallis test (p<0.05).

		%DBVD - Lungs					
		1	***2***	***3***	***4***	***5***	***6***
		Pre	***PF***	***Dem***	***DDem***	***OF***	***PF+OF***
P1	***Rx***	79.71	25.97	40.96	39.94	28.62	31.80
	Lx	38.54	26.25	35.16	44.74	27.72	25.52
P2	***Rx***	56.85	39.66	59.47	59.89	35.40	29.14
	Lx	60.80	21.06	48.75	50.13	32.23	42.09
P3	***Rx***	61.49	45.31	64.43	63.88	36.09	33.92
P4	***Rx***	68.62	82.65	28.76	29.70	19.23	17.01
P5	***Rx***	0.11	3.08	18.63	17.98	19.35	4.12
	Lx	7.05	21.04	28.30	26.66	30.80	33.66
	mean	***46.65***	***33.13***	***40.56***	***41.61***	***28.68***	***27.16***
	std	***29.03***	***23.72***	***16.01***	***16.21***	***6.49***	***11.79***
	median	***58.82***	***26.11***	***38.06***	***42.34***	***29.71***	***30.47***
	Kruskall-Wallis	0.25					

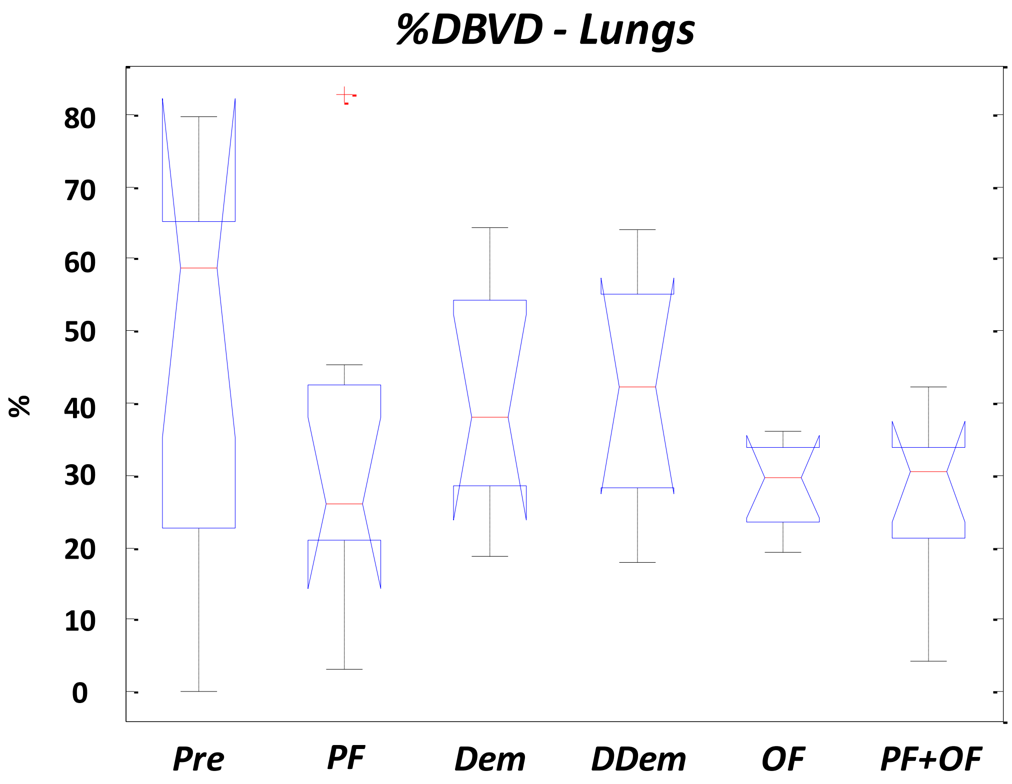

Figure 5.16. Box plot of the Percentage of Distances Bigger than Voxel Dimension (%DBVD) index estimated for each of the six conditions studied in the clinical images dataset: before registration (Pre), Particle Filter (PF), Demons (Dem), Diffeomorphic Demons (DDem), Optical Flow (OF) and PF followed by OF (PF+OF). %DBVD values were calculated from the lung segmentations of the 5 patients studied in the clinical images dataset. For each condition the box plot presents the median value (red line) bounded by the maximum and minimum values.

Table 5.13. Clinical dataset- Gross Target Volume (GTV) registration accuracy. Comparison between six different conditions: before registration (1-Pre), Particle Filter (2-PF), Demons (3-Dem), Diffeomorphic Demons (4-DDem), Optical Flow (5-OF) and PF followed by OF (6-PF+OF) in terms of the Percentage of Distances Bigger than Voxel Dimension (%DBVD). For each condition, %DBVD values corresponding to the registration performed between inspiratory and expiratory phases of the GTV for each of the five patients, alongside with the corresponding mean, standard deviation (std) and median values are presented. Presence of significant differences was assessed by a Kruskall-Wallis test (p<0.05).

%DBVD - GTV

		1 ***Pre***	***2*** ***PF***	***3*** ***Dem***	***4*** ***DDem***	***5*** ***OF***	***6*** ***PF+OF***
P1	***GTV***	72.92	48.02	56.04	56.04	61.23	57.60
P2	***GTV***	80.36	77.67	24.34	25.84	86.03	29.77
P3	***GTV***	70.13	76.26	45.43	43.52	47.48	49.83
P4	***GTV***	16.39	12.30	29.82	37.27	12.12	11.20
P5	***GTV***	71.15	40.38	22.92	20.00	41.61	20.28
	mean	***62.19***	***50.93***	***35.71***	***36.53***	***49.69***	***33.74***
	std	***25.91***	***27.24***	***14.45***	***14.30***	***27.09***	***19.58***
	median	***71.15***	***48.02***	***29.82***	***37.27***	***47.48***	***29.77***
	Kruskall-Wallis	0.40					

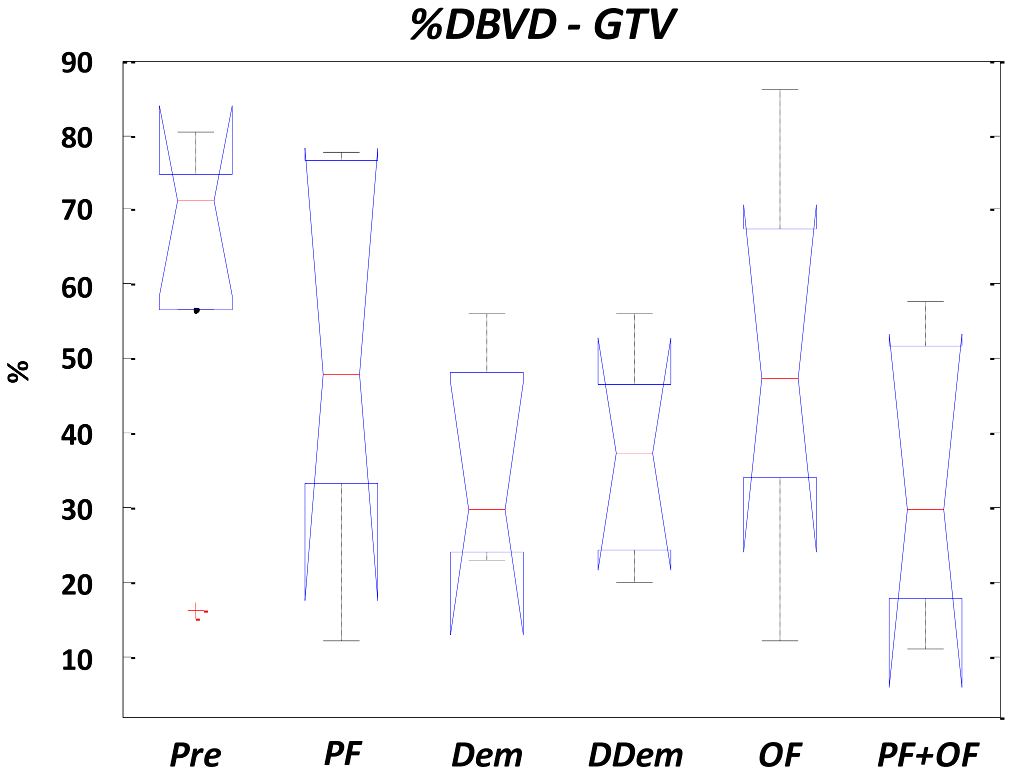

Figure 5.17. **Box plot of the Percentage of Distances Bigger than the Voxel Dimension (%DBVD) index estimated for each of the six conditions studied in the clinical images dataset: before registration (Pre), Particle Filter (PF), Demons (Dem), Diffeomorphic Demons (DDem), Optical Flow (OF) and PF followed by OF (PF+OF). %DBVD values were calculated from the Gross Target Volume (GTV) segmentations of the 5 patients studied in the clinical images dataset. For each condition the box plot presents the median value (red line) bounded by the maximum and minimum values.**

Chapter 6

Discussion

In this work, the aim was to propose an innovative elastic registration method to recover complex deformations presented in RT 4D CT lung images. The proposed PF+OF approach first obtains an accurate global affine transformation using the Particle Filter (PF), and then the transformation is locally refined accurately using a novel discrete iterative Optical Flow (OF) implementation. The characteristics of both algorithms lead to an approach that has a good balance between accuracy and mathematical complexity, which is the main goal of today elastic registration methods used in RT context.

The PF has increasingly been proved to be accurate, robust and, because of its parallelizable structure, it can be also considered a fast algorithm [Arce-Sanata et al., 2010; Arce-Santana et al., 2012; Mejia-Rodriguez et al., 2011; Reducindo, 2010]; while the proposed iterative OF algorithm is accurate enough and has a considerable lower mathematical complexity, with respect to other accurate fluid like algorithms such as Demons and Diffeomorphic Demons [Mani et al., 2013]. In this chapter is presented: the discussion regarding the analysis of the main differences between the proposed PF+OF approach and the algorithm originally proposed by [Arce-Santana et al, 2012], and the evaluation and comparison of the proposed algorithm against other fluid like registration methods, using controlled and clinical 4D CT lung images, based on the analysis of structures of interest. In addition, the conclusion of this work and future directions of research activities related to the proposed PF+OF algorithm are presented.

6.1 Comparison of Algorithms on POPI Model

The POPI model is built up from a real 4D CT lung acquisition, therefore it constitutes a realistic representation of human anatomy and breathing motion [Vandemeulebroucke et al., 2007]. In addition, because it was acquired under the same conditions applied during normal RT treatment planning, the POPI model is widely used for the validation of registration methods because it can provide accurate information about the performance of the algorithms before its use in clinic [Vandemeulebroucke et al., 2007; Janssens et al., 2011; Latifi et al., 2013].

Apart from the mentioned above, the use of the POPI model in this work has three purposes. First, to highlight the impact of the proposed OF process with four control parameters against the original version proposed by [Arce-Santana et al., 2012]; second, to evaluate the impact of PF in the OF process for the registration of 4D CT lung images; and third, to compare the proposed PF+OF approach against the Dem and DDem algorithms, two algorithms widely used with 4D CT lung images for their high performance [Peyrat et al., 2008; Janssens, 2009; Castillo, 2009; Zhong, 2010].

6.1.1 PF+OF comparison- original version vs. four control parameters version

Regarding the comparison against the original version proposed, as stated in chapter 3, two main differences between methods were implemented: first, the modification of the control parameter λ in the regularization term in eq. 3.40 from a constant value to a vector containing a control parameter for each dimension of the image ($\lambda^T = [\lambda_x, \lambda_y \lambda_z]^T$) defined in eq. 3.42; and second, the addition of a regularization term to control the velocity of the optical flow field weighted by a control parameter β (eq. 3.43).

Modification of the control parameter λ was made base on the fact that within 3D images is possible to find anisotropic voxels (different resolutions on axis *x*, *y* and *z*), thus apply equally the regularization term to all image dimensions may lead to irregularities in the 3D deformation field. This issue was not considered in the previous implementation of the method [Arce-Santana, et al. 2010], because isotropic pixel sizes were found in the studied 2D images. Moreover, this modification gives to the user the possibility to adapt the algorithm in terms of the characteristics of the images to be registered, decreasing or increasing λ values according to if a dimension on a particular direction of the voxel is larger or smaller with respect to the others.

On the other hand, the value of the global control parameter β gives the possibility to control the velocity of the whole optical flow, looking for to avoid foldings in the structures of interest due to inhomogeneities in the deformation field; this could be seen as a regularization term that tries to mimic the regularization achieved by the diffeomorphic property of DDem but adding a regularization term less complex that the use of the Lie algebra [Vercauteren et al., 2009], because the global solution of the proposed OF estimation process is computed by a system of linear equations, which ensures a low computational cost. Large values of β lead to a lower velocity of the optical flow, meaning a smaller displacement of the voxels due to the deformation field; therefore, in order to recover complex deformations between images an increase in the number of iterations performed by the OF process will be needed.

A qualitative comparison between the proposed PF+OF algorithm, with four control parameters, and its previous version is shown in figures 5.1 and 5.2. These figures show the result of the registration of respiratory phases 10-30 and 10-60 from the POPI model, using phase 10 as I_T and phases 30 and 60 as I_S respectively. In order to make a fare comparison and highlight the effect of the proposed four control parameters, the λ value of the algorithm with only one control parameter was set equal to the value used in axis x and y of the proposed method (λ=6000), the rest of the parameters (number of particles, number of maximum iterations in PF and OF, etc.) were the same for both implementations. In figure 5.1 is possible to observe that both versions of the PF+OF approach were capable to properly recover deformations between images at the beginning of the inspiration and at 30% of the inspiration; on the other hand, figure 5.2 shows that only the proposed PF+OF was able to realign the lungs between the inspiratory and expiratory phases (phases 10 and 60 of the POPI model respectively), while the algorithm with only one control parameter roughly recovers the misalignments between images but adding inhomogeneities in the borders of some borders of anatomical structures, suggesting that for complex and large deformations the inclusion of the proposed control parameters is desirable for a better performance of the PF+OF algorithm.

It is important to keep in mind that the establish parameters used in this thesis were selected empirically using the information of the 4D CT images of the POPI; the same parameters were used for also for the clinical images dataset in order to test the robustness of the algorithm when analyzing different anatomies. However, establish a methodology to improve the selection of proper parameters and automatize this process base on the characteristics of the images is an issue considered as a future work.

6.1.2 Algorithms comparison by the registration accuracy analysis

For the analysis of registration accuracy using the POPI model, only the lung segmentations provided also by [Vandemeulebroucke et al., 2007] were considered as structures of interest. In figure 5.3 registration performed between respiratory phases 10 (target image, I_T) and 60 (source image, I_S) was selected as example because these are the most distant phases, thus the more difficult registration to achieve is presented (GTV is visible at the inspiratory phase but is completely out of scope in the expiratory phase in the same representative slice). In figures 5.3 (a) to (e) it is possible to observe that all registration methods (PF, Dem, DDem, OF and PF+OF) had an improvement with respect to Pre. Improvements achieved by PF (figure 5.3 (a)) are mainly due to recovery of translations, but it failed recovering the borders surrounding GTV (as expected because PF generates an affine transformation). On the other hand PF+OF and OF (figures 5.3 (e) and (d) respectively) were capable to realign the lungs taking into account the complex deformations due to GTV; demons based algorithms were also capable to recover wraps in the POPI model realigning properly the tumor, results expected been similar to the ones reported by [Vandemeulebroucke et al., 2007] and [Latifi et al., 2013]. In figure 5.3, it is also possible to appreciate similarities and differences between the performance of all four elastic registration methods (figure 5.3 (f)). For this particular qualitative comparison, Dem, DDem and PF+OF stand as the more accurate approaches, while OF present a less smoother result presenting small variations in the borders of the GTV structure. For a better understanding about these differences, the standard indices for the registration accuracy provide quantitative evidence about the registration algorithms performance.

For the DICE index, which gives information about the global overlapping between structures, the best mean improvements were achieved by all four NRR increasing from 0.94 to 0.96, and in terms of the median value PF+OF performs better than the rest of the NRR algorithms but just by an increase of 0.01. The overall improvement of the four NRR algorithms is similar (all of them with significant differences with respect to Pre), with differences between them of less than 1% (no significant differences among them), thus small differences between approaches cannot be properly assessed with DICE index, considering that DICE gives information about the global overlapping, small variations in large size structures, like the lungs, do not have a notable impact.

DMax index gives information about the worst mismatch between structures; in this case PF+OF reduced the maximum mismatch about 2.5 mm, however this result was not statistically different with respect to the original Pre value. Only the demons based algorithms, that improved between 4 and 2.5 mm, were the only ones with significant differences with respect to Pre, but no differences were found among them. Despite the lack of significance in PF+OF, the tendency (decreasing) of the mean value and p-value of 0.07 suggest that in a scenario with more samples the statistical significance may be reach also by the proposed approach.

For ASD, %DBVD and TRE, the impact of the results depend on the voxel dimension, in this case (0.97 x 0.97 x 2.00 mm^3). ASD gives information about the mean mismatch. In this case the four NRR methods reduce the ASD mean value below 1 mm, therefore all four approaches are considered to have a good performance taking into account the voxel size. Nevertheless, it is important to mention that PF+OF shows the best improvement (43% with respect to Pre) with significance difference with respect not only to Pre and PF, but also with respect to DDem (p-value = 0.04), suggesting that for this particular index the proposed PF+OF approach is preferable among all the studied registration algorithms. In addition, the fact that OF was not significant from the other NRR approaches, could be considered as evidence of the positive effect of the PF combined with OF, making preferable PF+OF also with respect to OF.

The %DBVD gives an idea of the distances between structures that are bigger than the voxel thickness; this threshold was selected with the idea to evaluate the robustness of the algorithms. Considering this index, PF+OF has the best performance reducing the percentage from 40.3% (Pre) to 8.7% after the registration process resulting in significant differences with respect to Pre and PF; the same significant differences were found considering OF, putting these two algorithms as the best performers for this particular . On the other hand, demons based methods putting OF and DDem alongside PF+OF as the best performers.

Finally, analyzing the TRE index, PF+OF and the other three NRR algorithms have values below 2 mm, which is considered a satisfactory result being the registration error approximately of the size of a voxel; however, despite the reduction to half of the mean Pre value, no significant differences were found between OF and PF+OF with respect to Pre nor PF. On the other hand, DDem and Dem reduce TRE to values around 1 mm, and particularly DDem presented significant differences with respect to PF, OF and PF+OF, suggesting that the diffeomorphic version of the Demons algorithm is the most adequate approach to assess the TRE. The lack of significance in the NRR methods that used the OF process may be due to the fact that the demons based algorithms used in this thesis work under a multi-resolution scheme, while the proposed algorithms (PF, OF and PF+OF) do not. The TRE has been used previously in literature to evaluate, with the POPI model, Dem, DDem and a Horn-Schunck OF [Vandemeulebroucke et al., 2007; Janssens et al., 2011; Latifiet al., 2013], all of them implemented using a multi-scale approach; results found by these research groups are similar to the ones presented in this work, in terms of the mean values, and no significant differences were found among demons based and optical flow based methods; suggesting that the results found here could be improved when the multi-scale version of the proposed algorithm will be available.

The overall information provided by the standard indices to assess the registration accuracy based on structures of interest suggest PF+OF, alongside the other three NRR algorithms (Dem, DDem, and OF), could be considered to have a good performance registering 4D CT lung images from the POPI model, due to the mean quantitative improvement with respect to Pre, particularly considering the ASD index. However, it is important to state that a larger database and a multi-scale implementation of the proposed algorithm are desirable in order to collect more information that could highlight the benefits of the proposed algorithm. Also, considering the qualitative information provided by the overlapped contours in figure 5.3 (f), it is possible to observe that only PF+OF, Dem and DDem are truly comparable in terms of registration accuracy of the lungs. Despite OF improvement, in this figure is also possible to observe that some mismatching in zones with complex shapes (e.g. around GTV) are presented. Besides, for overlapping information, such as the one provided by the DICE index, the lack of significant differences may be due to the size of the analyzed structures (lungs) in which small differences may not have an impact on the statistics; suggesting that for a better evaluation of the registration accuracy, small and highly deformable structures of interest, such as the GTV, should be taken into account.

6.2 Comparison of Algorithms on Clinical Images Dataset

One drawback of using the information of only one patient of the POPI model to evaluate a new image registration method is that it is limited to a specific anatomy and one breathing pattern. To overcome this limitation and complement the information collected in the previous section, we decide to analyze the proposed algorithms using 4D CT images from five different clinical cases of NSCLC, taking into account different morphologies of lungs and gross target volume (GTV) (see figure 4.4). This two anatomical structures were analyzed independently to avoid bias in the validation because of the different sizes.

Considering the lungs, figure 5.9 shows a good recovery of the misalignment achieved by all four elastic registration approaches; and analyzing the accuracy indices information, results were similar but not equal to the ones found using the POPI model.

In ASD, apart from OF, elastic registration methods reduce the original Pre value below 2mm, being significantly different from Pre and PF, however no significant differences were found between PF+OF, Dem and DDem; particularly in this case the best performance was achieved by Dem, being 3% better than PF+OF. Considering OF, the lack of statistical differences contributes to the idea of the necessity of PF together with OF for a better performance.

A similar performance, with respect to the POPI model analysis, was achieved with DICE index, where all four NRR approaches increased the Pre value from 0.87 above 0.90, in this case PF+OF and Dem stand as the methods with the largest improvement (0.94). Nonetheless, no significant differences were found at all.

In DMax, considerable improvements were achieved by the demons based methods and the PF+OF approach, the best performance were achieved by Dem and DDem with a mean improvement of 20 mm in comparison with Pre (77.89 mm), being 10% better than PF+OF which had a mean improvement of 14 mm; however because of dispersion of the data (large std) also no significant differences were found at all considering DMax.

Similar evidence was observed in %DBVD, where OF and PF+OF achieved the biggest mean improvement (reduction around 15%), but no significant differences were found because of the large variability in the data due to the intra-subject differences of the five study cases.

All the information collected from lung segmentations of the clinical images dataset suggest, as the evidence found in the POPI model analysis, that PF+OF could be considered as an accurate method comparable with Dem and DDem for the analysis of large structures, based on the tendency to improve the standard indices values studied in this thesis, notwithstanding the intra-subject variability.

On the other hand, with the analysis of GTV is possible to collect information about the performance of the methods in a smaller scale. In figure 5.9, the selected example remarks the complex deformation due to the size and shape of the GTV in this particular patient, which is the smallest and amorphous of the available clinical studies. In this case is possible to observe that a good recovery is achieved by all four elastic methods, and that the method capable to recover more details after the registration process was PF+OF (figure 5.9 (h)).

ASD values found for GTV have similarities to those found considering the lungs. Again PF+OF and the demons based algorithms (Dem and DDem) have the best improvements (around 50%) with values below 1.5 mm; despite this improvement, no significant differences were found.

For the DICE index, PF+OF and DDem were the approaches with the best performance (mean value of 0.72 with respect the original Pre value of 0.52); in this case significant differences were found between NRR methods Dem, DDem and PF+OF with respect to Pre, and only PF+OF was statistically different from OF, this fact gives positive evidence regarding the use of PF alongside OF for a better performance of the NRR method. It is important to mention that the improvement of methods is considerably higher, 20% improvement in GTV versus 7% improvement in lungs; result expected because misalignments recovered after the registration process are more representative in small structures (such as GTV) than in large ones (such as the lungs); it was also expected that the mean DICE value (above 0.90) was higher analyzing the lungs than the mean value found considering GTV structures (around 0.70), also because of the size of the structures, and due to the variability of complex deformations studied in the five 4D CT clinical images.

Analyzing DMax, a slightly improvement (around 2.5 mm) was achieved by PF+OF, Dem and DDem algorithms; however no significant differences were found between all conditions. Also for %DBVD, GTV no significant differences were found considering GTV despite the improvement achieved by PF+OF, Dem and DDem methods around 25%.

Overall, the tendency found between accuracy indices in lungs and GTV structures of the clinical 4D CT images dataset is similar but, as expected, differences in mean, std and median values were found due to the different dimension and degree of deformation of the structures, suggesting that PF+OF could be considered as an accurate and robust algorithm to register 4D CT lung images despite differences among anatomical structures of interest. Notwithstanding, the large variability presented among GTV structures limited the evaluation of the methods in a very small scale, because the case presented in figure 5.9 is considerably smaller than the rest of the GTV studied in this work. In particular, for this case the visual inspection suggest that PF+OF could be preferable when small structures with complex shapes are considered; however, more study cases with this kind of structures are needed in order to support this hypothesis and increase the statistical evidence.

Considering the findings using both the controlled and the clinical datasets is possible to state that:

- The affine transformation provided by the PF algorithm has a positive impact, in terms of registration accuracy, when it is used alongside the proposed OF method, forming the PF+OF approach.

- The proposed iterative OF method using four control parameters represents an improvement to the version proposed by the Arce-Santana research group, not only extending the algorithm to its volumetric version, but also making it possible to deal with isotropic and anisotropic voxel sizes (possibility of set different values of λ for each dimension of the image), ensuring also smooth deformation fields due to the global control parameter β.

- The proposed OF algorithm could be considered as a good option to recover complex deformations in 4D CT lung images by itself, however it is recommended to use it alongside PF in order to improve its performance, based on the information provided by the standard indices for registration accuracy.

- The proposed PF+OF approach has shown good results registering 4D CT lung images in both, controlled and clinical cases. Its performance behaves similar, qualitatively and quantitatively, to the Dem and DDem algorithms. It is important to mention that a larger dataset for the quantitative analysis is desirable in order to extract solid statistic evidence about the potential of the proposed method to be considered as a novel NRR method useful in a RT context. In addition, the result presented in this work of PF+OF are not under a multi-scale implementation, as Dem and DDem, therefore improvement in the performance of this method can still be done to the PF+OF implementation developed in this thesis.

- It is important to mention that the lack of consistency between significant differences found considering the POPI model and the clinical images dataset remarks the necessity to increase the data available to perform the analysis of the proposed PF+OF, in order to construct solid evidence based not only on mean or median trends but with consistent and strong statistical conclusions. Furthermore, consider to improve the methodology to extract the contour of the structures of interest would help also in the statistical analysis; the manual contouring inter-observer variability issue could be solve considering the use of validated algorithms to perform the automatic segmentation of structures of interest.

- As mentioned before, results found in this thesis suggest that the proposed PF+OF approach with four control parameters could recover properly the deformation found in 4D CT lung images due to the respiratory movement and / or the effects of the RT treatment, thus it is possible to state that the proposed method could be useful in a clinical context considering that 3D imaging and the selection and delineation of volumes such as GTV, CTV, and OAR, are crucial steps for the RT treatment. Before the use of PF+OF in a real scenario, it is important to mention, again, that a deeper analysis of the proposed algorithm have to done.

6.3 Conclusion

In this work, a novel non rigid registration approach was presented, which is based on a global accurate affine registration using the Particle Filter (PF) followed by an elastic local transformation using a discrete implementation of the Horn-Schunck Optical Flow (OF) with four control parameters. The proposed method, PF+OF, was evaluated using two datasets of 4D CT lung images: the POPI model and a set of five 4D CT images from clinical patients treated for non-small cells lung cancer (NSCLC). Registration accuracy was assessed visually and by computation of indices for the analysis of anatomical structures of interest (lungs and tumor). In addition, a comparison with the Demons (Dem) and Diffeomorphic Demons (DDem) algorithms was performed to assess the accuracy of the proposed approach against methods widely used for the registration of 4D CT lung images.

The results have shown that our NRR method is capable to recover complex deformations presented in the thoracic district caused by the respiratory motion, and is comparable to the state of the art algorithms, suggesting that the PF+OF approach could provide useful information for RT applications, for example, providing useful information to help assessing the dose to be dispensed on the gross target volume (GTV) and organs at risk (OAR) of RT treatment plans generated by the use of 4D CT lung images.

6.4 Future Work

Important future developments related to the work presented in this thesis could be:

- Optimization of the PF+OF registration process. A multi-core implementation of PF and a multi-scale approach of the OF registration process are considered as a first future development; in this way, a considerable speed up of the registration method would be achieved, thus a full comparison between PF+OF, Demons and Diffeomorphic Demons algorithms considering both, accuracy and speed processing, could be analyzed. This implementations are projected to be developed in the next month.

- Improvement of the 4D CT lung images dataset for a more robust evaluation of the PF+OF method, taking into account inter-subject variability to assess the performance of the method with different breathing patterns and considering different anatomical shapes, in both controlled and clinical cases is recommended. The improvement of the dataset will also help with the statistical significance of the PF+OF method. This point is projected to be reach also in a near future.

- Application of the PF+OF approach to different anatomical districts and image modalities, e.g. the head-and -neck track using MR images, to study the accuracy and impact of the method with different medical protocols. Preliminary results in 2D about this topic are presented in appendix A.

- Evaluation of the PF impact on different non-rigid registration algorithms. The main hypothesis of this future development is that non rigid registration algorithms in which the initial rigid transformation is crucial for the accuracy (e.g. B-Splines Free Form Deformation) could be benefit from the robustness of PF.

- To extend the use of the PF+OF approach to multimodal cases by applying a local intensity mapping to the images in order to overcome the monomodal restriction of the method. Metrics such as the Entropy as a local variability measure, or the conditional statistics of the joint intensity distribution will be studied. Initial results with 2D CT-MR brain images are presented in appendix B.

- Evaluating the registration accuracy of the proposed method based on the analysis structures of interest represented by mesh data structures. The motivation of this future work and an example of the proposed registration accuracy indices for the analysis are presented in appendix C.

- Introduction of this novel registration method within a software package (such as the Insight Toolkit - ITK) to make it available for its general use with clinical images.

Appendix A

Elastic Registration in Radiotherapy Images with Brain Deformations

In the present work it has been proved that PF+OF approach is a good option to recover complex deformations presented in 4D CT lung images due to respiratory movements. Despite the results presented in this thesis, PF impact could not be assessed properly because patients remain in the same position during images acquisition, therefore rigid deformations are limited. On the other hand, images acquired during different sessions of a RT treatment have to correct first misalignments due to patients repositioning with a global registration step in order to achieve a good elastic registration. Within this context, in this appendix the first results of PF+OF method using 2D CT and MR images with brain deformations caused by anatomical modifications of the tumor are presented. For both image modalities, synthetic and real cases were studied. Registration results showed good accuracy, qualitatively and quantitatively, suggesting that the PF+OF approach may be considered as a good new option for RT applications like patient's follow up treatment in the head-and-neck tract. The present appendix is based on the article :

Mejia-Rodriguez A, Arce-Santana ER, Scalco E, Tresoldi D, Mendez MO, A. M. Bianchi, G. M. Cattaneo, G. Rizzo. *"Elastic registration based on particle filter in radiotherapy images with brain deformations"*. Proceedings of the 33rd Annual International Conference of the IEEE Engineering in Medicine and Biology Society; 2011: 8049–8052.

33rd Annual International Conference of the IEEE EMBS
Boston, Massachusetts USA, August 30 - September 3, 2011

Elastic Registration Based on Particle Filter in Radiotherapy Images with Brain Deformations

A. R. Mejia-Rodriguez, E. R. Arce-Santana, E. Scalco, D. Tresoldi, M. O. Mendez, A. M. Bianchi, G. M. Cattaneo, G. Rizzo.

Abstract—**This paper presents the evaluation of the accuracy of an elastic registration algorithm, based on the particle filter and an optical flow process. The algorithm is applied in brain CT and MRI simulated image datasets, and MRI images from a real clinical radiotherapy case. To validate registration accuracy, standard indices for registration accuracy assessment were calculated: the dice similarity coefficient (DICE), the average symmetric distance (ASD) and the maximal distance between pixels (Dmax). The results showed that this registration process has good accuracy, both qualitatively and quantitatively, suggesting that this method may be considered as a good new option for radiotherapy applications like patient's follow up treatment.**

Index Terms—**Elastic image registration, particle filter, optical flow, simulation datasets, radiotherapy real clinical case.**

I. INTRODUCTION

ONE important subject in medical image analysis is image registration [1], which consists in a spatial remapping of one image to another to obtain a voxel by voxel correspondence of the same anatomical structures in the two images. In fact, image registration is useful to recover organ deformations during the evolution of certain diseases or the treatment of them. In particular, in radiotherapy, it allows the estimation of strains that can be caused by increase or reduction of tumors treated with radiation, or by side effects such as weight loss or increase / reduction of the healthy organs surrounding the tumor [2].

In the last years, image registration has been approached with rigid and non-rigid techniques. Rigid registration methods assume that the same global transformation is applied to each image pixel, thus reducing the problem to find only the parameters which describe the global transformation. However, these methods present serious drawbacks when one of the images shows complex deformations with respect to the other one. On the other hand, non-rigid or "elastic" registration methods estimate a transformation for each pixel, incorporating only weaker smoothness assumptions in order to make the problem well-posed. Elastic methods are more general than the rigid ones but also more computationally demanding, and difficult to implement and calibrate [3].

Recently, a new approach has been proposed for rigid registration, based on the Particle Filter (PF), an algorithm commonly used for parameter estimation in dynamical systems [4]. In this method, an iterative stochastic search is performed using a Monte Carlo model. This new approach based on PF has been also adapted to non rigid image registration cases, by incorporating an optical flow approximation [5]. This iterative process is reported to be easy to implement and powerful enough to achieve complex non-rigid registrations; however, before its application on a real clinical context, validation of the algorithm accuracy should be performed.

In this work, the evaluation of PF elastic registration accuracy is carried out in the case of 2D images, using simulated data. Its application to a real clinical case is also shown.

II. METHODS

A. Simulated Image Datasets

CT and MRI studies of two patients with cerebral tumor treated with macroscopically total resection were selected, in which the presence of deformations in the head and neck tract caused by tumors were evident. These patients underwent pre-operative diagnostic, surgical resection and radiotherapy treatment at the San Raffaele Hospital in Milan, Italy.

CT and MR 2D images of three different sections of the head were selected to study different morphological structures; each image was deformed in a controlled way (5 deformations per image).

The controlled deformations were obtained using the Moving Least Squares (MLS) algorithm [6], which is a deformation technique that allows to compute a map

---

Manuscript received April 14, 2011.

A. R. Mejia-Rodriguez is with Institute of Molecular Bioimaging and Physiology (IBFM)-CNR, Milan, Italy and Bioengineering Department, Politecnico di Milano, Milan, Italy. Author is supported by CONACyT studentship (CVU/Becario): 217232/213579 for PhD studies (e-mail: armero83@gmail.com)

E. R. Roman-Arce is with Fac. de Ciencias, UASLP, San Luis Potosi, Mexico.

E. Scalco is with Institute of Molecular Bioimaging and Physiology (IBFM)-CNR, Milan, Italy

D. Tresoldi is with Institute of Molecular Bioimaging and Physiology (IBFM)-CNR, Milan, Italy and Bioengineering Department, Politecnico di Milano, Milan, Italy.

M.O. Mendez-Garcia is with Fac. de Ciencias, UASLP, San Luis Potosi, Mexico.

A.M. Bianchi is with Bioengineering Department Politecnico di Milano, Milan, Italy.

G. M. Cattaneo is with Dept. of Medical Physics, Scientific Institute San Raffaele, Milan, Italy.

G. Rizzo is with Institute of Molecular Bioimaging and Physiology (IBFM)-CNR, Milan, Italy and Dept. Nuclear Medicine, Scientific Institute San Raffaele, Milan, Italy.

f:R2→R2 from the transformation of a set of N pivot points "p" in new positions "q". For the simulated deformations we put 6 pivot points initially placed at 60, 120, 180, 240, 300 and 360 degrees around the outer structure of each image. Subsequently, these pivot points were moved, randomly, ±5–10 pixels, both in x-axis and y-axis, to generate the corresponding warps.

Two simulated datasets were thus obtained:

1. CT simulated dataset; original CT images with their corresponding simulated deformations.
2. MRI simulated dataset; original MRI images with their corresponding simulated deformations.

It should be emphasized that for evaluation purposes, simulation was intended to study deformations even exaggerated or impossible to find in actual radiotherapy clinical cases.

B. Clinical Images

A real clinical case was considered using MRI images acquired before (MRI-Pre) and after (MRI-Post) a radiotherapy treatment, where it is possible to observe deformations of brain structures, in the axial plane, due to the tumor shrinkage as a result of the treatment. In this case the proposed method was used to remap post-treatment imaging back to pre-treatment images in order to estimate brain structures changes occurred during treatment.

A slice by slice correspondence between MRI-Pre and MRI-Post was obtained, using the rigid registration software available on the radiotherapy plan computer.

C. Parametric Particle Filter

The Particle Filter (PF) is a method based on Bayesian approach that uses a Montecarlo algorithm to estimate a probability density function (pdf) [4]. The goal of the PF is to obtain a posterior pdf at time k, through a set of test points θ_k^j (particles: in this case the parameters of an affine transformation) with associated weights $\{\theta_k^j, W_k^j\}_{j=1}^{Ns}$, such that $\sum_{j=1}^{Ns} W_k^j = 1$, and N_S the particle number.

The PF algorithm is an iterative process composed of two stages:

1. *Prediction stage*: each particle is modified by a random walk pattern ($\theta_k = \theta_{k-1} + v_{k-1}$, where v_{k-1} represent i.i.d. noise samples), through a recursive propagation of the particles at time k. A resampling process is needed in order to select only the best particles to be propagated, solving the Degeneracy Problem (particles with negligible weights).
2. *Update stage*: the weights are recalculated according to the measurements z_k, using the likelihood function $P(z_k|\theta_k)$, defined by the measurement model in order to obtain representatives samples of $P(\theta_k|z_k)$ [5].

The algorithm uses mutual information (MI) as likelihood measurement in the image registration process, thus it is possible to define the output measurement $z_k$as:

$$z_k = MI(I_T(x,y), I_S(T_{\theta_k}(x,y))) + w_k \qquad (1)$$

where I_T and I_S are the target an source images, $T_\theta(.)$ is the geometric (affine) transformation and w_k represent i.i.d. noise samples; if I_S is the result of a bijective intensity mapping for I_T, then, by using the property of MI [5], and the entropy H(.) of the I_S, it is possible to define $P(z|\theta)$ as likelihood metric [7]:

$$P(z|\theta) = \frac{1}{\sigma\sqrt{2\pi}} exp\left\{-\frac{[H(I_T(C)) - MI(I_T(C), I_S(T_\theta(C)))]^2}{2\sigma^2}\right\}, \qquad (2)$$

for a given measurement noise variance σ^2>0 and a set of m equispaced pixels $C = \{(x_i, y_i); i = 1, \ldots, m\}$, in both images. Note that (2) reaches its maximum when $I_S(C) = F(I_T(T_\theta(C)))$, where F(.) denotes an injective intensity mapping.

D. Elastic Registration using PF and optical flow

For the elastic registration the key idea lies in a two step iterative algorithm; first, the global affine registration between both images using the PF approach is computed; second, the transformation is locally refined for each pixel using an optical flow approximation [5]. The aligned candidate image, obtained at each iteration, is used as the input candidate image in the following iteration until convergence is reached. An important advantage on this method is that only a few control parameters are required and these parameters are robust with respect to the images to be registered. In the case of affine registration, the parameters are the number of particles and the number of iterations, while, for optical flow, estimation requires taking into account the number of iterations and the value of a regularization factor λ, that controls the smoothness of the resulting flow field. In this work for all the registrations we used 300 particles and 200 iterations for calculating the affine transformation, and 50 iterations with λ=5000 for the computation of optical flow. All these experiments were performed on a PC running at 3.06 GHz.

E. Registration accuracy on simulated data

The algorithm was applied to the simulated datasets, using the parameters mentioned above; the mean registration time was 45 seconds.

To validate registration accuracy, in both internal and external brain structures, segmentation of some structures of interest were performed: in each simulated study an expert in radiological images interactively drew the brain contour (including the main sulci), the lateral cerebral ventricles contours (divided in top and bottom left/right ventricles) and the tumor boundary using MIPAV software [8].

From these data, differences in structures between original and deformed images (pre registration) and between original and post registration images were calculated using standard indices usually adopted for registration accuracy assessment [9]: the dice similarity coefficient (DICE), the average symmetric distance (ASD) and the maximal distance between pixels (Dmax).

The value of DICE ranges from 0, indicating no spatial overlap between two sets of binary segmentation results, to 1, indicating complete overlap. ASD is based on the contour pixels of two segmentations A and B. For each contour pixel of B, the Euclidean distance to the closest surface pixel of A is calculated and stored. In order to provide symmetry, the same process is applied from contour pixel of A to B. The ASD is then defined as the average of all stored distances, which is 0 for a perfect segmentation. The Dmax index calculates the maximum distance between the analyzed overlapped contours, where zero means a perfect overlap.

F. Clinical Case Registration

The algorithm was applied to the clinical images, using the same parameters set for the simulated datasets. For these images the registration time was 46 seconds.

Qualitative analysis of the algorithm performance was carried out by an expert physician, taking into account the misalignment recovery of particular structures (right ventricle and tumor). Quantitative analysis was performed using the same criterion applied in simulated data.

III. RESULTS AND DISCUSSION

A. Simulated data

Figure 1 shows an example of the results found using images with simulated deformations in both MRI (row a) and CT (row b) images. In this figure, we can see (by columns) the original images, the deformed images and their respective registration (resulting image). It could be observed that the PF has made an acceptable registration between images. Qualitatively, registered images look very similar to the original ones, regardless of the degree of the applied strain. The good recovery is particularly evident by looking at the contours of the brain, the brain ventricles and the tumor (white area at the top left).

Complementing figure 1, Table I shows the results of calculated indices DICE, Dmax and ASD in CT-CT and MR-MR registrations. Values were calculated for pre and post registrations, corresponding to values of the pairs original-deformed images and original-registered images respectively, of the 5 strains applied (Def 1, Def 2, Def 3, Def 4 and Def 5). It also presents the mean, standard deviation and median values for each pre and post indices.

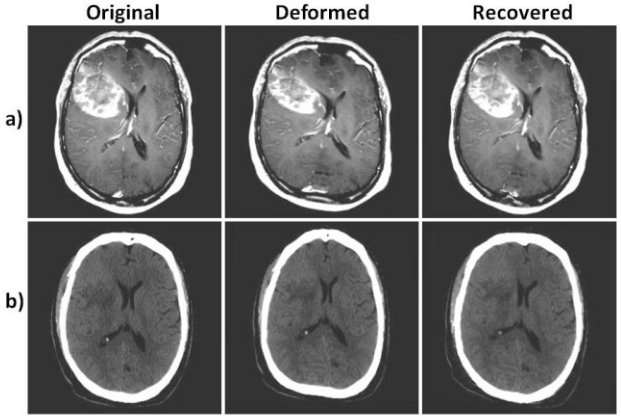

Fig. 1. a) MRI images, b) CT images.

The values of pre and post ASD were about 2.70 ± 0.59 mm and 0.80 ± 0.41 mm for CT, 2.68 ± 0.43 mm and 0.92 ± 0.60 mm for MR, while Dmax values decreased from 7.76 ± 1.68 mm to 3.46 ± 1.23 mm for CT and 8.47 ±1.57 mm to 3.80 ± 1.17 mm in MR respectively. Taking into account that the pixel size of these images is 0.819 mm, these results show that the uncertainties in the alignment of the structures were reduced to values comparable to the pixel size. For DICE index results show a considerable improvement since the found values increased from 0.55 ± 0.28 for CT and 0.48 ± 0.07 for RM, to 0.86 ± 0.19 and 0.85 ± 0.10 respectively, indicating that the overlap of the contours had an improvement from 50% to 85%.

TABLE I
REGISTRATION ACCURACY IN SIMULATED DATA.
EACH DEFORMATION VALUE (DEF) IS THE MEAN VALUE OF THE BRAIN AND VENTRICLES STRUCTURES FOR EACH SIMULATION.

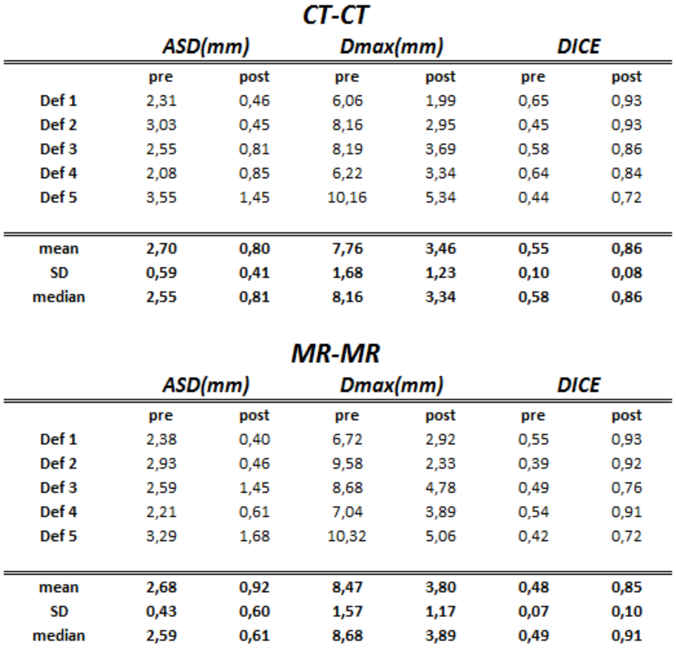

CT-CT

	ASD(mm)		Dmax(mm)		DICE	
	pre	post	pre	post	pre	post
Def 1	2,31	0,46	6,06	1,99	0,65	0,93
Def 2	3,03	0,45	8,16	2,95	0,45	0,93
Def 3	2,55	0,81	8,19	3,69	0,58	0,86
Def 4	2,08	0,85	6,22	3,34	0,64	0,84
Def 5	3,55	1,45	10,16	5,34	0,44	0,72
mean	**2,70**	**0,80**	**7,76**	**3,46**	**0,55**	**0,86**
SD	**0,59**	**0,41**	**1,68**	**1,23**	**0,10**	**0,08**
median	**2,55**	**0,81**	**8,16**	**3,34**	**0,58**	**0,86**

MR-MR

	ASD(mm)		Dmax(mm)		DICE	
	pre	post	pre	post	pre	post
Def 1	2,38	0,40	6,72	2,92	0,55	0,93
Def 2	2,93	0,46	9,58	2,33	0,39	0,92
Def 3	2,59	1,45	8,68	4,78	0,49	0,76
Def 4	2,21	0,61	7,04	3,89	0,54	0,91
Def 5	3,29	1,68	10,32	5,06	0,42	0,72
mean	**2,68**	**0,92**	**8,47**	**3,80**	**0,48**	**0,85**
SD	**0,43**	**0,60**	**1,57**	**1,17**	**0,07**	**0,10**
median	**2,59**	**0,61**	**8,68**	**3,89**	**0,49**	**0,91**

B. Clinical Images

Figure 2 shows the result for the real clinical case, in which the right hemisphere of the brain is affected by the tumor. In this figure pre-treatment, post-treatment and recovered images are presented.

To analyze the efficiency of the registration, arrows were placed pointing the most deformed structures (cerebral ventricles and tumor). Comparing the post-treatment image with respect to the pre-treatment one, deformations on the brain ventricles structures of the right hemisphere are observed; also a shrinking of the tumor is present. Analyzing the recovered image and the pre treatment image, it is possible to appreciate that the shape of the ventricles is properly recovered, maintaining the tumor's shrinkage. Table II presents the results obtained with ASD, Dmax and DICE indexes in this particular case, confirming qualitatively the efficiency of the proposed registration method in real clinical data. These results suggest that the methodology proposed in this work may be helpful for following up studies in radiotherapy thanks to its good performance and accuracy.

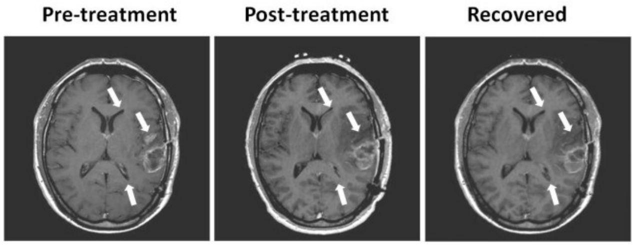

Fig. 2. Real MRI clinical case images elastic registration.

TABLE II
REGISTRATION ACCURACY IN CLINICAL DATA.

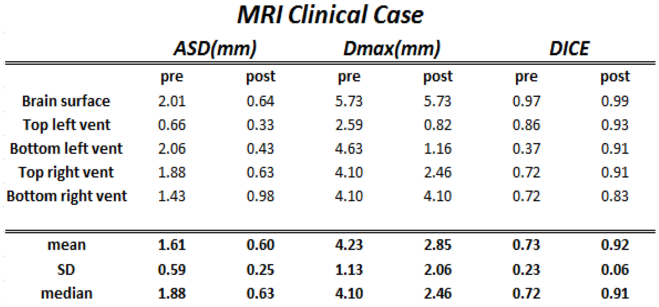

MRI Clinical Case

	ASD(mm)		Dmax(mm)		DICE	
	pre	post	pre	post	pre	post
Brain surface	2.01	0.64	5.73	5.73	0.97	0.99
Top left vent	0.66	0.33	2.59	0.82	0.86	0.93
Bottom left vent	2.06	0.43	4.63	1.16	0.37	0.91
Top right vent	1.88	0.63	4.10	2.46	0.72	0.91
Bottom right vent	1.43	0.98	4.10	4.10	0.72	0.83
mean	**1.61**	**0.60**	**4.23**	**2.85**	**0.73**	**0.92**
SD	**0.59**	**0.25**	**1.13**	**2.06**	**0.23**	**0.06**
median	**1.88**	**0.63**	**4.10**	**2.46**	**0.72**	**0.91**

IV. CONCLUSIONS

This work evaluated the accuracy of elastic registration guided by the particle filter (PF) with an optical flow process in 2D. In CT and MRI images of radiotherapy patients, in both simulated and real environment, registration showed good accuracy, both qualitatively and quantitatively. These results, in terms of accuracy, corroborate the advantages already mentioned on PF approach such as easy implementation, robustness to initial parameters and speed processing [7],[8], suggesting that extending it to a 3D registration process may be considered as a good new option for radiotherapy applications like patient's follow up treatment.

REFERENCES

[1] Hill D.L., Batchelor P.G., Holden M., Hawkes D.J. "Medical image registration". Phys Med Biol. 2001;46:R1-45.

[2] Faggiano E., Cattaneo G.M., Ciavarro C., Dell'Oca I, Persano D., Calandrino R. Rizzo G." Validation of an elastic registration technique to estimate anatomical lung modification in Non Small-Cell Lung Cancer Tomotherapy". Radiat Oncol. 2011 , in press

[3] Zitova B., Flusser J., "Image registration methods: a survey", Image and Vision Computing 21, 2003.

[4] Arce-Santana E.R., Campos-Delgado D. U., Alba A., "Image registration guided by particle filter", in *advances in Visual Computing, Part I,* ser. Lecture Notes in Computer Science, vol. 5875. Springer-Verlag, Nov. 2009, pp. 554–563.

[5] Arce-Santana E.R., Campos-Delgado D. U., Alba A., "A non-rigid multimodal image registration method based on particle filter and optical flow", Lecture Notes in Computer Science, 2010, Volume 6453/2010, 35-44.

[6] Schaefer S., McPhail T., Warren J., "Image Deformation Using Moving Least Squares". *ACM Transactions on Graphics (TOG) - Proceedings of ACM SIGGRAPH 2006*, Volume 25 Issue 3, July 2006.

[7] Reducindo, I.; Arce-Santana, E.R.; Campos-Delgado, D.U.; Alba, A.; , "Evaluation of multimodal medical image registration based on Particle Filter," *Electrical Engineering Computing Science and Automatic Control (CCE), 2010 7th International Conference on*, pp.406-411, 8-10 Sept. 2010.

[8] McAuliffe, M. J., F. M. Lalonde, D. McGarry, W. Gandler, K. Csaky, and B. L. Trus. "Medical Image Processing, Analysis & Visualization In Clinical Research." In: CBMS '01: Proceedings of the Fourteenth IEEE Symposium on Computer-Based Medical SystemsAnonymous Washington, DC, USA: IEEE Computer Society, 2001, pp. 381.

[9] Faggiano, E.; Fiorino, C.; Scalco, E.; Broggi, S.; Cattaneo, M.; Maggiulli, E.; Dell'Oca, I.; Di Muzio, N.; Calandrino, R.; Rizzo, G. An automatic contour propagation method to follow parotid glands deformation during head-and-neck cancer Tomotherapy. Physics in

[10] Medicine and Biology, 2011. 56 (3), pp 775-791

Appendix B

Multimodal Image Registration Approach Based on Local Variability Measures

Non-rigid registration algorithms based on the optical flow concept work under the assumption of intensity conservation between voxels of the images to be registered, limiting these algorithms to monomodal registration cases. In medical imaging, multimodal image registration is useful in a clinical context because different types of medical images could lead to better identifying structures of interest for the RT treatment plan, such as the tumor and organs at risk, and for studying the efficiency of RT and its collateral effects. In this appendix a novel proposal to overcome the monomodal restriction and adapt the PF+OF approach to multimodal registration cases is presented. The main idea is to add a step which maps images from different modalities into a space where their intensities can be compared, such as the intensity variability around neighbor elements of a voxel. Four measures that meet the above description, which we call Local Variability Measures (LVM's) based on the entropy and variance computed over a window centered in a pixel of interest, are implemented to achieved the PF+LVM+OF multimodal registration method. These methods were tested using 2D CT and MR images from patients with cerebral tumor. Images with synthetic deformations and real warps due to RT treatment were studied. The resulting registrations were evaluated both qualitatively and quantitatively by standard indices of correspondence over anatomical structures of interest in RT (brain cortex, tumor and cerebral ventricles). These results showed that one of the proposed LVM (entropy) offers a superior performance in estimating the non-rigid deformation field. The present chapter is based on the article :

Isnardo Reducindo, Aldo R. Mejia-Rodriguez, Edgar R. Arce-Santana, Daniel U. Campos-Delgado, Flavio Vigueras-Gomez, Elisa Scalco, Anna M. Bianchi, Giovanni M. Cattaneo, Giovanna Rizzo. *"Multimodal Non-Rigid Registration Methods Based on Local Variability Measures in CT and MR Brain Images"*. IET Image Processing (submitted 2013).

Introduction

Multimodal image registration is the process of geometrically align two or more overlaying images from different modalities (CT, MRI, PET, etc.). Applications of multimodal non-rigid registration (NNR) are abundant and diverse, predominantly diagnostic in nature. For instance, multimodal NRR is useful in radiotherapy (RT), where different types of medical images could lead to better identifying the structures of interest for the RT treatment plan, such as the tumor and organs at risk (OAR), and for studying the efficiency of RT and its collateral effects [Rueckert et al., 2010; Bin et al., 2010]; for example when 3D conformal radiotherapy treatment planning (CRTP) is employed for tumor treatment, the relative position between the tumor and its adjacent tissues could be obtained accurately through analyzing the medical data sets, which fuse the information of functional and anatomical images [Bin et al., 2010]. In literature, current multimodal registration techniques, such as those based on Sum of Squared gray value Differences (SSD) and Mutual Information (MI), attempt to find similarities between images obtained from different modalities in a direct fashion, without a prior knowledge [Hill et al., 2001]. This is often very difficult as images acquired from different modalities can have very different intensity mappings.

In this context, the work presented in this appendix pursues to overcome the monomodal restriction of the PF+OF algorithm, by applying a local intensity mapping over the images, after an initial parametric registration. In this proposal, the multimodal images are mapped into a space where their intensities can be compared, in order to perform an OF algorithm iteratively, as proposed in [Reducindo et al., 2012].

Methods

Multimodal non-rigid registration based on local variability measures

As mentioned in previous chapters, the NRR problem can be formulated as to find the displacements vector field $V(\mathbf{r})$ such that it can align a source image, I_S,with a target one, I_T. Then, the problem can be mathematically written as follows:

$$I_T(\mathbf{r}) = F\big[I_S\big(\mathbf{r} + V(\mathbf{r})\big)\big], \tag{1}$$

where $\mathbf{r} = (x, y)^\top$ denotes a pixel position within the rectangular domain $\Omega \subset \mathbb{R}^2$ of the images, and $F[\cdot]$ represents the relation between the intensities of both images $I_T$and I_S. According to eq. (1), F is the identity if the two images are monomodal, and the registration problem can be solved by the PF+OF algorithm, where the vector field of the non-rigid deformation is obtained by adding the rigid vector field, achieved by the PF, to the one obtained by the iterative OF process. For details of the implementation the reader is referred to chapter 3.

For the case of multimodal NRR an extension of the PF+OF methodology is proposed in order to overcome the limitations by applying an intensity mapping over the images by using measures that describe the intensity variability around each pixel [Reducindo et al., 2012]. This mapping transforms both images into a space where each pixel intensity in one image could be compared with its corresponding in the other image, despite their intrinsic multimodal characteristics; namely, establishing a mapping $G[\cdot]$ such that:

$$G[I_T(\mathbf{r})] = G\left[I_S\left(\mathbf{r} + V(\mathbf{r})\right)\right], \tag{2}$$

In order to define this mapping, we propose to employ measures that do not depend on the intensity level of the pixels, but on their intensity variability around neighbor elements. Two measures that meet the above description are the entropy and the variance, computed over a window centered in a pixel of interest, which we call Local Variability Measures (*LVM*s). In addition, we also propose to employ a combination of these two metrics in order to take advantage of the local information that they capture. Hence, the Euclidean and maximum weights are used, similarly to the two and infinity norms of 2-D vectors. The proposed methodology *PF+LVM+OF* for multimodal NRR adds two intermediate steps between the rigid and the elastic registration to the algorithm described in previous chapters:

1. Parametric (rigid) registration, Find the parameters vector $\widehat{\theta}$ of the perspective transformation $T\left(\mathbf{r}|\widehat{\theta}\right)$ that provide the best alignment between $I_T(\mathbf{r})$ and $I_S(\mathbf{r})$, and compute the initial (rigid) displacement vector field $d_0(\mathbf{r})$.

2. Intensity mapping based on *LVM*. Apply the mapping $G[\cdot]$ based on a *LVM* over all the pixels $\mathbf{r}$ in the images $I_T(\mathbf{r})$ and $\tilde{I}_S(\mathbf{r})$. That is, compute the intensity mapping, and obtain $\tilde{I}_T(\mathbf{r}) \triangleq G[I_T(\mathbf{r})]$ and $\tilde{I}_S^0(\mathbf{r}) \triangleq G\left[I_S\left(\mathbf{r} + d_0(\mathbf{r})\right)\right]$, according to the following four proposals:

$$G_1[I(\mathbf{r})] = \sum_{\mathbf{s} \in N_{\mathrm{r}}} p_{\mathbf{r}}\left(I(\mathbf{s})\right) \log[I(\mathbf{s})], \tag{3}$$

$$G_2[I(\mathbf{r})] = \sum_{\mathbf{s} \in N_{\mathrm{r}}} p_{\mathbf{r}}\left(I(\mathbf{s})\right) [\mu_{\mathbf{r}} - I(\mathbf{s})]^2, \tag{4}$$

$$G_3[I(\mathbf{r})] = \sqrt{G_1[I(\mathbf{r})]^2 + G_2[I(\mathbf{r})]^2}, \tag{5}$$

$$G_4[I(\mathbf{r})] = \max_{\mathbf{r}}\{G_1[I(\mathbf{r})], G_2[I(\mathbf{r})]\}, \tag{6}$$

where G_1 represents the *LVM* using entropy, G_2 using variance, G_3 an Euclidean weight between variance and entropy, and G_4 selecting the maximum value between variance and entropy at each pixel. In addition, N_{r} represents the set of pixels of a $n \times n$ window centered at $\mathbf{r}$, $p_{\mathrm{r}}\left(I(\mathrm{s})\right)$ is the local probability distribution of the image intensities $I(s)$ within N_r, and μ_r is the average value of the intensity $I(s)$with s $\in N_\mathrm{r}$.

3. Equalization. After the transformation, the intensities of the images ($\tilde{I}_T$ and $\tilde{I}_S^0$) could have small values and could be concentrated in a short dynamic range. For this reason, it is necessary to scale the two images intensities into a range from 0 to 255 (grayscale), and to apply a histogram equalization [Gonzalez, 2009].

4. Optical Flow. Find the remaining displacements between I_T and $\tilde{I}_S^0$ by an OF iterative scheme, $d(\mathbf{r}) = d_1(\mathbf{r}) + d_2(\mathbf{r}) + \cdots + d_k(\mathbf{r})$, until convergence is achieved.

5. Non-rigid registration. Finally, we can obtain the vector field of the non-rigid multimodal deformation by adding the rigid vector field to the one obtained by the iterative OF, i.e., $V(\mathbf{r}) \triangleq d_0(\mathbf{r}) + d(\mathbf{r})$.

Clinical and synthetic images datasets

CT and MR clinical studies of three patients with cerebral tumor were selected for evaluation purposes. In these studies, it is possible to observe deformations of the brain structures in the axial plane, due to tumor shrinkage as a result of the medical treatment. These patients underwent pre-operative diagnostic and RT treatment at the San Raffaele Hospital in Milan, Italy. The dataset was composed by a CT scan and a MR image before the RT treatment (CT-Pre and MR-Pre), and a MR image after the treatment (MR-Post). From the three clinical studies, ten pairs of CT/MR 2D images of different sections of the head were selected to study different morphological structures. Each image has a dimension of 512 x 512 pixels with a pixel size of 1.0 × 1.0 mm. A slice-by-slice correspondence between CT-Pre and both MR images (Pre and Post) was obtained by using the software available in the Treatment Plan System.

In addition to the clinical dataset, we generated new synthetic data for the algorithm evaluation, where two MR-Pre images of different sections of the head were deformed in a controlled way (three deformations per image) by using the Moving Least Squares (MLS) algorithm [Schaefer et al., 2006]. This algorithm allows to compute a transformation map L: $\mathbb{R}^2 \rightarrow \mathbb{R}^2$ from a set of *N* pivot points "p" and their corresponding new positions "q". These deformations were constructed to simulate the ideal effect of the RT treatment, i.e. only the tumor suffers shrinkage due to the therapy but the healthy organs surrounding it remain intact. Therefore, for the simulated deformations, we placed six initial pivot points on the brain contour and six around the tumor. Subsequently, only the pivot points of the tumor were moved to an inner position closer to the center of the tumor, to simulate a shrinking effect. Meanwhile, the pivot points on the brain contour remained at the same positions. In this way, the NRR process was performed between a CT-Pre image and the synthetically modified MR-Pre image.

Registration accuracy

First, an expert physician evaluated the results of the registration process by visual inspection, in order to label the performance as acceptable or not acceptable from a clinical point of view. Then, segmentations of the structures of interest (brain cortex, ventricles and tumor), in both synthetic and clinical datasets, were carried out for each of the 4 images obtained after the registration with the *PF+LVM+OF* method, and for the original *PF+OF* implementation (without *LVM*). For analysis purposes, we define LVM_k as the *PF+LVM+OF* approach by using the mapping G_k, as described in equations (3-6), and *No-LVM* for just *PF+OF*. Due to the difficulty in properly locating anatomical structures just by using the CT image, a CT-Pre/MR-Pre correspondence was used to ensure a proper segmentation of the structures of interest in CT images, where contour delineations of the structures in MR-Pre images were used for this purpose. These segmentations were performed by an expert observer through the MIPAV software [McAuliffe et al., 2001] (see Figure 1). From these segmentations, differences in anatomical structures before and after the registration process were calculated by using standard indices usually adopted for accuracy assessment: area difference (ADiff), dice similarity coefficient (DICE), average symmetric distance (ASD), and maximum symmetric distance (DMax) [Mejia-Rodriguez et al., 2011; Faggiano et al., 2011-b; Wang et al., 2008; Heimann et al., 2009] (indices definitions can be found in section 4.5 of this document).

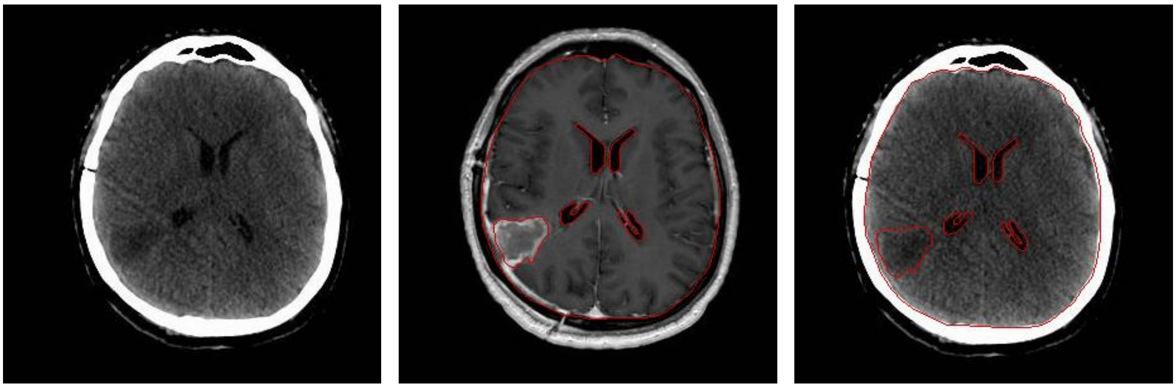

Figure 1. A pair of the set of images used for the algorithm evaluation. (a) CT-Pre, (b) MR-Pre with contours of the anatomical structures of interest, and (c) CT-Pre with contours of the anatomical structures of interest obtained from MR-Pre.

To avoid bias in the quantitative evaluation due to differences in the dimensions of the structures of interest, the resulting indices were analyzed for each type of anatomical structure (brain contour, ventricles and tumor). So the evaluation results are presented as mean ± std for each of the three structures. Additionally, in the synthetic images, eight markers were placed around the tumor with the goal of estimating the Euclidean distance between the coordinates of the markers in the images, before and after the registration process (see figure 2).

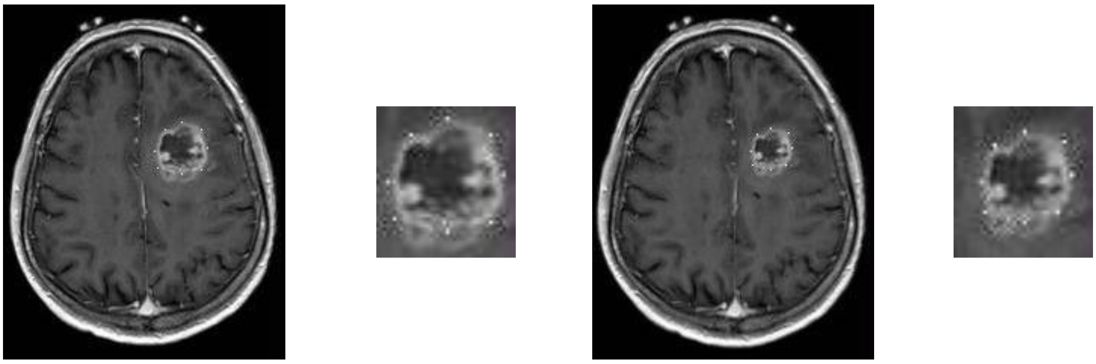

Figure 2. Example of a MR-Pre image used to generate a synthetically deformed image with eight markers placed around the tumor. (a) MR-Pre, (b) MR-Pre tumor, (c) MR-Pre deformed image in a controlled way, and (d) Tumor of the MR-Pre deformed image.

Results

Synthetic images

Figure 3 shows an example of the registration results obtained by the different *LVM*s proposed in this paper, where a CT-Pre image is used as I_T, and an MR-Pre synthetically deformed as I_S. Table 1 presents the overall results of the accuracy indices for brain contour and tumor. Results show a similarity in ADiff for the brain contour, before and after the registration process (for any *LVM*); while in the tumor, a considerable decrease of about 60% is observed in *LVM1* and *LVM4*, and an increase of about 50% is presented for *LVM2*, *LVM3*, and No-*LVM*. For the ASD index, the NRR results for the brain structure show a slight decrease only by *LVM1* with respect to the initial registration value. At the same time, an increment of about 20% is found in ASD for the rest of the *LVM*s. In the tumor, a considerable decrease (around 45%) was accomplished by *LVM1* and *LVM4*, with respect to the ASD value before registration; *LVM2*, *LVM3* and *No-LVM* presented an increment of approximately twice its initial value. Analyzing the brain contour for the DMax index, a slightly decrease is observed in *LVM1* and *LVM4* (around 20%), although *LVM2* and *LVM3* remain approximately at the same value before the NRR process, and *No-LVM* presented an increase of 23%. For the tumor, a 20% decrease is presented in *LVM1* and *LVM4* for DMax. Although a 35% increase is presented with the other two *LVM*s and *No-LVM* case. Finally, the NRR average performance for the brain structure with the DICE index was always above 0.9 for all cases, before and after the NRR process. In the tumor, DICE shows an increase after the NRR process with *LVM1* (10%) and *LVM4* (7%), and a decrease of about 15% with *LVM2*, *LVM3* and *No-LVM*. The overall evaluation in Table 7.1 shows that the NRR with *LVM1* achieved the best mean index in 75% of the cases, and the lowest variability (std) in 63%.

In addition to the accuracy indices, the Euclidean error is calculated between the tumor markers before and after the NRR process in table 2. For each deformation (Def), the mean ± std value of the distance between the eight markers around the tumor is presented for each *LVM*. In this table, we can observe a decrease in the mean error and its variability (std) for *LVM1* and *LVM4* (25%). Meanwhile, the error increased for *LVM2*, *LVM3* and *No-LVM* (roughly 50%).

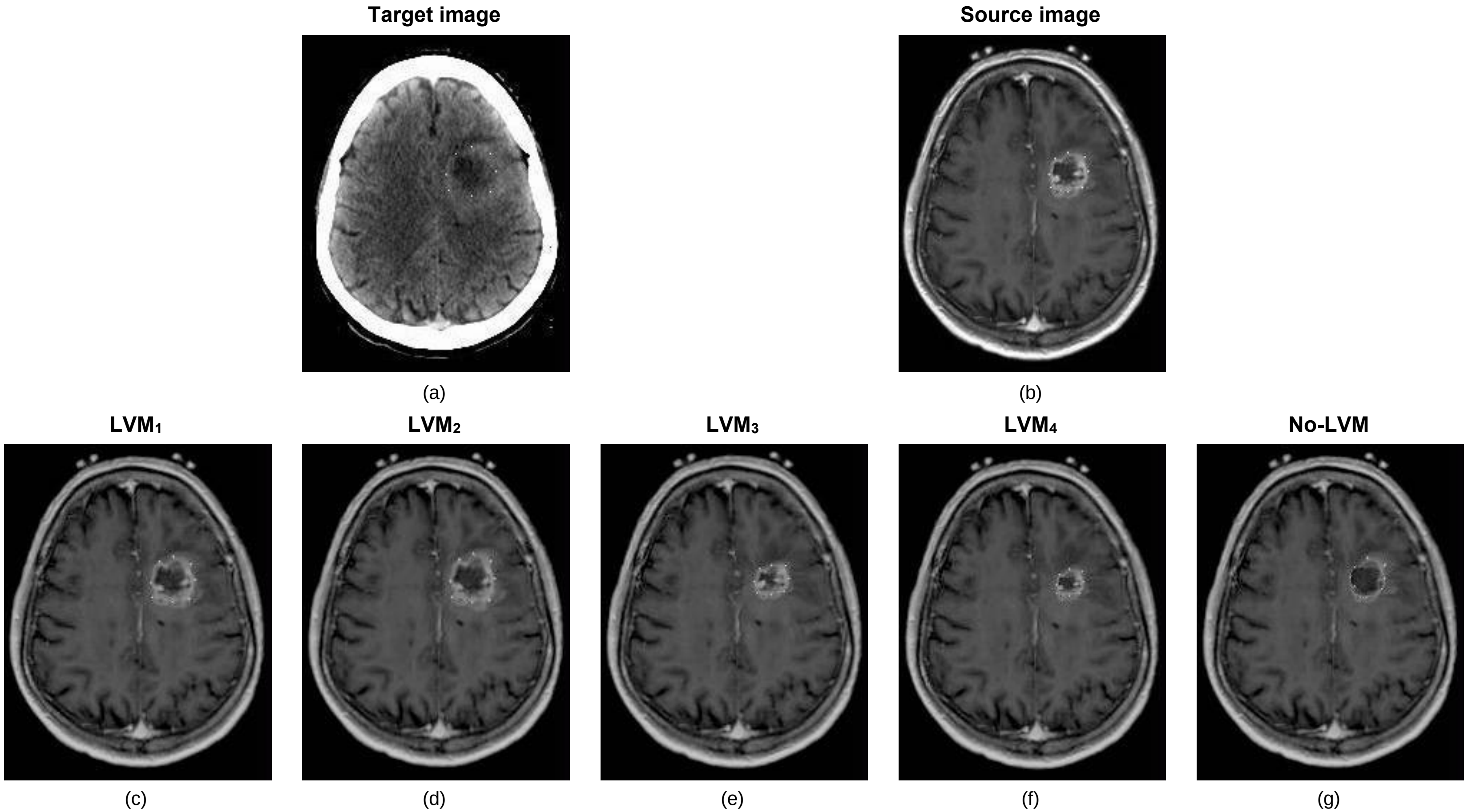

Figure 3. Example of NRR results of the synthetic dataset for the four *LVM*s and original PF+OF algorithm (*No-LVM*). (a) Target image (b) Source image. (c), (d), (e), (f) and (g), show the registration result of LVM$_1$, LVM$_2$, LVM$_3$, LVM$_4$and No-LVM, respectively.

Table 1. Mean and standard deviation of ADiff (area difference), ASD (average symmetric distance), DMax (maximum symmetric distance) and DICE (dice similarity coefficient) obtained before the registration process, with the four *LVM* (entropy, variance, and Euclidean and maximum weights between them) and with the *No-LVM* version; for the three anatomical structures of interest in the synthetic images.

Index	**Anatomical structure**	**Before registration**		**LVM$_1$**		**LVM$_2$**		**LVM$_3$**		**LVM$_4$**		**No-LVM**	
		Mean	Std. Dev.	**Mean**	Std. Dev.	**Mean**	Std. Dev.	**Mean**	Std. Dev.	**Mean**	Std. Dev.	**Mean**	Std. Dev.
ADiff(mm^2)	**Brain**	**0.005**	0.002	***0.004***	0.003	***0.005***	0.002	***0.007***	0.004	***0.004***	0.002	***0.008***	0.005
	Tumor	**0.283**	0.049	***0.100***	0.073	***0.445***	0.187	***0.432***	0.132	***0.145***	0.096	***0.328***	0.094
ASD (mm)	**Brain**	**0.340**	0.075	***0.331***	0.086	***0.466***	0.178	***0.495***	0.170	***0.415***	0.205	***0.542***	0.185
	Tumor	**2.698**	0.729	***1.427***	0.587	***4.560***	1.226	***4.284***	1.063	***1.735***	0.766	***3.992***	1.001
DMax(mm)	**Brain**	**3.549**	0.992	***2.730***	0.846	***3.413***	1.312	***3.276***	0.518	***2.867***	0.449	***4.368***	0.992
	Tumor	**6.143**	2.120	***4.778***	1.967	***8.327***	1.750	***8.371***	2.139	***4.837***	1.929	***8.600***	1.989
DICE	**Brain**	**0.995**	0.001	***0.996***	0.001	***0.994***	0.002	***0.993***	0.003	***0.995***	0.002	***0.993***	0.002
	Tumor	**0.817**	0.042	***0.906***	0.036	***0.667***	0.126	***0.693***	0.094	***0.883***	0.049	***0.729***	0.051

Table 2. Euclidean distance (mm) of the tumor markers, before and after registration for each synthetic deformation (Def).

Deformations		**Before registration**		**LVM$_1$**		**LVM$_2$**		**LVM$_3$**		**LVM$_4$**		**No-LVM**	
		Mean	std	***Mean***	std	***Mean***	std	***Mean***	std	***Mean***	std	***Mean***	Std
Image1	**Def1**	***3.695***	0.910	***1.714***	0.461	***8.019***	1.283	***6.074***	1.767	***1.675***	1.106	***5.650***	3.244
	Def2	***5.383***	1.081	***3.761***	2.799	***7.522***	2.488	***7.270***	2.146	***3.385***	1.865	***6.898***	2.778
	Def3	***4.437***	1.103	***2.061***	1.196	***8.369***	1.052	***6.919***	1.466	***2.428***	1.504	***6.303***	3.099
Image2	**Def1**	***3.571***	2.267	***3.169***	1.397	***5.540***	3.104	***5.892***	3.364	***3.530***	1.214	***5.978***	2.648
	Def2	***3.468***	2.228	***3.206***	2.384	***5.021***	2.984	***5.142***	3.012	***3.621***	2.538	***5.500***	2.205
	Def3	***6.364***	3.999	***5.400***	2.896	***8.141***	5.516	***8.367***	2.680	***5.676***	2.896	***8.476***	4.315

Clinical images

Figure 4 shows an example of the NRR results obtained by applying the *PF+LVM+OF* approach to the clinical dataset, where it is possible to visually assess the performance of the registration process for each *LVM*. In this example, the CT-Pre and MR-Post images (I_T and I_S respectively) show the tumor before and after the RT treatment, located in the center of the left hemisphere. Therefore, the visual inspection consisted in evaluate if the registration process was able to recover the deformation (shrinking) suffered by the tumor due to the RT treatment. Taking this information into account, *LVM1*, *LVM3* and *LVM4* have an acceptable performance from a clinical point of view (see Figures. 4 (h), (j) and (k)); while *LVM2* and *No-LVM* have not since they predict a change in opposite direction (see Figures. 4. (i) and (l)).

The quantitative analysis is presented in table 3, where for each performance index the mean ± std for each group of anatomical structures of interest are shown. For the brain contour, a slight decrease in ADiff is presented with respect to its initial value before NRR with the exception of *LVM4*; for the ventricles and the tumor, a more evident decrease was presented in all *LVM*s and *No-LVM* case. The results for the brain contour and ventricles show also a decrement in ASD. For DMax, a slight reduction is observed after the NRR process for the brain structure; although for the *No-LVM* case, there is an increase in this index for all anatomical structures. For the ventricles, a decrease was found with all four *LVM*s, where *LVM2* showed the largest improvement (15%). Finally, DICE shows for the brain structure a performance always above 0.9, before and after the NRR process; in the ventricles, the DICE shows a slight increase after NRR (about 8%) with all *LVM*s and *No-LVM* scenarios. Analyzing the tumor, *LVM2* and *No-LVM* did not improve ASD, DMax and DICE after the NRR process. An improvement in all four indices is found only for *LVM1*, *LVM3* and *LVM4*; being the best improvements of 40% for the ADiff, 17% for the ASD, 15% for the DMax, and 9% for the DICE, all of them by using *LVM1*.

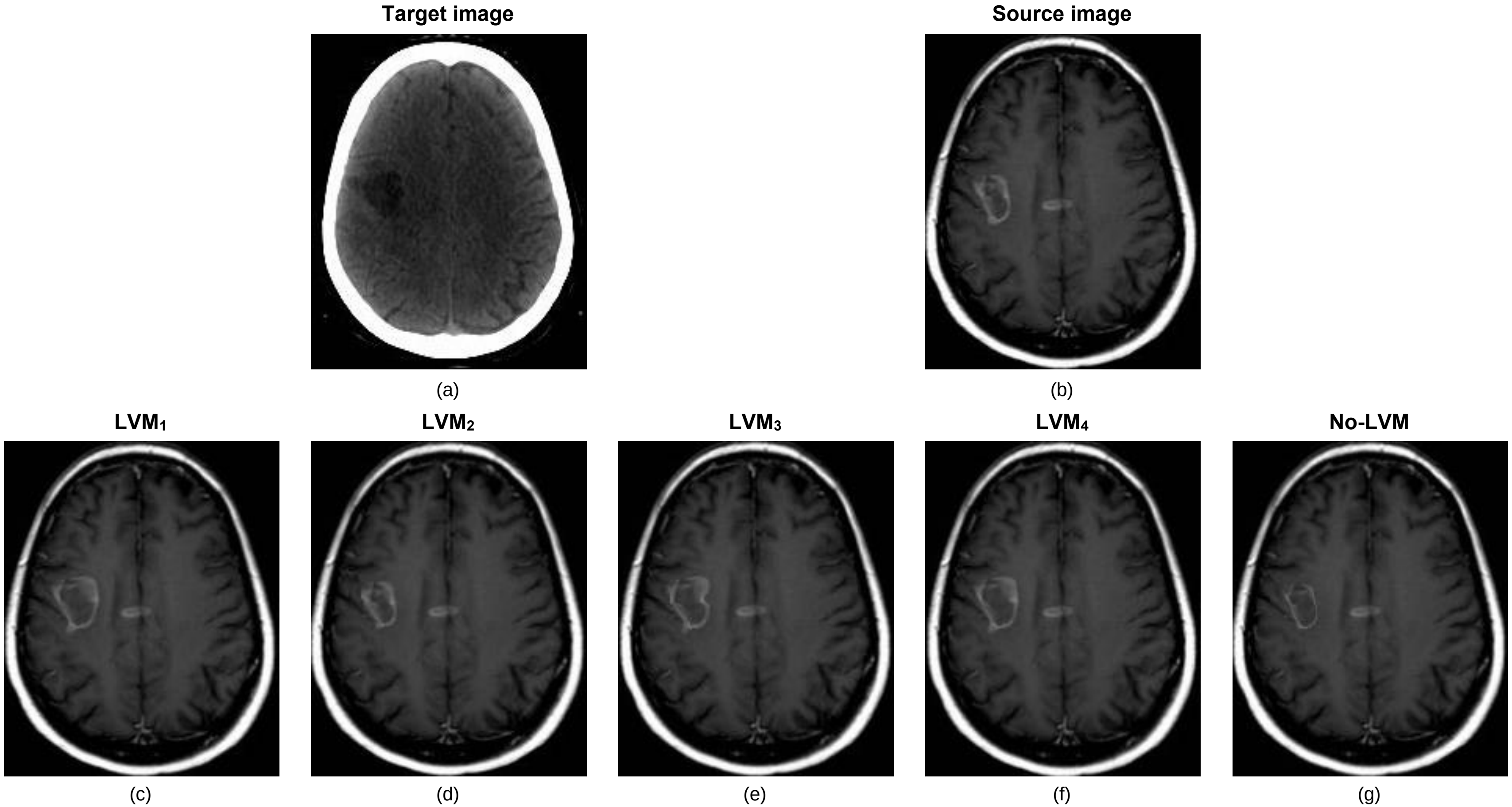

Figure 4. Registration results for the four LVMs and No-LVM version. (a) and (b) CT-Pre and MR-Post images used as target and source, respectively; (c)-(g) registered images, and (h)-(l) deformation fields after NRR.

Table 3. Mean and standard deviation of ADiff (area difference), ASD (average symmetric distance), DMax (maximum symmetric distance) and DICE (dice similarity coefficient) obtained before the registration process, with the four LVM (entropy, variance, 2-Norm and Infinity-Norm) and with the No-LVM version; for the three anatomical structures of interest.

Index	**Anatomical structure**	**Before registration**		**LVM_1**		**LVM_2**		**LVM_3**		**LVM_4**		**No-LVM**	
		Mean	Std. Dev.	Mean	Std. Dev.	Mean	Std. Dev.	Mean	Std. Dev.	Mean	Std. Dev.	Mean	Std. Dev.
ADiff(mm^2)	**Brain**	***0.012***	0.010	***0.008***	0.008	***0.010***	0.007	***0.010***	0.009	***0.013***	0.010	***0.008***	0.007
	Ventricles	***0.964***	2.163	***0.520***	0.915	***0.679***	1.973	***0.692***	2.108	***0.665***	1.084	***0.501***	0.879
	Tumor	***0.420***	0.263	***0.252***	0.365	***0.415***	0.292	***0.366***	0.310	***0.278***	0.340	***0.389***	0.350
ASD (mm)	**Brain**	***0.999***	0.235	***0.781***	0.398	***0.741***	0.289	***0.720***	0.250	***0.859***	0.326	***0.769***	0.219
	Ventricles	***2.197***	1.241	***1.891***	1.157	***1.811***	1.234	***1.829***	1.081	***1.970***	1.202	***1.868***	1.441
	Tumor	***4.265***	3.285	***3.517***	4.123	***4.669***	3.752	***4.009***	3.926	***3.590***	3.694	***4.804***	4.265
DMax(mm)	**Brain**	***4.341***	0.674	***4.013***	0.717	***4.259***	0.846	***3.964***	0.973	***4.341***	0.868	***4.586***	0.791
	Ventricles	***7.841***	6.372	***7.308***	6.599	***6.604***	5.447	***6.918***	4.875	***7.833***	6.783	***8.042***	7.424
	Tumor	***9.398***	4.046	***7.980***	4.710	***10.144***	4.843	***9.031***	5.228	***8.368***	4.560	***10.362***	5.713
DICE	**Brain**	***0.986***	0.004	***0.989***	0.006	***0.990***	0.004	***0.990***	0.004	***0.988***	0.005	***0.990***	0.003
	Ventricles	***0.608***	0.198	***0.659***	0.191	***0.662***	0.213	***0.645***	0.214	***0.656***	0.185	***0.681***	0.205
	Tumor	***0.683***	0.264	***0.746***	0.319	***0.661***	0.289	***0.710***	0.301	***0.741***	0.294	***0.652***	0.322

Discussion

Synthetic images

In the analysis of the synthetic evaluation, only the brain contour, the biggest rigid structure presented in the images, and the tumor, which is the structure that presents complex deformations, were considered as structures of interest for RT. Therefore, as expected, the values of all four accuracy indices (ADiff, DICE, ASD and DMax) calculated for all the *LVM*s and *No-LVM* at the contour of the brain did not change significantly compared to their values before NRR. For the tumor, an improvement was presented only for *LVM1* and *LVM4* in all indices, being *LVM1* the one with the largest improvement. The analysis of the Euclidean error among markers in the tumor section provided an estimation of the NRR accuracy on specific points for a structure of interest; anew, the corresponding results show positive performance only for *LVM1* and *LVM4*. However, by considering the results in [Reducindo et al., 2012], where *LVM*s were first proposed for the registration of medical images, an acceptable performance was found in all four LVMs. Moreover, the performance analysis in [Reducindo et al., 2012] was only based on the mean error of the entire vector field after applying the NRR algorithm; while in this paper, we analyze the performance of the different *LVM*s methodologies by specifically addressing the anatomical structures of clinical interest.

Clinical images

The resulting images after the NRR process show that *LVM1* (entropy) provides qualitatively and quantitatively the best results on the set of images used for the evaluation, followed by *LVM4* (maximum weight between entropy and variance), appropriately aligning the anatomical structures in MR-Post with CT-Pre. Although *LVM2* and *LVM3* (variance and Euclidean weight between entropy and variance) achieve an adequate alignment for some structures of interest, these metrics generated anatomically inconsistent deformations, and changes in the textures of tissues in the registered images. The inconsistent deformations obtained after NRR by *LVM2* might be caused by highly textured in MR versus low contrast areas in CT, as in several brain regions, where the values obtained by computing local variance are constant due to the low variability of the intensities in these regions. This phenomenon becomes similar to estimate the OF between two constant-intensity areas, where any displacement in any direction keeps unchanged the cost function. In the same way, within an homogeneous area, there is high probability of obtaining values of variance and entropy for two different locations with similar magnitudes, generating an identical problem for *LVM3* (Euclidean weight). These effects explain the inconsistent deformations generated by *LVM2* and *LVM3*, which do not occur in *LVM1*, because in highly textured areas, the entropy values are very different from the rest, due to the high uncertainty in the intensities of these regions. Images 5.(a) and (b) show the tumor for MR-Pre and CT-Pre respectively, where it is possible to observe the lack of contrast for the tumor, which makes difficult the registration of this structure with the MR-Post (figure 5 (c)), by using any LVM. On the other hand, images 5 (d) and (e) show an example of good contrast, where it is easy to distinguish the tumor in both CT and MR images, thereby facilitating the registration of this structure with MR-Post (figure 5 (f)). Thus, an acceptable difference can be considered as the suitable contrast in the CT-Pre that enables to distinguish the tumor from the rest of the brain in the CT.

Lack of contrast for the tumor in CT-Pre

(a) MR-Pre (b) CT-Pre (c) MR-Post

Good contrast for the tumor in CT-Pre

(d) MR-Pre (e) CT-Pre (f) MR-Post

Figure 5. Examples of good and lack of contrast of the tumor in the CT-Pre. Images (a) and (b) show the tumor for MR-Pre and CT-Pre respectively, where it is easy to see in CT-Pre that the tumor has poor contrast, which makes difficult the NRR of this structure with the MR-Post, shown in (c), by using any LVM. Images (d) and (e) show the tumor for MR-Pre and CT-Pre respectively, where is possible to see a good contrast of the tumor in CT-Pre, thereby facilitating the registration of this structure with the MR-Post, shown in (f).

In fact, the quantitative analysis on the tumor shows that the best results for the NRR algorithm were obtained by using *LVM1* and *LVM4*, despite some problems with the contrast in the CT-Pre images. Moreover, the *No- LVM* approach does not provide good results to estimate the tumor deformation, because the tissue intensities at each modality (CT and MR) are very different. Contrarily, the *No-LVM* approach gave the best results in terms of ADiff and DICE in the ventricles and the brain contour (along with *LVM1*) and also presented positive results in the ventricles for the ASD index (see Table 3). This behavior could be related to the similarity of intensities in the ventricles, for both CT and MR.

The positive results found with the No-LVM implementation follow the performance shown in [Arce-Santana et al., 2010; Mejia-Rodriguez et al., 2011], where it is stated that the use of the PF+OF method is a valuable tool for complex NRR problems. In the meantime, the negative results support the disadvantage of this methodology for multimodal cases, reinforcing the motivation for using *LVM*s to achieve a multimodal registration that does not parameterize the elastic deformation space, in contrast to the majority of the methods reported in the literature. Furthermore, a parameterization of the deformation space increases the computational cost because the optimization process used in these methods are typically nonlinear [Xuan et al., 2006; Serifovic-Trbalic et al., 2009; Klein et al., 2009]. These two problems are solved with the proposed PF+LVM+OF technique, since each pixel can move independently, thus increasing the manifoldness of deformations that can be reproduced. Also, the OF estimation process is formulated as a quadratic optimization over a convex surface, and its global solution is computed by a system of linear equations, which ensures a low computational cost.

Making a comparison between the four *LVM*s and the *No-LVM* implementation (see Tables 1, 2 and 3), it is possible to see a consistent advantage of *LVM1* (entropy) over the other *LVM*s and *No-LVM* approach in mean performance, and even in some cases, with less variability. This idea suggests that the local entropy is the best performing *LVM* under a quantitative analysis of anatomical structures of interest for RT brain images. Furthermore, the results found in this work suggest that the *PF+LVM+OF* algorithm, if extended to a 3D version, could be useful in RT for some important tasks, such as the monitoring of medical treatment.

Conclusion

In this work, local intensity transformations are suggested to perform a multimodal NRR based on PF and iterative OF. These transformations map the target and source images into a space where the multimodal property is overcame, such that an efficient OF solution can be pursued. The evaluation of the proposal was based on CT and MR brain images deformed synthetically and on real clinical cases. The results showed that the local entropy is the LVM with the best performance, both qualitatively and quantitatively, by analyzing the anatomical structures of interest in RT (brain contour, tumor and ventricles). Therefore, our NRR proposal could be considered as a new option of medical image registration for RT applications.

Appendix C

Registration Accuracy Based on Mesh Data Structures

The analysis of anatomical structures of interest used in this work to evaluate the accuracy of registration methods is also of great importance in a clinical context. For example the analysis of anatomical modifications occurring during RT treatments is useful to identify potential predictors of toxicity in organs at risk (OAR) and to design optimized adaptive treatment plans. To have a better perspective of the distortions that occur, the mesh data-structure is one of the most used techniques in RT for rendering 3D structures of interest. However, although meshing is widely used, the analysis is usually carried out by extracting quantitative metrics from a set of 2D binary images whose contours define a 3D surface, as it was performed in this work; in this way a coarser representation of the structure surfaces is obtained. In this appendix, a mesh-based approach is proposed to improve the analysis of 3D anatomical structures in RT, by calculating directly over the meshes the standard indices previously used. Mesh surfaces corresponding to the right and left parotid glands, from a set of Megavoltage CT (MVCT) images from patients treated for head-and-neck cancer (HNC) were constructed from manual contour delineations. This approach is compared with the standard binary image approach in order to evaluate if the introduction of this more accurate 3D representation results in differences between both strategies of structure analysis; the set of binary images used for the classical analysis was also generated using the same contour delineations. Results suggest that the proposed mesh approach could represent a useful tool in RT for the analysis structures of interest, being able to provide a finer 3D shape representation, and could have more relevance when anatomical structures with more complex or deformable shapes, like the lungs, are considered. The present chapter is based on the article :

Aldo R. Mejia-Rodriguez , Elisa Scalco, Daniele Tresoldi, Anna M. Bianchi, Edgar R. Arce-Santana, Martin O. Mendez, Giovanna Rizzo. *"A Mesh-Based Approach for the 3D Analysis of Anatomical Structures of Interest in Radiotherapy"*. Proceedings of the 34th Annual International Conference of the IEEE Engineering in Medicine and Biology Society; 2012: 6555 - 6558.

34th Annual International Conference of the IEEE EMBS
San Diego, California USA, 28 August - 1 September, 2012

A Mesh-Based Approach for the 3D Analysis of Anatomical Structures of Interest in Radiotherapy

Aldo R. Mejia-Rodriguez, Elisa Scalco, Daniele Tresoldi, Anna M. Bianchi, Edgar R. Arce-Santana,
Martin O. Mendez, Giovanna Rizzo

Abstract— **In this paper a method based on mesh surfaces approximations for the 3D analysis of anatomical structures in Radiotherapy (RT) is presented. Parotid glands meshes constructed from Megavoltage CT (MVCT) images were studied in terms of volume, distance between center of mass (distCOM) of the right and left parotids, dice similarity coefficient (DICE), maximum distance between meshes (DMax) and the average symmetric distance (ASD). A comparison with the standard binary images approach was performed. While absence of significant differences in terms of volume, DistCOM and DICE indices suggests that both approaches are comparable, the fact that the ASD showed significant difference (p=0.002) and the DMax was almost significant (p=0.053) suggests that the mesh approach should be adopted to provide accurate comparison between 3D anatomical structures of interest in RT.**

I. INTRODUCTION

THE analysis of anatomical structures of interest is a relevant task in the medical field. For example in Radiotherapy (RT), patients undergoing a head-and-neck cancer (HNC) treatment are known to experience significant decrease in the volume of the parotid glands and their migration toward the midline of the patient with a distance change of a few millimeters. Due to these anatomical modifications the parotids can receive a total dose significantly higher than the planned one. In this context the importance of the analysis of the anatomical modifications occurring during RT treatments is to both identify potential predictors of toxicity and design optimized adaptive treatment plans [1].

To have a better perspective of the distortions that occur in structures of interest, different techniques to represent structures in 3D have been implemented [2, 3]. The mesh data-structure is one of the most used techniques for rendering 3D objects and it is defined as a collection of vertices (points positioned in a virtual space), edges (a connection between two vertices) and faces (a closed set of edges) that defines the shape of a polyhedral object. The faces could form polygons of any type (quadrilaterals, concaves or convexes complex polygons) but triangular polygons are commonly used since this simplifies rendering [3].

Although meshing is widely used for rendering 3D geometrics, in RT, analysis of anatomical structures of interest is usually carried out by extracting quantitative measurements from a set of 2D binary images whose contours define a 3D surface [4, 5]. In this way a coarser representation of the structure surfaces is obtained [2].

In this paper, we propose a mesh-based approach to improve the analysis of 3D anatomical structures in RT. This approach is compared with the standard binary image approach in order to evaluate if the introduction of this more accurate 3D structure representation results in differences in structure analysis.

II. METHODS

A. *Analysis of structures of interest by meshes*

Analysis of the 3D anatomical structures by meshes proposed in this paper consists in the calculation of nine quantitative standard indices. The indices could be divided into two categories, 1) indices that give spatial and geometrical information of an individual mesh: coordinates of the baricenter, surface area and volume; and 2) indices that make a comparison between two meshes: Euclidean distance between baricenters, surface area difference, volume difference, dice similarity coefficient (DICE) [1], maximum distance between meshes (DMax) and average symmetric distance (ASD) [1].

DICE index is a metric of the overlap between 2 surfaces ranging from 0 (no spatial overlap) to 1 (complete overlap). DMax index calculates the maximum distance between two surfaces and gives an idea of the worst local distance mismatch. ASD index is defined as the average Euclidean distance between two surfaces, which is 0 for a perfect match.

---

*A. R. Mejia-Rodriguez is with Institute of Molecular Bioimaging and Physiology (IBFM)-CNR, Milan, Italy and Bioengineering Department, Politecnico di Milano, Milan, Italy. Author is supported by CONACyT studentship (CVU/Becario): 217232/213579 for PhD studies (e-mail: armero83@gmail.com)

E. Scalco is with Institute of Molecular Bioimaging and Physiology (IBFM)-CNR, Milan, Italy

D. Tresoldi is with Institute of Molecular Bioimaging and Physiology (IBFM)-CNR, Milan, Italy and Bioengineering Department, Politecnico di Milano, Milan, Italy.

A.M. Bianchi is with Bioengineering Department Politecnico di Milano, Milan, Italy.

E. R. Roman-Arce is with Fac. de Ciencias, UASLP, San Luis Potosi, Mexico.

M.O. Mendez-Garcia is with Fac. de Ciencias, UASLP, San Luis Potosi, Mexico.

G. Rizzo is with Institute of Molecular Bioimaging and Physiology (IBFM)-CNR, Milan, Italy.

978-1-4577-1787-1/12/$26.00 ©2012 IEEE

For the calculations of the meshes and the set of indices the standard libraries included in the Visualization Toolkit (VTK) package were used, particularly the VTK package implemented for its use in Python [6].

B. Boolean operations on meshes

For DICE, DMax and ASD calculations, a set of classes that enable computation of boolean operations on meshes were used [7]. Boolean operations over meshes can be computed using the signed distance field (distance from a point *x* in one mesh to the nearest point on the surface defined by another mesh). The sign of the distance field corresponds to whether a point is inside (negative), outside (positive), or on (zero) the other mesh. In this context, the boolean operations of union, intersection and difference were defined as:

- Union: set of cells in each mesh such that the distance from each cell point to the other mesh is ≥ 0.
- Intersection: set of cells in each mesh such that the distance from each cell point to the other mesh is ≤ 0.
- Difference: set of cells of the mesh A (M_A) whose points are a non-negative distance from mesh B (M_B) combined with the cells of M_B whose points are a non positive distance from M_A.

Taking these assumptions into account and given two meshes A and B, the DICE, ASD and DMax indices were calculated as:

$$DICE = 2\frac{V_A \bigcap V_B}{V_A + V_B} \tag{1}$$

$$ASD = \frac{1}{M_A + M_B}\left(\sum_{p_B \in M_A} d(p_A, M_B) + \sum_{p_A \in M_B} d(p_B, M_A)\right) \tag{2}$$

$$DMax = \max\left\{\max_{p_A \in M_A} d(p_A, M_B), \max_{p_B \in M_B} d(p_B, M_A)\right\} \tag{3}$$

where V_A and V_B are the sets of cells within A and B, respectively, $d(p_A, M_B)$ and $d(p_B, M_A)$ indicate the shortest distance between an arbitrary point to A or B, respectively.

The same equations can also be used to define correspondent indices for the standard binary image analysis, where, instead of meshes, A and B refer to binary image contours.

Fig. 1 shows an example of two meshes to be compared and the respective meshes generated by the boolean operations.

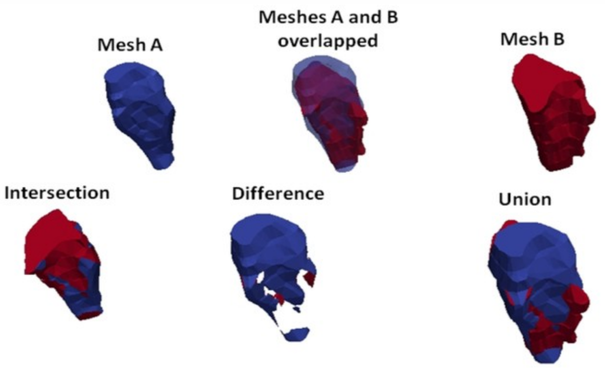

Fig. 1 Example of 3D representation of two meshes: A and B, with their respective boolean operations meshes.

C. Comparison between mesh and binary image approaches for the analysis of 3D structures

Mesh analysis was applied to a set of Megavoltage CT (MVCT) images from 10 patients treated for HNC with Helical Tomotheraphy analyzed in [1] with the standard analysis based on binary images. Triangular mesh surfaces corresponding to the right and left parotids were constructed from the manual contour delineation by three different expert observers in radiological images using the power crust method [8]; the set of binary images used for the parotid analysis studied in [1] were also generated using these manual contour delineations.

A comparison between measurements calculated from binary images in [1] and measurements computed from meshes was made in terms of parotid volumes, distance between right and left parotids center of mass (DistCOM), DICE, ASD and DMax indices. Wilcoxon signed rank test ($p<0.05$) between both approaches was used to assess the comparison.

III. RESULTS

Table I presents the results for the calculation of the volume of the parotid glands from both meshes and binary images. For each patient mean ± std values of the right parotid (*Par R*) and left parotid (*Par L*) are presented. The comparison between mesh and binary images volume values was assessed for each expert observer (Exp). The mean ±std values found for Exp1 were 16.759±5.132 cm^3 vs. 16.760±5.129 cm^3; Exp2 16.377±5.023 cm^3 vs. 16.405±5.037 cm^3; and Exp3 18.304±5.107 cm^3 vs. 18.166±5.044 cm^3, for mesh approach and binary image approach respectively. No significant differences were found (Exp1 p =0.668; Exp2 p=0.861 ; Exp3 p=0.538).

Table II shows the comparison for DistCOM of the right and left parotids. The mean ± std values found for Exp1 were 110.55±8.64 mm vs. 111.44±8.44 mm; Exp2 109.97±8.52 mm vs. 111.03±8.55 mm; and Exp3 109.55±7.88mm vs. 110.40±7.68 mm. No significant differences were found (Exp1 p = 0.623; Exp2 p=0.677 ; Exp3 p=0.677).

Table III presents the results for DICE, DMax and ASD indices; for each patient the mean ± std value of all possible pairs comparisons between the three expert observers are presented. The mean ± std values of the mesh and binary images estimations respectively for each index were: DICE 0.796±0.043 vs. 0.812±0.028; DMax 9.014±2.052 mm vs. 9.617±1.840 mm; and ASD 1.157±0.429 mm vs. 1.581±0.250 mm. No significant differences were found for the DICE (p=0.179) and DMax (p=0.053), while ASD shows significant differences (p=0.002) between mesh and binary image approaches.

IV. DISCUSSION

Volume and DistCOM give geometrical and spatial information of a structure of interest, in this case parotid glands from patients treated with RT. The absence of significant differences between the mesh-based analysis and the approach based on sets of binary images suggests that both methodologies are suitable to provide quantitative anatomical information in parotid glands. DICE, DMax and ASD allow comparisons between two structures; in this case allowed to compare the parotid glands 3D representations constructed from the manual contours delineated by three different expert observers in RT. Results showed that the two approaches studied in this work are comparable in terms of DICE and DMax, but showed significant difference (21%) when ASD is considered.

Volume, DistCOM and DICE indices give spatial global information about the structures analyzed, therefore these indices are less susceptible to the variations presented in the mesh-based rendering and the representation using binary images; hence, the absence of significance between the two approaches was expected. On the other hand, ASD and DMax indices are more sensitive to these variations because they give information about the mean mismatch and the worst mismatch case between 2 structures respectively. The fact that the ASD showed significant difference (p=0.002) and the DMax was almost significant (p=0.053) suggests that mesh-based analysis presented in this paper should be preferable to obtain geometrical information of 3D structures. Besides, an additional advantage related to the use of a mesh approach is that it facilitates modeling of complex deformations, such as the ones that could be found in RT.

V. CONCLUSION

The mesh approach presented in this work could represent a useful tool in RT to compare anatomical structures of interest, being able to provide a finer 3D shape representation. This approach could have more relevance when anatomical structures with more complex or deformable shapes, like the lungs, are considered.

TABLE I. VOLUME COMPARISON BETWEEN MESH AND BINARY IMAGES APPROACHES. VALUES WERE CALCULATED FOR RIGHT (R) AND LEFT (L) PAROTIDS FOR EACH PATIENT (PAT)

VOLUME (cm^3)

	Exp1		**Exp2**		**Exp3**	
	Mesh	**Binary**	**Mesh**	**Binary**	**Mesh**	**Binary**
Pat1 R	18.540	18.540	19.836	20.190	23.340	23.340
Pat1 L	21.500	21.500	20.650	20.650	22.434	22.430
Pat2 R	17.693	17.690	18.343	18.340	19.626	19.630
Pat2 L	19.131	19.130	16.799	17.020	20.674	18.500
Pat3 R	17.566	17.570	16.691	16.690	19.310	19.310
Pat3 L	10.225	10.260	15.005	15.000	13.630	13.630
Pat4 R	17.350	17.350	21.825	21.820	20.273	20.270
Pat4 L	17.282	17.280	18.019	18.020	17.023	17.020
Pat5 R	22.938	22.940	24.334	24.330	22.975	22.980
Pat5 L	21.703	21.700	17.327	17.330	22.832	22.830
Pat6 R	24.590	24.590	20.068	20.070	28.834	28.830
Pat6 L	26.204	26.200	21.145	21.140	19.952	19.950
Pat7 R	14.082	14.080	13.341	13.340	15.121	15.180
Pat7 L	17.724	17.720	15.875	15.880	17.878	17.880
Pat8 R	7.896	7.900	5.399	5.400	10.666	10.670
Pat8 L	10.393	10.390	9.104	9.050	11.167	11.170
Pat9 R	11.463	11.460	12.111	12.110	11.002	11.000
Pat9 L	10.738	10.740	7.164	7.210	10.658	10.660
Pat10 R	15.698	15.700	20.629	20.630	23.076	22.440
Pat10 L	12.460	12.460	13.880	13.880	15.601	15.600
MEAN	**16.759**	**16.760**	**16.377**	**16.405**	**18.304**	**18.166**
STD	**5.132**	**5.129**	**5.023**	**5.037**	**5.107**	**5.044**

No significant differences were found with the Wilcoxon signed rank test ($p<0.05$).

TABLE II. DISTCOM COMPARISON BETWEEN MESH AND BINARY IMAGES APPROACHES. VALUES WERE CALCULATED FOR RIGHT (R) AND LEFT (L) PAROTIDS FOR EACH PATIENT (PAT)

DistCOM_ (mm)

	Exp1		**Exp2**		**Exp3**	
	Mesh	**Binary**	**Mesh**	**Binary**	**Mesh**	**Binary**
Pat1	115.77	116.53	115.66	116.16	113.17	114.45
Pat2	106.06	107.20	106.68	107.53	106.19	107.10
Pat3	112.78	113.18	114.27	115.31	115.24	115.57
Pat4	113.11	113.39	109.49	109.57	110.42	109.29
Pat5	121.49	122.47	121.81	123.82	119.16	120.48
Pat6	122.22	122.83	119.23	120.76	117.42	118.37
Pat7	98.09	99.08	95.56	97.79	96.10	98.56
Pat8	99.09	100.19	99.45	100.35	98.31	99.52
Pat9	102.90	104.53	104.09	104.70	105.96	105.20
Pat10	113.98	114.97	113.41	114.35	113.54	115.42
MEAN	**110.55**	**111.44**	**109.97**	**111.03**	**109.55**	**110.40**
STD	**8.64**	**8.44**	**8.52**	**8.55**	**7.80**	**7.68**

No significant differences were found with the Wilcoxon signed rank test ($p<0.05$).

TABLE III.

DICE, DMAX AND ASD COMPARISONS BETWEEN MESH AND BINARY IMAGES APPROACHES. VALUES WERE CALCULATED FOR RIGHT (R) AND LEFT (L) PAROTIDS FOR EACH PATIENT (PAT).

	DICE				**DMax (mm)**				**ASD (mm)**			
	Mesh		**Binary Im.**		**Mesh**		**Binary Im.**		**Mesh**		**Binary Im.**	
	Mean	**std**	**Mean**	**Std**	**Mean**	**std**	**Mean**	**std**	**Mean**	**std**	**Mean**	**std**
Pat1 R	0.790	0.018	0.788	0.019	10.612	0.708	9.844	0.450	1.208	0.224	1.895	0.053
Pat1 L	0.822	0.009	0.809	0.025	9.618	0.751	13.834	2.672	1.102	0.082	1.832	0.209
Pat2 R	0.840	0.018	0.836	0.007	6.760	2.382	8.469	1.000	0.570	0.209	1.326	0.083
Pat2 L	0.785	0.019	0.828	0.031	10.280	1.630	9.199	1.455	0.960	0.342	1.457	0.296
Pat3 R	0.769	0.063	0.771	0.040	8.464	1.161	8.859	1.499	0.981	0.465	1.941	0.458
Pat3 L	0.786	0.028	0.808	0.064	7.699	1.404	8.113	2.114	1.393	0.461	1.490	0.481
Pat4 R	0.767	0.054	0.774	0.026	11.374	3.690	11.770	1.603	1.503	0.457	1.881	0.238
Pat4 L	0.809	0.033	0.793	0.020	8.792	0.252	10.324	1.138	0.901	0.212	1.589	0.129
Pat5 R	0.843	0.001	0.838	0.011	6.731	1.017	8.117	0.814	0.729	0.077	1.473	0.084
Pat5 L	0.788	0.028	0.812	0.017	8.194	1.276	10.301	1.927	0.940	0.323	1.646	0.110
Pat6 R	0.808	0.021	0.855	0.028	10.900	1.986	8.949	3.859	0.989	0.848	1.434	0.305
Pat6 L	0.841	0.441	0.827	0.029	7.992	1.882	9.013	0.825	1.695	0.930	1.613	0.315
Pat7 R	0.730	0.044	0.786	0.028	8.786	1.892	10.983	0.645	1.350	0.585	1.721	0.220
Pat7 L	0.825	0.034	0.813	0.032	7.789	0.825	8.103	0.849	0.886	0.264	1.567	0.266
Pat8 R	0.703	0.104	0.824	0.053	13.578	4.264	6.548	2.908	2.364	0.583	1.391	0.473
Pat8 L	0.837	0.037	0.825	0.027	7.053	1.162	8.231	3.042	1.001	0.299	1.226	0.176
Pat9 R	0.874	0.042	0.878	0.024	6.483	1.863	9.436	3.206	0.625	0.273	1.028	0.207
Pat9 L	0.748	0.069	0.817	0.044	7.359	0.947	8.024	2.011	1.192	0.442	1.422	0.321
Pat10 R	0.753	0.044	0.791	0.026	13.115	3.069	13.327	2.958	1.768	0.229	1.953	0.278
Pat10 L	0.803	0.019	0.771	0.011	8.707	0.448	10.893	0.722	0.979	0.201	1.743	0.126
MEAN	**0.796**		**0.812**		**9.014**		**9.617**		***1.157**		**1.581**	
STD	**0.043**		**0.028**		**2.052**		**1.840**		**0.429**		**0.250**	

* p=0.002, ASD presented significant difference with the Wilcoxon signed rank test

REFERENCES

[1] E. Faggiano, C. Fiorino, E. Scalco, S. Broggi, M. Cattaneo, E. Maggiulli, I. Dell'Oca, N. Di Muzio, R. Calandrino,G. Rizzo, “An automatic contour propagation method to follow parotid gland deformation during head-and-neck cancer tomotherapy”, *Phys Med Biol.* 2011 Feb 7;56(3):775-91. Epub 2011 Jan 14.

[2] A. M. Alyassin, J. L. Lancaster, J. Hunter Downs III, and P. T. Fox, “Evaluation of new algorithms for the interactive measurement of surface area and volume”, *Med. Phys. 21*, 741, 1994.

[3] C. Smith. “ On Vertex-Vertex Systems and their Use in Geometric and Biological Modelling”. Ph.D. Dissertation. University of Calgary, Calgary, Alta., Canada, 2006.

[4] R. Allozi, X.A. Li, J. White, A. Apte, A. Tai, J.M. Michalski, W.R. Bosch, I.E. Naqa, “Tools for consensus analysis of experts’ contours for radiotherapy structure definitions”, *Radiotherapy and Oncology*, Volume 97, Issue 3, December 2010, Pages 572-578.

[5] W.Y. Song, B. Chiu, G.S. Bauman, M. Lock, G. Rodrigues, R. Ash, C. Lewis, A. Fenster, J.J. Battista, J. Van Dyk, “Prostate contouring uncertainty in megavoltage computed tomography images acquired with a helical tomotherapy unit during image-guided radiation therapy”, *Int J Radiat Oncol Biol Phys*. 2006 Jun 1;65(2):595-607.

[6] W. Schroeder, K. Martin, B. Lorensen 2002 *The Visualization Toolkit 2nd edn* (Upper Saddle River, NJ: Prentice-Hall).

[7] C. Quammen, C. Weigle, R. M. Taylor II, “Boolean Operations on Surfaces in VTK Without External Libraries” VTK Journal, May 2011.

[8] N. Amenta, S. Choi, R. K. Kolluri, “The power crust, unions of balls, and the medial axis transform”, *Computational Geometry*, Volume 19, Issues 2–3, July 2001, Pages 127-153.

[9] E. Scalco, E. Faggiano, S. Liberini, C. Fiorino, E. Maggiulli, S. Broggi, G. M. Cattaneo, R. Calandrino, G. Rizzo, “Validation of elastic registration to study parotid deformation in head and neck Tomotherapy”, *Radiotherapy & Oncology*, 2011. 99, Supplement 1, p S339.

References

- Arce-Santana E.R, Campos-Delgado D U, Alba A. A non-rigid multimodal image registration method based on particle filter and optical flow. Advances in Visual Computing Lecture Notes in Computer Science. (6453) 35-44, 2010.
- Arce-Santana ER, Campos-Delgado D U., Alba A., Image registration guided by particle filter. Advances in Visual Computing, Lecture Notes in Computer Science, (5875) 554–563, 2009.
- Arce-Santana ER, Campos-Delgado DU, Alba A. Affine image registration guided by particle filter. IET Image Processing. 6(5): 455–462, 2012.
- Arulampalam MS, Maskell S, Gordon N, Clapp T. A tutorial on particle filters for online nonlinear/non-gaussian bayesian tracking. IEEE Transactions on Signal Processing. 50(2): 174–188, 2002.
- Avants, B B, Epstein C L, Grossman M, Gee, J C. Symmetric diffeomorphic image registration with cross-correlation: Evaluating automated labeling of elderly and neurodegenerative brain. Med Image Anal. 12 (1), 26–41, 2008
- Balter JM, Ten Haken RK, Lawrence TS, Lam KL, Robertson JM. Uncertainties in CT-based radiation therapy treatment planning associated with patient breathing. Int J Radiat Oncol Biol Phys. 36(1):167-74, 1996.
- Barrett, R.; Berry, M.; Chan, T. F.; Demmel, J.; Donato, J.; Dongarra, J.; Eijkhout, V.; Pozo, R.; Romine, C.; and van der Vorst, H. Templates for the Solution of Linear Systems: Building Blocks for Iterative Methods, 2nd ed. Philadelphia, PA: SIAM, 1994
- Beg M F, Miller M I, Trouvé A, Younes L. Computing large deformation metric mappings via geodesic flows of diffeomorphisms. Int. J. Comput. Vis. 61 (2), 139–157, 2005.
- Bergman N.: Recursive Bayesian estimation: Navigation and tracking applications. Ph.D. dissertation. Linkoeping University, Linkoeping, Sweden, 1999.
- Bin L, Lianfang T, Shanxing O. Rapid Multimodal Medical Image Registration and Fusion in 3D Conformal Radiotherapy Treatment Planning. Proceedings of the International Conference on Bioinformatics and Biomedical Engineering; 2010: 1–5.

- Bookstein, Fred L., "Principal warps: thin-plate splines and the decomposition of deformations," Pattern Analysis and Machine Intelligence, IEEE Transactions on, vol.11, no.6, pp.567,585, Jun 1989.
- Brock KK, Dawson LA, Sharpe MB, Jaffray DA. Application of a Novel Deformable Image Registration Technique to Facilitate Classification, Tracking and Targeting of Tumor and Normal Tissue. Int J Radiat Oncol Biol Phys, 64(4): 1245-54, 2006.
- Brock KK, Sharpe MB, Dawson LA, Kim SM, Jaffray DA. Accuracy of finite element model-based multi-organ deformable image registration. Med Phys. 2005 Jun;32(6):1647-59.
- Brock, K K. Image registration in intensity-modulated, image-guided and stereotactic body radiation therapy. Front Radiat Ther Oncol. 40:94-115, 2007.
- Bruhn A, Weickert J, Feddern C, Kohlberger T, Schnörr C. Real-Time Optic Flow Computation with Variational Methods. Computer Analysis of Images and Patterns Lecture Notes in Computer Science 2756:222-229, 2003.
- Castadot P, Lee JA, Parraga A, Geets X, Macq B, Grégoire V. Comparison of 12 deformable registration strategies in adaptive radiation therapy for the treatment of head and neck tumors. Radiother Oncol. 89(1):1-12, 2008.
- Castillo R, Castillo E, Guerra R, Johnson VE, McPhail T, Garg AK, Guerrero T. A framework for evaluation of deformable image registration spatial accuracy using large landmark point sets. Phys Med Biol. 54(7):1849-70, 2009.
- Chui H, Rangarajan A, A New Point Matching Algorithm for Non-Rigid Registration. Computer Vision and Image Understanding 89:114–141, 2003.
- Crum W, HartkensT, and Hill D. Non-rigid image registration: Theory and practice. Br. J. Radiol., vol. 77, pp. S140–S153, 2004.
- Das A, Bhattacharya M. Affine-based registration of CT and MR modality images of human brain using multi resolution approaches: comparative study on genetic algorithm and particle swarm optimization. Neural Computing and Applications. 20(2): 223–237, 2010.
- Dawson LA, Brock KK, Kazanjian S, Fitch D, McGinn CJ, Lawrence TS, Ten Haken RK, Balter J. The reproducibility of organ position using active breathing control (ABC) during liver radiotherapy. Int J Radiat Oncol Biol Phys. 51(5):1410-21, 2001.
- Dice LR. Measures of the amount of ecologic association between species. Ecology. 26:297–302, 1945.
- Dobbs, J and Barrett, A. *Practical radiotherapy planning.* Hodder Education, 2009.
- Doucet A, De Fraitas N. Sequantial Monte Carlo methods in practice. Springer, 2001.

- Doucet A. On sequential simulation-based methods for Bayesian filtering. Univ. Cambridge. Information Engineering Division, 1998.
- Duma MN, Kampfer S, Wilkens J J, Schuster T, Molls M and Geinitz H 2010 Comparative analysis of an image-guided versus a non-image-guided setup approach in terms of delivered dose to the parotid glands in head-and-neck cancer IMRT *Int. J. Radiat. Oncol. Biol. Phys.* 77 1266–73.
- Ecabert O, Peters J, Walker MJ, Ivanc T, Lorenz C, von Berg J, Lessick J, Vembar M, Weese J. Segmentation of the heart and great vessels in CT images using a model-based adaptation framework. Med Image Anal. 15(6):863-76, 2011.
- Faggiano E, Cattaneo GM, Ciavarro C, Dell'Oca I, Persano D, Calandrino R, Rizzo G. Validation of an elastic registration technique to estimate anatomical lung modification in non-small-cell lung cancer tomotherapy. Radiat Oncol. 6:31, 2011-a.
- Faggiano E, Fiorino C, Scalco E, Broggi S, Cattaneo M, Maggiulli E, Dell'Oca I, Di Muzio N, Calandrino R, Rizzo G. An automatic contour propagation method to follow parotid gland deformation during head-and-neck cancer tomotherapy. Phys Med Biol. 56(3):775-91, 2011-b.
- Fiorino C, Dell'Oca I, Pierelli A, Broggi S, De Martin E, Di Muzio N, Longobardi B, Fazio F, Calandrino R. Significant improvement in normal tissue sparing and target coverage for head and neck cancer by means of helical tomotherapy. Radiother Oncol. 2006 Mar;78(3):276-82.
- Fornefett M, Rohr K, Stiehl HS. Radial basis functions with compact support for elastic registration of medical images. Image Vision Comput. 19(1–2):87-96, 2001.
- Fox J, Ford E, Redmond K, Zhou J, Wong J, Song DY. Quantification of Tumor Volume Changes during Radiotherapy for Non-Small-Cell Lung Cancer. Int J Radiat Oncol Biol Phys. 74(2):341-348, 2009.
- Gonzalez RC, Woods RE,Eddins SL. Digital Image Processing Using MATLAB. Gatesmark Publishing; 2009.
- Guerrero T, Sanders K, Castillo E, et al. Dynamic ventilation imaging from four-dimensional computed tomography. Phys Med Biol. 51(4):777–91, 2006.
- Guimond A, Roche A, Ayache N andMeunier J 2001 Three-dimensional multimodal brain warping using the demons algorithm and adaptive intensity corrections IEEE Trans. Med. Imaging 20 58–69.
- Hanley J, Debois MM, Mah D, Mageras GS, Raben A, et al. Deep inspiration breath-hold technique for lung tumors: the potential value of target immobilization and reduced lung density in dose escalation. Int J Radiat Oncol Biol Phys. 45(3):603-11, 1999.

- Heimann T, van Ginneken B, Styner MA, Arzhaeva Y, Aurich V, Bauer C, Beck A, Becker C, Beichel R, Bekes G, Bello F, Binnig G, Bischof H, Bornik A, et al. Comparison and evaluation of methods for liver segmentation from CT datasets. IEEE Trans Med Imaging. 28(8):1251-65, 2009.
- Heimann T, van Ginneken B, Styner MA, Arzhaeva Y, Aurich V, Bauer C, Beck A, Becker C, Beichel R, Bekes G, Bello F, Binnig G, Bischof H, Bornik A, Cashman PM, Chi Y, Cordova A, Dawant BM, Fidrich M, Furst JD, Furukawa D, Grenacher L, Hornegger J, Kainmüller D, Kitney RI, Kobatake H, Lamecker H, Lange T, Lee J, Lennon B, Li R, Li S, Meinzer HP, Nemeth G, Raicu DS, Rau AM, van Rikxoort EM, Rousson M, Rusko L, Saddi KA, Schmidt G, Seghers D, Shimizu A, Slagmolen P, Sorantin E, Soza G, Susomboon R, Waite JM, Wimmer A, Wolf I. Comparison and evaluation of methods for liver segmentation from CT datasets. IEEE Trans Med Imaging. 2009 Aug;28(8):1251-65.
- Hill DL, Batchelor PG, Holden M, Hawkes DJ. Medical image registration. Phys Med Biol. 46:R1-45, 2001.
- Horn BK, Schunck BG. Determining optical flow: a retrospective. Artificial Intelligence. 59(1-2): 81–87, 1993.
- Horn BKP, Schunck BG. Determining optical flow. Artificial Intelligence. 17(1-3):185–203, 1981.
- Ibanez L, Schroeder W, Ng L, Cates J. The ITK software guide: the insight segmentation and registration toolkit. Kitware Inc, 5, 2003.
- Janssens G, de Xivry JO, Fekkes S, Dekker A, Macq B, Lambin P, van Elmpt W. Evaluation of nonrigid registration models for interfraction dose accumulation in radiotherapy. Med Phys. 36(9):4268-76, 2009.
- Janssens G, Jacques L, Orban de Xivry J, Geets X, Macq Benoit. Diffeomorphic registration of images with variable contrast enhancement. International Journal of Biomedical Imaging. doi:10.1155/2011/891585, 2011.
- Journal of the ICRU, Vol 10 No 1 (2010), Report 83, Oxford University Press.
- Keall P J. et al. Time—The fourth dimension in radiotherapy ASTRO Panel Discussion. Int J Radiat Oncol Biol Phys. 57, S8–9, 2003.
- Keall PJ, Mageras GS, Balter JM, et al. The management of respiratory motion in radiation oncology report of AAPM Task Group 76. Med Phys 33:3874-900, 2006.
- Klein A, Andersson J, Ardekani BA, Ashburner J, Avants B, et al. Evaluation of 14 nonlinear deformation algorithms applied to humanbrainmri registration.Neuroimage. 46(3): 786–802, 2009.

- Kohlrausch J, Rohr K, and Siegfried Stiehl H. 2005. A New Class of Elastic Body Splines for Nonrigid Registration of Medical Images. Math. Imaging Vis.23, 3 (November 2005), 253-280.
- Lee C, Langen KM, Lu W, Haimerl J, Schnarr E, Ruchala KJ, Olivera GH, Meeks SL, Kupelian PA, Shellenberger TD, Mañon RR. Evaluation of geometric changes of parotid glands during head and neck cancer radiotherapy using daily MVCT and automatic deformable registration. Radiother Oncol. 89(1):81-8, 2008.
- Low DA, Nystrom M, Kalinin E, Parikh P, Dempsey JF, Bradley JD, Mutic S, et al. A method for the reconstruction of four-dimensional synchronized CT scans acquired during free breathing. Med Phys. 30(6):1254-63, 2003.
- Lu W, Chen ML, Olivera GH, Ruchala KJ, Mackie TR. Fast freeform deformable registration via calculus of variations. Phys Med Biol. 49:3067–87, 2004.
- Lucas B, Kanade T. An iterative image registration technique with an application to stereo vision. In Proc. Seventh International Joint Conference on Artificial Intelligence, Vancouver, Canada, 674–679, 1981.
- Mageras GS, Mechalakos J: Planning in the IGRT context: closing the loop. In Seminars in Radiation Oncology. Volume 17. Elsevier. 268-277, 2007.
- Mah D, Hanley J, Rosenzweig KE, Yorke E, Braban L, Ling CC, Leibel SA, Mageras G. Technical aspects of the deep inspiration breath-hold technique in the treatment of thoracic cancer. Int J Radiat Oncol Biol Phys. 48(4):1175-85; 2000.
- Maintz JB, Viergever MA. A survey of medical image registration. Med Image Anal. 2(1):1-36, 1998.
- Man KF, Tang KS, Kwong S. Genetic Algorithms Concepts and Designs. London: Springer; 2001.
- Mani, V.R.S, and Dr.S. rivazhagan. Survey of Medical Image Registration. Journal of Biomedical Engineering and Technology. 1(2): 8-25, 2013.
- Marroquin, J.L.; Botello, S.; Calderon, F.; Vemuri, B.C., "The MPM-MAP algorithm for image segmentation,"Pattern Recognition, 2000. Proceedings. 15th International Conference on, vol.1, no., pp.303,308 vol.1, 2000.
- McAuliffe MJ, Lalonde FM, McGarry D, Gandler W, Csaky K, Trus BL, Medical Image Processing, Analysis and Visualization in clinical research. Computer-Based Medical Systems, Proceedings. 14th IEEE Symposium. 381-386, 2001.
- Mejia-Rodriguez A, Arce-Santana ER, Scalco E, Tresoldi D, Mendez MO, et al. Elastic registration based on particle filter in radiotherapy images with brain deformations. Proceedings of the Annual International Conference of the IEEE Engineering in Medicine and Biology Society;2011:8049–8052.

- Modersitzki J. Numerical methods for image registration. New York: Oxford University Press; 2004.
- Murphy K, van Ginneken B, Reinhardt JM, Kabus S, Ding K, Deng X, Cao K, Du K, Christensen GE, Garcia V, Vercauteren T, et al. Evaluation of registration methods on thoracic CT: the EMPIRE10 challenge. IEEE Trans Med Imaging. 30(11):1901-20. 2011.
- Nijkamp J, Wolthaus JWH, Sonke JJ et al. Mid-ventilation determination with automatic four dimensional rigid grey-value registration on respiration-correlated computed tomography scans with moving lung tumours. Proceedings of the XVth ICCR - Toronto - Canada 2007.
- Nocedal J, Wright SJ. Numerical Optimization. New York: Springer; 2006.
- Orban de Xivry J, Janssens G, Bosmans G, De Craene M, Dekker A, Buijsen J, van Baardwijk A, De Ruysscher D, Macq B, Lambin P. Tumour delineation and cumulative dose computation in radiotherapy based on deformable registration of respiratory correlated CT images of lung cancer patients. Radiotherapy and Oncology. 85(2):232-238, 2007.
- Pan T, Lee TY, Rietzel E, Chen GT. 4D-CT imaging of a volume influenced by respiratory motion on multi-slice CT. Med Phys. 31(2):333-40, 2004.
- Peyrat JM, Delingette H, Sermesant M, Pennec X, Xu C, Ayache N. Registration of 4D time-series of cardiac images with multichannel Diffeomorphic Demons. Med Image Comput Comput Assist Interv. 11(Pt 2):972-9, 2008.
- Pluim JP, Fitzpatrick JM. Image registration. IEEE Transactions on Medical Imaging. 22(11): 1341–1343, 2003.
- Pluim JP, Maintz JB, Viergever MA. Image registration by maximization of combined mutual information and gradient information. IEEE Transactions on Medical Imaging. 19(8): 809–814, 2000.
- Reducindo I, Arce-Santana ER, Campos-Delgado DU, Vigueras-Gomez F. Non-rigid multimodal image registration based on local variability measures and optical flow. Proceedings of the Annual International Conference of the IEEE Engineering in Medicine and Biology Society; 2012: 1133–1136.
- Reducindo, I.; Arce-Santana, E.R.; Campos-Delgado, D.U.; Alba, A., "Evaluation of multimodal medical image registration based on Particle Filter", Electrical Engineering Computing Science and Automatic Control (CCE), 2010 7th International Conference on, vol., no., pp.406,411, 8-10 Sept. 2010
- Reducindo, I.; Arce-Santana, E.R.; Campos-Delgado, D.U.; Vigueras-Gomez, J.F.; Alba, A., "An exploration of multimodal similarity metrics for parametric image registration

based on particle filtering,"Electrical Engineering Computing Science and Automatic Control (CCE), 2011 8th International Conference on, vol., no., pp.1,6, 26-28 Oct. 2011.

- Ristic B., Arulampalm s., Gordon N. Beyond the Kalman filter: Particle filters for tracking applications. Artech House Publishers, 2004.
- Rosenzweig KE, Hanley J, Mah D, Mageras G, Hunt M, Toner S, Burman C, Ling CC, Mychalczak B, Fuks Z, Leibel SA. The deep inspiration breath-hold technique in the treatment of inoperable non-small-cell lung cancer. Int J Radiat Oncol Biol Phys. 48(1):81-7, 2000.
- Rosu M, Balter JM, Chetty IJ, Kessler ML, McShan DL, Balter P, Ten Haken RK. How extensive of a 4D dataset is needed to estimate cumulative dose distribution plan evaluation metrics in conformal lung therapy?. Med Phys. 34(1):233-45, 2007.
- Rosu M, Chetty IJ, Balter JM, Kessler ML, McShan DL, Ten Haken RK. Dose reconstruction in deforming lung anatomy: dose grid size effects and clinical implications. Med Phys. 32(8):2487-95, 2005.
- Rueckert D, Sonoda LI, Hayes C, Hill DL, Leach MO, Hawkes DJ. Nonrigid registration using free-form deformations: application to breast MR images. IEEE Trans Med Imaging. 18(8):712-21, 1999.
- Schaefer S, McPhail T, Warren J. Image Deformation Using Moving Least Squares. ACM Transactions on Graphics (TOG) - Proceedings of ACM SIGGRAPH 2006; 25(3): 533–540.
- Serifovic-Trbalic A, Demirovic D, Prljaca N, Szekely G, Cattin PC.Intensity-based elastic registration incorporating anisotropic landmark errors and rotational information. International Journal of Computer Assisted Radiology and Surgery 2009; 4(5): 463-468.
- Shimizu S, Shirato H, Kagei K, Nishioka T, Bo X, Dosaka-Akita H, Hashimoto S, Aoyama H, Tsuchiya K, Miyasaka K. Impact of respiratory movement on the computed tomographic images of small lung tumors in three-dimensional (3D) radiotherapy. Int J Radiat Oncol Biol Phys. 46(5):1127-33. 2000.
- Simon D. : Optimal State Estimation. Wiley Interscience, New York, 2006.
- Studholme C., Hill D.L.G., Hawkes D.J., An overlap invariant entropy measure of 3D medical image alignment, Pattern Recognition, Volume 32, Issue 1, January 1999, Pages 71-86,
- Tewatia D, Zhang T, Tome W, Paliwal B, Metha M Clinical implementation of target tracking by breathing synchronized delivery. Med Phys: 2006, 33(11);4330-6
- Thirion JP. Image matching as a diffusion process: an analogy with Maxwell’s demons. Med Image Anal. 2(3):243–60, 1998.

- Trees H. : Detection, Estimation and Modulation Theory: Part 1. John Wiley and Sons, John Wiley and Sons, 2001.
- Vandemeulebroucke, J., Sarrut, D. and Clarysse, P. The POPI-model, a point-validated pixel-based breathing thorax model. In XVth International Conference on the Use of Computers in Radiation Therapy (ICCR), Toronto, Canada. 2007.
- Vásquez Osorio EM, Hoogeman MS, Al-Mamgani A, Teguh DN, Levendag PC, Heijmen BJ. Local anatomic changes in parotid and submandibular glands during radiotherapy for oropharynx cancer and correlation with dose, studied in detail with nonrigid registration. Int J Radiat Oncol Biol Phys. 2008 Mar 1;70(3):875-82.
- Vásquez Osorio EM, Hoogeman MS, Bondar L, Levendag PC, Heijmen BJ. A novel flexible framework with automatic feature correspondence optimization for nonrigid registration in radiotherapy. Med Phys. 2009 Jul;36(7):2848-59.
- Vedam SS, Keall PJ, Kini VR, Mostafavi H, Shukla HP, Mohan R. Acquiring a four-dimensional computed tomography dataset using an external respiratory signal. Phys Med Biol. 48(1):45-62, 2003.
- Vemuri BC, Ye J, Chen Y, Leonard CM. Image registration via level-set motion: applications to atlas-based segmentation. Med Image Anal. 2003 Mar;7(1):1-20.
- Vercauteren T, Pennec X, Perchant A, Ayache N. Diffeomorphic demons: efficient non-parametric image registration. Neuroimage. 45(Suppl 1):S61–S72, 2009.
- Wang H, Dong L, O'Daniel J, Mohan R, Garden AS, Ang KK, Kuban DA, Bonnen M, Chang JY, Cheung R. Validation of an accelerated 'demons' algorithm for deformable image registration in radiation therapy. Phys Med Biol. 2005 Jun 21;50(12):2887-905.
- Wang H, Garden AS, Zhang L, Wei X, Ahamad A, Kuban DA, Komaki R, O'Daniel J, Zhang Y, Mohan R, Dong L. Performance evaluation of automatic anatomy segmentation algorithm on repeat or four-dimensional computed tomography images using deformable image registration method. Int J Radiat Oncol Biol Phys. 72(1):210-9, 2008.
- Wells WM, Viola P, Atsumi H, Nakajima S, Kikinis R. Multi–modal volume registration by maximization of mutual information. Medical Image Analysis. 1(1):35–51, 1996.
- Wolthaus JWH, Sonke JJ, Herk M van, Damen EMF. Image quality optimization, Reconstruction of a time-averaged mid-position CT scan for radiotherapy planning of lung cancer patients using deformable registration. Dissertation Medical Physics, 80-97, 2008.
- Wong JW, Sharpe MB, Jaffray DA, Kini VR, Robertson JM, Stromberg JS, Martinez AA. The use of active breathing control (ABC) to reduce margin for breathing motion. Int J Radiat Oncol Biol Phys. 44(4):911-9, 1999.
- Wrangsjo A, Pettersson J, Knutsson H. Non-rigid registration using morphons. Proceedings of the 14th Scandinavian Conference on Image Analysis (SCIA ’05), Springer, 2005.

- Xie Z, Ng L and Gee J 2003 Two algorithms for non-rigid image registration and their evaluation *SPIE-Medical Imaging: Image Processing* vol 5032 ed J M F Milan Sonka (San Diego, CA) pp 157–64.
- Xuan J, Wang Y, Freedman MT, Adali T, Shields P. Nonrigid medical image registration by finite-element deformablesheet-curve models. International Journal of Biomedical Imaging. 2006:1–9, 2006.
- Ying Liu; Benping Wang; Wang He; Jing Zhao; Zhi Ding, "Fundamental Principles and Applications of Particle Filters,"Intelligent Control and Automation, 2006. WCICA 2006. The Sixth World Congress on, vol.2, no., pp. 5327, 5331, 0-0 0.
- Zhang G, Dilling TJ, Stevens CW, Forster KM. Functional lung imaging in thoracic cancer radiotherapy. Cancer Control. 15(2):112–19, 2008.
- Zhiyong Gao, Bin Gu, Jiarui Lin, Monomodal image registration using mutual information based methods, Image and Vision Computing, Volume 26, Issue 2, 1 February 2008, Pages 164-173.
- Zitova B, Flusser J. Image registration methods: a survey. Image and Vision Computing 21, 2003.
- Zou KH, Warfield SK, Bharatha A, Tempany CM, Kaus MR, Haker SJ, Wells WM 3rd, Jolesz FA, Kikinis R. Statistical validation of image segmentation quality based on a spatial overlap index. Acad Radiol. 2004 Feb; 11(2):178-89.